Phase Separation in Active Systems: Non-Equilibrium Fingerprints

Giordano Fausti

université
PARIS-SACLAY

Thèse de doctorat

NNT: 2021UPASP141

Phase Separation in Active Systems: Non-Equilibrium Fingerprints

Séparation de phases dans les systèmes actifs : empreintes de non-équilibre

Thèse de doctorat de l'Université Paris-Saclay

École doctorale n° 564, Physique de l'Ile-de-France (PIF)
Spécialité de doctorat: Physique
Unité de recherche: Université Paris-Saclay, CEA, CNRS, SPEC, 91191, Gif-sur-Yvette, France.
Référent: : Faculté des sciences d'Orsay

Thèse présentée et soutenue à Gif-sur-Yvette, le 17 décembre 2021, par

Giordano FAUSTI

Composition du jury:

Olivier Dauchot Directeur de recherche, Université PSL	Président
Ignacio Pagonabarraga Professeur, Universitat de Barcelona	Rapporteur
Giuseppe Gonnella Professeur, Università degli Studi di Bari	Rapporteur
Cécile Cottin-Bizonne Directrice de recherche, Université Lyon 1	Examinatrice
Antonio Celani Research scientist , ICTP, Trieste	Examinateur
Hugues Chaté Chercheur CEA, Université Paris-Saclay	Directeur
Cesare Nardini Chercheur CEA, Université Paris-Saclay	Co-encadrant

acknowledgements

First, I would like to thank Giuseppe Gonnella and Igancio Pagonabarraga for their careful reading of the manuscript. I would also like to thank the other members of the jury, Antonio Celani, Cécile Cottin-Bizonne and Olivier Dauchot, for their interest in my work, as well as their questions and remarks.

I would also like to thank my two thesis advisors: Hugues Chaté and Cesare Nardini. The former for his scientific experience, careful critic of my work, and his adventurous spirit that made me discover the wonderful *path in the wood*, and a little more far away, China.

On the other hand, I would like to thank Cesare for his scientific intuition and close supervision, whose combination allowed me to obtain most of the results presented in this manuscript. I would also like to thank him for the patience and precious discussions about my future, that greatly helped me find my first postdoc.

I would also like to thank the other members of our group. In particular, a special thanks goes to Aurelio Patelli who greatly helped me in the initial stage of my Ph.D, by providing its supervision, especially in the development of the codes and algorithms I used in this manuscript. I also thank Xiaquing Shi, for the discussions and its very generous hospitality when I visited China. Finally, I thank Bruno Ventejou who shared with me the burden of doing a Ph.D. during the COVID-pandemic and Marc Besse, who recently joined the group.

I would then like to thank the researcher with whom I had the pleasure to collaborate and be a co-author: Mike Cates, for its precious insight and encyclopedic knowledge, as well as Alexandre Solon and Elsen Tjhung, for all the discussions and exchanges we had.

Then, I thank all the SPEC members. In particular: François Ladieu, for its advices on the good unrolling of my ph.D; Daniel Bonamy, head of SPYNX group,

for its mediation in tricky situations; Galette Basile and Dubrulle Bérengère, part of my *comités de suivi*, that annually supervised my work, scientifically but also psychologically. Finally, I would like to thank Nathalie Royer who guided me in the redundant and uselessly complicated labyrinth of french bureaucracy, and all the other people that I met, and with whom I shared something, be it just a little *bonjour* or a smile in the corridor. I would like to thank the IPhT laboratory, our neighbour, for the nice coffee room and Pierfrancesco Urbani, who helped me during the organization of my hybrid thesis defense.

I thank the LPTMC laboratory for its hospitality and computer cluster.

A huge thank goes to my girlfriend Rébecca, that never stopped supporting me, and helped me acquire a more critical view on my work conditions and our society. Thank you Rébecca, for believing in me, even in the darkest moments. Thank you for your creative mind, pour ton envie de voyager que, même en temps de Covid, nous as mené loin ; tu m'as vraiment aidé à redéfinir le monde autour et dedans moi.

A special thank goes also to my childhood friend Matteo, always ready to help me with his pragmatism that saved from oblivion one year worth of simulations. Thank you also for polenta, cotolette and for all the amazing Sundays spent eating and having an ironical gaze over our academic path. Because, *so, well, very good* and this is not important are still graved in our minds.

Then, of course, I would like to thank my first Parisian family. Thank you, Linda, for your questions and enthusiasm, and the hours spent discussing everything; Alice, for being always there for me in the moments of need, and for sharing my same existential doubts; Thank you Max for your precise, German mind and Lily, for your kindness and your inspiring romantic adventures.

It wouldn't be fair not mentioning my second Parisian family, also know as Corona Family, that allowed me to get thought the first confinement preserving my mental sanity (in however state it was). Thank to Rébecca, Emeline, Feryel, Hy-Kang, Charline, Ivet, Vlad, Alex, Max, Antoine, Fathima, Monica, Pascal, Eric and Hyppolyte. See you all in the legendary *Castel*, our second home.

Thanks to my flatmates for the board-games sessions and for breaking the loneliness of the n-th quarantine: thank you Hélène, Kenza, Robin, Agathe and Victor.

Infine vorrei ringraziare la mia famiglia e i miei amici oltralpe, che avrei voluto vedere molto di più e da cui il covid mi ha separato. Grazie dunque alla mia famiglia, sempre pronta ad accogliermi a Brozzo, fra le montagne. Grazie al Guido, per i molti *eau de chocon* subiti, a mia sorella Giulia per la precisione e pazienza spropositati, a mia mamma Eleonora, sempre pronta a sostenermi e aiutarmi, a mio papà, per la sua pragmaticità e per avermi spinto a continuare i miei studi. Grazie a tutti gli altri miei parenti, sempre pronti ad aiutare in caso di bisogno. Sopratutto ai miei nonni, Fausto e Rosa, che hanno attraversato l'Europa per assistere alla mia difesa; al nonno Massimo, ancora lucido nonostante l'età, e sempre interessato alle mie avventure, alla nonna Cesira, venuta a mancare nel mezzo della pandemia: *no,*

non ho ancora smesso di studiare e sì, non sono più solo. Grazie ai miei amici Torinesi, che nonostante non abbia potuto vedere molto spesso negli ultimi due anni, rivedo ogni volta come se non fosse passato un giorno dal nostro ultimo incontro. Grazie a Piero, per essere un orsacchiotto, a Luisa, per il suo entusiasmo e le sue imitazioni caprine, a Pierluigi, per la follia, e i gridi a squarcia gola, a Stella per sopportare quest'ultimo, ad Alessio ed Elvira e tutti gli altri membri del secondo piano del Collegio Einaudi (e annessi). Grazie anche ad Alessio, Laura, Campa, Giulia e Mascarino.

Grazie anche a Maria Luisa, per le nostre lunghe discussioni sulla sanità mentale.

Last but not the least, thanks to all the other people who believed in me, and helped me, even in apparently little details.

This project has received funding from the European Union's Horizon 2020 research and innovation program under grant agreement No 800945 — NUMERICS — H2020-MSCA-COFUND-2017

Contents

Overview

Active matter, being intrinsically out of equilibrium, displays surprising collective phenomena which are impossible in passive systems. In this Thesis we focus on phase separation, which is one of the main collective phenomena displayed by active systems. First understood via an approximate mapping to equilibrium liquid-vapor phase separation, it is nowadays clear that phase separated active systems show not only quantitative, but even qualitative difference with respect to the equilibrium phenomenology. This Thesis contributes in this direction.

Specifically, Chapter 1 introduces the main concepts and models that we use in the rest of the Thesis. There, we introduce active matter as an emerging field of non-equilibrium statistical mechanics, presenting some of its remarkable collective phenomena. Among all the different and fascinating displays of coordination pertaining to active matter systems, we focus our attention on a particular kind of phase separation, the *motility-induced phase-separation*, arising when particles decrease their self-propulsion in high density areas. Then, we discuss Active Model B+, a generic field theory based on symmetry arguments; the latter, introduced to describe phase separation in active systems, allowed to predict novel and unexpected types of phase separation: micro- and bubbly phase separation. We describe their main features, and study the mechanism by which they arise, linked to the fact that the classical Ostwald process can go into reverse because of activity.

In Chapter 2, we push forward our understanding of micro- and bubbly phase separation by performing large-scale simulations of Active Model B+, studying their statistical properties. Among our main results, we confirm that bubbly phase separation is a bona-fide phase separation among a micro-phase separated state, formed of vapor bubbles, and a homogeneous vapor phase. Moreover, we discover unexpected features, such as the fact that the equilibration time-scale to the bubbly phase-separated state is strongly dependent on system-size.

In Chapter 3, we discuss how the concept of interfacial tension should be understood in active systems. By exploiting – once again – Active Model B+, we show that no unique definition exists, and describe for the first time, both analytically and numerically, the capillary surface tension, the quantity describing the fluctuations of the liquid-vapor interface. We do so by deriving from first principles the capillary wave theory for active systems. Moreover, surprisingly, we discover that the capil-

lary interfacial tension can get negative because of activity, while still maintaining a phase separated state. We thus describe the novel phase of matter that arise in such a situation: a new type of micro-phase separation and an 'active foam state'.

We conclude in Chapter 4 by presenting preliminary results on a minimal model of diffusing bubbles interacting by reversed Ostwald ripening and coalescing upon contact. This allows us to elucidate the statistical properties of bubbly and micro-phase separation from a different perspective, and in particular to control the relative importance of reversed Ostwald ripening and coalescence. This might shed light on the properties of bubbly and micro- phase separation in particle-based models of active systems, where bubbles were found to have a very strong variability in size [1, 2].

In Appendix A, we provide technical details about the integration of Active Model B+ equations and the algorithms we used to analyze the data of our simulations.

The results of Chapter 3 where published in [3]. Those contained in Chapters 2 and 4 are not yet published in peer-review journals.

Chapter 1

Phase separation in active matter Systems

Active matter is a fascinating field of physics in which from simple, local interaction between its constituents, is possible to observe the spontaneous emergence of collective phenomena on length-scales much larger than the typical interaction length. Beside the fascination of discovering how a school of fish is capable of reacting collectively to a predator, or what is the physics behind the acrobatic motion of thousands of starling in the sky, the study of active matter might allow devising new soft materials with properties that are impossible in the traditional ones.

This introductory chapter is devoted to the presentation of some fundamental concepts in the study of active systems, while describing the main models that will be studied all along the Thesis. In particular, in Sec. 1.2, we define what active matter is, presenting a quick overview of experimental results, and placing it in the context of non-equilibrium statistical mechanics. Among the beautiful collective phenomena displayed by active systems, one of the most ubiquitous is phase separation, that we briefly overview in Sec. 1.3. Then, in Sec.1.4, we introduce field theories, a powerful tool used to study both equilibrium and non-equilibrium systems by means of few first-principle assumptions. After stating the main assumptions, we introduce and describe the phenomenology of Model B, the standard description of phase separation in passive systems in absence of momentum conservation. Finally, in Sec. 1.6, we discuss the particular case of field theories for active phase separation. In this latter section, we will introduce Active Model B+, one of the main models that we are going to study in the rest of the Thesis, and its phenomenology. This greatly differs from Model B because the Ostwald process can go into reverse due to activity. When this happens, two new form of phase separation emerge: either the coarsening is arrested to a finite lenght-scale (micro-phase separation), or a micro-phase separated state coexists with a macroscopic homogeneous phase (bubbly phase separation), sustaining a current in the steady state. The statistical

properties of micro- and bubbly phase separation will be studied in Chap. 2.

1.1 Statistical mechanics

1.1.1 At equilibrium

Statistical mechanics is a formal framework used to predict the macroscopic properties of bodies starting from the microscopic dynamics of its constituents. Of particular interest are the so-called *Thermodynamic systems*, macroscopic systems whose behavior can be defined by a handful of thermodynamic properties (*e.g.* mass, volume, internal energy, magnetization). If the latter are time and space independent, then the system is said to be in equilibrium.

Thermodynamic systems may be described at different level of coarse-graining, depending on the goal of the study. In most instances, for example, there is no point in describing the air in a room in terms of quarks and electrons, but it is more convenient to describe it in terms of atoms, molecules, or even – at the mesoscopic level - by the Boltzmann or hydrodynamic equations. Likewise, polymers can be described as a chain of interacting particles, while magnets can be described by toy models as the *Ising model*. In the latter, the system is described by (discrete) magnetic dipole moments generated by its magnetic atom. The common features of all these systems is that the enormous number of degrees of freedom (of the order of the Avogadro number $\sim 10^{23}$) allows for the emergence of statistical properties, whose study is the focus of statistical mechanics.

The state of a system composed by N particles is fully characterized by its $6N$ degrees of freedom, given by the momentum and position of each particle. We can think of its state as being in the highly dimensional space of positions and momenta, the *phase space*. In this contest, the evolution in time of the system describes a trajectory in the phase space and is determined by the mechanical equations governing its microscopic dynamic. To fully predict the evolution in time of the system, we would need to know all its $6N$ initial condition precisely, and to integrate the same number of (coupled) equations. This is, in practice, not possible, nor desirable. Rather than knowing the exact state of the system though all its microscopic details, we are interested in its macroscopic properties, shared by an enormous number of system configurations.

Statistical mechanics revolves around the concept of ensembles, consisting in many virtual copies of the same system in different configurations. In other words, ensembles are associated with the probability distribution of points in the phase space. The kind of ensemble chosen for a specific system depends on which physical constraints are applied to it. The easiest example is the *micro-canonical ensemble*, used to describe isolated systems, in which energy and number of particles are

conserved. In the latter, under the assumption of *equal a priori probability*, all the states are considered equiprobable. Most of the real equilibrium system, though, are actually able to exchange energy. In these cases the canonical ensemble is more appropriate, allowing for fluctuations of energy around its mean value. It can be shown that in the canonical ensemble the probability P that the system is found in a state of energy $E(\mathcal{C})$ is given by the *Boltzmann-Gibbs distribution*:

$$P(E) = \frac{e^{-\beta E(\mathcal{C})}}{Z} \tag{1.1}$$

where Z is the partition function of the system, and normalizes the probability distribution $P(E)$ to 1:

$$Z = \sum_{\mathcal{C}} e^{-\beta E(\mathcal{C})} \tag{1.2}$$

This, in turn, allow us to derive all system properties through its *ensemble average*. Solving exactly equilibrium systems, in most case, reduces to the computation of Z. It is fair to mention, though, that in practice, this can be very complicated. For this reason, other techniques have been developed. Among the others, we recall the renormalization group and Monte Carlo methods, often used for numerical simulations.

Another powerful tool used in this context are field theories (*e.g.* the Ginzburg-Landau theory of ferromagnetism). From this viewpoint, that will be reviewed below, the system is described at continuum level, in terms of its slow fields, conservation laws, symmetries and gradient expansion. The most well-known outcome is the development of Renormalization Group [4]. This provided one of those rare (unique?) examples of a technique capable of giving exact results even if applied to a minimal model, under the assumption that scale-invariance is present (as it happens close to a critical point). Possibly less well-known, is the fact that field theories in statistical mechanics often give accurate descriptions, sometimes even at quantitative level, of phenomena that are not scale-invariant [5]. Examples in this direction are coarsening laws in ordering kinetics [6], or the emergence of instabilities such as the spinodal decomposition in phase separating systems. Furthermore, an advantage of field-theoretical approaches is the little freedom that is left in their definition. In fact, there is much less freedom in defining a field theory than when setting up a microscopic model, unless microscopic properties of the physical system at hand (such as shape of the constituents, deformability and interactions) are very well known. All these properties are typically very hard to control in soft matter, and even harder to control in biological systems. For these reasons, field theories have been widely developed in statistical mechanics and soft matter.

1.1.2 Out of equilibrium

Most of real systems are out of equilibrium. Non-equilibrium systems arise in a wide range of different context and can have very different properties. However, it is possible to identify classes of system sharing similar phenomenologies and properties.

First, there are systems slowly relaxing towards equilibrium. The timescales involved may be much longer (like for glasses) or comparable to the observation times (like for long-range interacting systems such as galaxies). In either cases, there is a clear direction of relaxation.

A second class of non equilibrium problems is represented by those that cannot reach equilibrium due to boundary conditions creating a steady current. Typical examples are a piece of matter between two thermal reservoirs at different temperatures, or a fluid in which energy is continuously injected by, for example, heating.

We have a third class of non-equilibrium systems (subject of this work) known as *active matter*, in which detailed balance is broken locally: active units are able to transform some non-thermal (often chemical) energy present in the environment into self-propulsion, or other functional mechanism. It goes without saying that an isolated active system cannot last indefinitely, as the fuel has to be provided from the external on a long enough time-scale. Yet, the time-scales at play (the one on which new physics at the collective level arises and the one in which fuel is depleted) can be so separated that it is meaningful to keep this class of non-equilibrium systems distinct from the one above. In Sec. 1.2, we give a more specific definition and presents the main fields of research in active matter.

Out of equilibrium, we do not dispose of the central formalism encoded in the Boltzmann-Gibbs measure: we need to rely on other techniques, which are often rooted in the dynamics. Important techniques are based on the study of stochastic equations such as the Langevin equations, or of the time evolution of probability distributions given by master and Fokker-Plank equations. Importantly, the field-theoretical approach described above, and first developed for equilibrium systems, is fully generalizable to non-equilbrium contexts.

While new theoretical approaches were developing, the computational power of computers increased drastically in the last decade, allowing for extensive numerical studies. In particular, computer can be used in two different ways: by performing either simulations or calculations. The latter allows finding analytic solutions that would be complicated or tedious to compute manually, while the former allows one to directly observe the evolution of a system by means of its dynamical equations (up to a certain finite precision). Among the others, very successful approaches, routinely employed in non-equilibrium statistical mechanics, are molecular dynamics (in its deterministic and stochastic versions), and numerical integration of dynamical field theories.

1.2 Active matter systems

1.2.1 What are active systems?

Active matter is a young field of non-equilibrium statistical mechanics that studies system composed by a large collection of autonomous agents [7, 8, 9, 10]: non-thermal (most often chemical) energy is dissipated locally by its constituents that transform it into systematic motion (called hereby self-propulsion). Microscopic units of active systems will be called active agents or active 'particles'.

1.2.2 Active agents

In nature, we find a great variety of examples of active particles ranging across scales. From humans, forming crowds or vehicles fluxes [11], and other human-sized animals like sheep, fishes [12], birds [13] or herds of animals walking on dry land [14], to micrometer-sized active units such as bacteria, algae, or protein filaments, such as actin [15] or micro-tubules [16]. Beside living organism, in the last decade several synthetic active systems have been engineered by scientists in the lab: among others, Janus particles [17], micro-robots [18], vibrated asymmetric disks [19] and *Quincke rollers* [20].

1.2.3 Collective behaviors

In active systems, due to the interactions between its active units and their ability to self-propel, we can observe the emergence of many collective behaviors that have no equilibrium counterpart. Strikingly, many macroscopic properties are shared by very different systems. The natural question physicist tried to answer is whether – like in equilibrium – is possible to define minimal models capable of describing (qualitatively) various systems. This would allow to describe all the systems belonging to the same class, by mean of the same general theory. Even though we still lack a complete answer, we can distinguish several classes of active matter systems sharing similar microscopic properties and thus presenting the same macroscopic behavior. For example, we can define several classes of systems according to the presence or not of an ordered state, and if it is present, according to the nature of broken symmetries in the ordered state (polar or nematic). Another important criterion used to predict the behavior of active matter systems is the kind of momentum damping. In particular, we talk about *wet active matter* when momentum is conserved. This is often the case in suspension of bacteria where hydrodynamic interactions are relevant. On the contrary, for animals moving on lands or flock of birds, we usually neglect the medium in which active agents are moving, and momentum is not conserved. We then talk about *dry active matter*. In this Thesis, in particular, we will only focus on dry active matter. The reason behind it is that

the particular collective phenomena under our analysis, active phase separation, most often happens close to a substrate (this in turn imply that momentum is not conserved). It would be interesting to see the kind of new physics hydrodynamics brings [21], but this is left to future studies.

Flocking: polar order In presence of microscopic aligning interactions between active particles, we can observe fascinating flocking phenomena, in which all particles are aligned (and move) in the same direction (*i.e.* we have polar order). Flocking can be observed in various groups of social animals, like birds, fishes or animal herds walking on dry lands (gnu, sheep, etc...). Strikingly, most of these self-ordering phenomena, are observed in absence of a group leader, and come from self-organization mechanisms [14]. An archetypal example is given by starling flocks, for which data analysis of bird trajectories allowed to conclude that interactions depend on topological rather than metric distances: each bird interact, on average, with the 6 to 7 nearest neighbors, regardless of their distance [13]. Other studies showed that collective response of bird flocks is achieved through scale-free behavioral correlations [22, 23, 24]. When approaching the study birds flocks, typical topics of interest are the emergence of collective motion, the characterization of interactions between individuals and the response to predators attacks [25]. Similar studies have been carried out for school of fish: from the understanding of phase transition emerging in large schools of fish [12], to the inference of interaction rules between individuals from experimental data [26, 27]. We can observe similar flocking states for simpler form of life, like suspension of bacteria, for which – when bacterial densities are sufficiently large – we have the emergence of collective motion with long range correlations and large density fluctuations [28, 29].

Nematic order Another important class of active systems, is represented by active particle aligning nematically. This can happen in two ways. Either particles are parallel but have a random head-tail orientation, or they do not present a head-tail asymmetry, and are just aligned. A typical example is given by systems composed by microtubules and molecular motors, presenting local nematic order and topological defects [30]. For non-living systems, instead, we can have this kind of order in vibrated copper-wire segments [31]. When hydrodynamic interactions are relevant, instead, we can observe the so-called *active turbolence*. In [32], for example, was observed a self-sustained turbulent motion for dense suspensions of *Bacillus subtilis*.

Phase separation in absence of alignment Another important class of active matter comprehend systems for which steric repulsion is crucial (*e.g.* for self-propelled spherical particles [33]), or for which particles adapt their speed due to the density of other particles they sense. This happens in some bacterial suspensions, where bacteria slow-down due to *quorum sensing*, leading to the phase separation of the

suspension dense cluster diffusing in a more dilute phase [34]. This kind of phase separation, caused by a motility drop in presence of a particular denser area of bacteria, is known as motility-induced phase-separation and is the subject of Sec.1.3.1.

Other collective motions The above list of collective phenomena, and the relative classification, is far from exhaustive and it just meant to give the reader the flavor of the diffeent kind of systems and collective phenomena we can encounter in the study of active matter. We now provide some more examples that do not fit in the above classification.

Among other active system, we have the *cytoskeleton*[15], a versatile network of protein filaments, that is a fundamental component of most cells; in particular, it determines the cells shape, and is responsible for many fundamental cell events, such as cell division and migration. To better understand these phenomena, various experimental studies have reproduced active networks of molecular motors and proteins filaments *in vitro*. These experiments have allowed to simulate the self-organization of microtubules into both polar and nematic phases [35], and to understand the contractile properties of active cytoskeletal networks [36]. Other interesting studies showed how motile cells in dense bacterial suspensions can self-organize into collective oscillatory motion, despite the erratic movement of the singular bacterial cell [37] and how swarms of midgets, despite not showing global order, display strong correlations in the motion of individuals [38](that is strongly influenced by the presence of other midgets).

Synthetic active matter Finally, physicist have created synthetic active matter systems [39], either to device microrobots to perform complex tasks [40] or to improve experimental control over active systems. A typical example is provided by Janus particles [17], whose surfaces present different chemical or physical properties. In particular, by exploiting different chemical reactions on its sides (*e.g.* the two emispheres of a micro-sphere), is possible to generate a net motion of such objects. One striking example of controllable active environment is given by suspensions of colloids with programmable interactions, for example by exploiting Janus particles propelled though a light-induced mechanism [41, 42]. By focusing a laser beam on single particles, is possible to control their motion according to the configuration of other particles (tracked through digital optical microscopy).

Theoretical approaches There are several ways in which we can study active matter. Agents-based models represent a widely investigated approach which often seek qualitative (rather than quantitative) agreement with real active matter systems. The success of this approach relies on its simplicity, that allows, on one hand, to discriminate the fundamental ingredients leading to collective phenomena, and on the other, to simulate them easily.

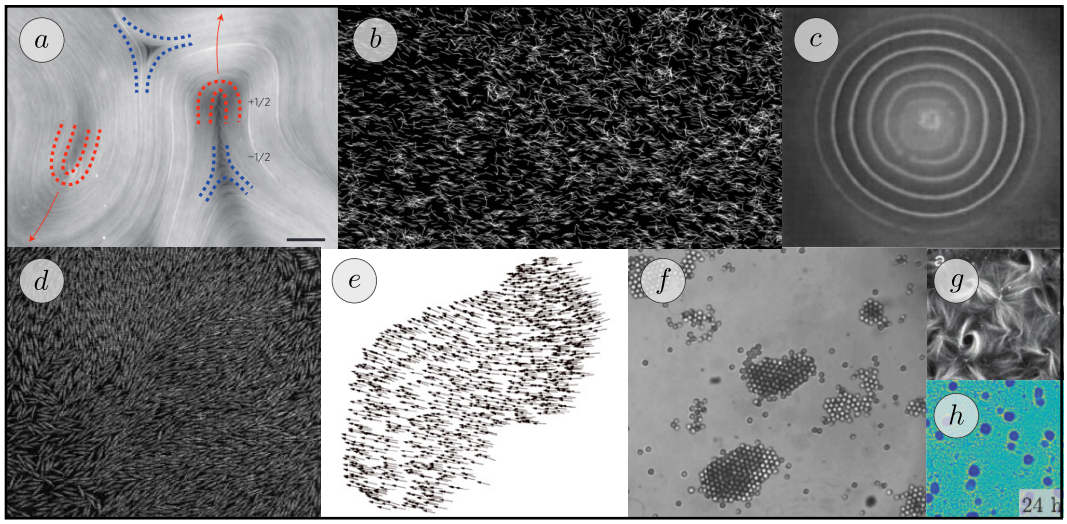

Figure 1.1: Experimental realization of active matter systems.
(a) Fluorescence microscope image of a dense quasi-2d film of microtubules and molecular motors that exhibits nematic order and topological defects. [30]
(b) Nematically-ordered phase of filamentous bacteria [28]
(c) experimental images of bacterial colony of *S.typhimurium* [43]
(d) Active nematic phase of vibrated copper-wire segments. From [31].
(e) Velocity field of starling in a flock of more than 10^3 birds from [23]
(f) Phase separation of a (quasi-)two-dimensional colloidal suspension of self-propelled spherical particles into clusters and a dilute phase. [33]
(g) Pattern of an active network of microtubule, organized *in vitro* by the action of molecular motors. [44]
(h) Microscopy images of *Myxococcus xanthus* cells undergoing phase separation via a nucleation and growth process from [34]

One of the first attempt in this direction was carried out by Vicsek [45], that introduced a model of identical self-propelled particles, aligning their velocity with the average neighbors one. Since the original model, various modification has been proposed [46], creating a class of models describing a well characterized disorder to order transition. Another example of minimal model is given by *active Brownian particles*, diffusing at a constant speed, while their direction of motion is subject to angular diffusion.

A different approach, investigated since when physicists got interested in active matter [7] is to study coarse-grained theories, such as continuum field theories, that study the large-scales, long-time behavior of the system. The advantage of this approach is that we can describe the system behavior by few fields. Moreover, little freedom is left in defining systems at the large-scale, allowing to study generic (*i.e.*, independent of system details) and universal physics; this is at variance with microscopic models, given that active matter systems are often too complex to be

modeled from first principles. While it is clear that Vicsek model is a crude description of flocking and not much control is available on whether anything changes upon changing the definition of the model, Toner-Tu theory (a continuum, general theory of flocking [22]) might be exact at large scales. As we will make large use of active field theories, we dedicate Sec.1.4 to introduce them in more details.

1.3 Active phase separation

1.3.1 MIPS

This Thesis studies phase separation in active systems. This is one of the most fundamental and well known phenomena in the field. Because detailed balance is broken, active systems can indeed show phase separation even in the absence of attractive interactions, a phenomenon known as *motility-induced phase separation* (MIPS)[47].

As the name suggest, MIPS is linked to the self-propulsion speed of particles and its dependence on the local particle density. In particular, it is caused by positive feedback between slowing down and accumulation. Self-propelled particles tend to accumulate where they move more slowly, while slowing down in high density area. Such dependence of the propulsion speed on the local density ρ, can arise in, at least, two different ways. Some bacteria can measure the density of surrounding bacteria by sensing the chemicals released by them, and adapt their speed accordingly. This is what is called *quorum-sensing* in microbiology. Otherwise, the slowdown at high density can be caused effectively by steric interactions: obviously a nearly hard-core particle cannot move much if tightly surrounded by others. In both cases, one refer to quorum sensing when the self-propulsion speed of particles is made dependent of the local density.

It was shown[48] that when the positive feedback is strong enough the homogeneous state becomes unstable. In particular, if

$$\frac{d\log(v)}{d\log(\rho)} < -1 \tag{1.3}$$

the system phase-separates in a dense phase of slow particles, and a dilute phase of fast movers.

MIPS was also observed experimentally in system composed by active colloidal particles [33, 34]. The latter can be living organism, such as bacteria or algae, but also synthetic micro-swimmers, like Janus particles. A general microscopic model for this kind of system is to consider an ensemble of self-propelled units, whose dynamics can be approximated by a density dependent propulsion speed $v(\rho)$ and a relaxation time τ associated to its direction of motion. Historically, MIPS was first

theoretically predicted in models of swimming bacteria with discrete re-orientations (though a 'run and tumbling' dynamics) interacting via quorum-sensing [47], and then on active Brownian particles interacting more directly, through pairwise forces at short distances [49]. It was then shown that when the motility is independent of motion direction, the two stochastic dynamics – run and tumble and active Brownian – are actually equivalent (at leading order) for large length- and time-scales [50].

MIPS can also be studied using continuum field theories. For example, when propulsion speed depends only on the local density ρ (and not on its derivatives), we can map, at large scales, pure quorum sensing models to the vapor-liquid phase separation of equilibrium systems [48]. In particular, an explicit coarse-graining of microscopic quorum sensing models shows that is possible to recover an effective free energy equal to [47]

$$f(\rho) = \rho(\log(\rho) - 1) + \int_0^\rho \log v(s) ds \,. \tag{1.4}$$

However, this mapping is complete only for particles whose self-propulsion velocity depends locally on the density; otherwise, it breaks down when trying to recover the liquid and vapor binodals. Nevertheless, these can be computed [51], for example introducing generalized chemical potentials and pressure [52]. On the contrary, for particles interacting through an isotropic, repulsive pair potential, is possible to define a mechanical pressure that is constant in the two phases, but not to define a chemical potential constant across the liquid and vapor phases [53].

All in all, phase separation as described by quorum-sensing model has not only the same qualitative but even quantitative properties as equilibrium liquid-like phase separation. It is however clear that more complex phenomenology can arise in active phase separation, as we will discuss in the next section.

1.3.2 Phase separation beyond quorum-sensing

Unlike what was initially though, the description of active phase separation using quorum-sensing particles is far from describing the full phenomenology of the phenomenon. This conclusion can be reached by following several hints, that both simulations and the experimental world give us.

First, experiments on self-propelled colloids often show micro-phase separation where clusters dimension arrest to a finite length and do not coarsen to system-size scale [54, 55, 33]. This is in contrast with what happens at equilibrium, where the so-called Ostwald ripening process makes big cluster grow and small one shrink, leading to a full phase separated state. Some examples of arrested coarsening are shown in Fig. 1.2. Several mechanisms can lead to such physics, as for example chemical [56, 57], hydrodynamic interactions [58, 21] or alignment [55].

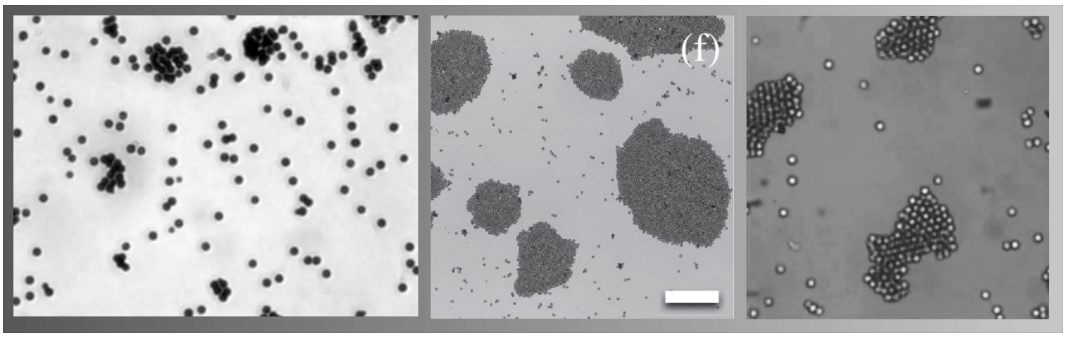

Figure 1.2: 'Cluster phase' in self-propelled colloidal systems. From left to right, pictures are taken from [54, 55, 33]

Second, simulations of dense suspensions of active Brownian particles interacting through pairwise repulsive forces in 2 dimensions [59, 7], show that the dense phase is more complex than a passive liquid (see Fig. 1.3). In particular, it is possible to observe bubbles inside the dense phase. Bubbles nucleate in the liquid clusters and then diffuse until reaching the vapor-liquid interface, where they are ejected. This creates a mass current, manifestly breaking time reversal symmetry at a mesoscopic scale. Such phenomena, hereby termed bubbly phase separation, is absent in quorum-sensing models [60].

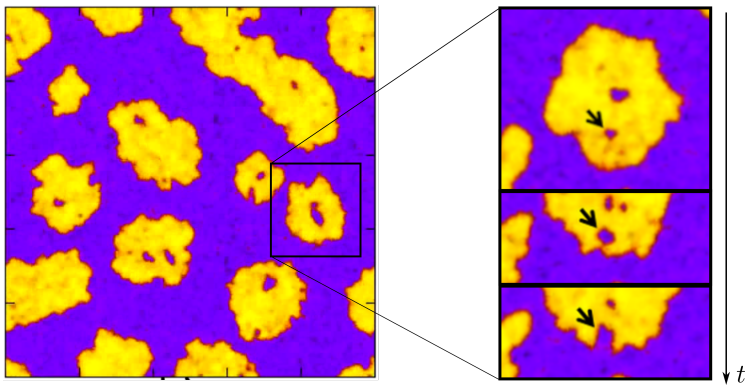

Figure 1.3: Snapshots of the local density field for simulation of active Brownian particles (adapted from [59]).
Left: snapshot of bubbles inside the dense phase. Right: three successive snapshots showing a bubble being ejected when reaching the interface of the dense phase.

Third, even more complex forms of phase separation have been observed in experiments with nematodes [61].

Fourth, simulations on models of self-propelled particles with nearly hard-core

interactions have recently shown that the internal structure of the dense phase can be even more complex, showing regions with high hexatic order that are separated by sharp defect lines [2]. More in general, the physics of active particle systems at very high densities, and the transitions between liquid, hexatic and solid phases is a delicate topic that has been investigated only since recently [62, 63].

All these hints pointed towards the need of a different, more complete theory that goes beyond quorum-sensing active particles and their coarse-grained description. Active Model B+ was recently introduced in [60] as a generic theory of phase separation in active systems under the sole assumption that density is the only slow field. Although, by itself, this cannot thus describe very dense systems that might show hexatic order, we will see in the next section that it gives surprisingly new predictions on active phase separation. After introducing active field theories in general, we will present such theory in Sec. 1.6.

1.4 Field theories for passive phase separation

A very powerful tool that can be used to study both passive and active systems are field theories: continuum theories purposely describing the system under study at mesoscopic level. Although microscopic details are lost, there are two significant advantages of a mesoscopic approach: on one side, these theories can be built from first principles; on the other, their simplicity often allows for analytical progress otherwise not possible in microscopic models. In this context, the link with microscopic parameters should be sought a-posteriori, measuring observable quantities – such as, for example, the surface tension (more on this below) – that are set by the parameters defining the field theory.

In passive systems, there is a well-defined path for building such field theories. First, one must identify the slow fields, *i.e.* those that do not relax exponentially fast in time; these are called order parameters $\Psi(\boldsymbol{r}, t)$. The order parameters needed to fully describe active matter systems, depend on the nature of the system itself. Among the most common examples we have:

- ρ, the density of a single-component, compressible fluid.
- $\boldsymbol{v}$, the fluid velocity
- ϕ, the relative composition of a binary mixture.
- $\boldsymbol{p}$, the polarization vector describing the orientation of polar particles.

The classical top-down approach [5, 64] provides a dynamical perspective that retains fluctuations; In this context, the field theory describing the dynamics of $\Psi(\boldsymbol{r}, t)$, is written on the basis of symmetries and gradient expansion (under the

assumption that the gradients of the field are small). In other words, one performs a Taylor expansion up to a given, fixed, order of $\Psi(\boldsymbol{r}, t)$. It must be noted, however, that such expansions should contain all terms that do not violate any symmetry of the problem.

Sometimes, field theoretical descriptions can be also obtained by direct coarse-grain of microscopic models. This, unlikely the top-down approach described above, allows to have a direct connection between the field theory coefficients and the underlying microscopic dynamic. Such path is particularly powerful when one is able to build microscopic models from first principles. As recalled before, however, the microscopic models of active systems are themselves phenomenological, rather based on first principle analysis. Therefore, it is unclear what can be gained by such linking process, and the link might reveal not really useful in practice.

A typical field theory for Ψ has the form

$$\dot{\Psi}(\boldsymbol{r}, t) = G[\Psi] + \xi \tag{1.5}$$

where G is a functional of Ψ and ξ is the noise term. Setting the latter to zero provide us the so-called 'hydrodynamic description' of the system: a mean-field version of the equations describing their average behavior. Even though this is sometimes a good first approximation, we have to retain the noise part to study the system fluctuations.

In equilibrium systems, in which particles do not dissipate energy locally, the steady-state probability of the order parameters $P[\Psi(\boldsymbol{r})]$ is unique and equal to the Boltzmann distribution:

$$P_B \propto \exp[-\beta F[\Psi]] \tag{1.6}$$

Where F is the Helmholtz free energy, and is equal to the system Hamiltonian H just if all the microscopic details are retained (*i.e.* no coarse-grain procedure is used). Setting the steady state probability to the Boltzmann distribution is enough to fix the noise term. In out of equilibrium systems, this does not hold. Therefore, the form of the noise term must be explicitly obtained from the microscopic equations or guessed. In the next sections we will review, following the terminology introduced in [64], the so-called *Model B*, the canonical stochastic field theory for diffusive phase separation of a conserved scalar field (without moment conservation).

1.4.1 Model B

One of the most successful field theories is Model B, which describes phase separation of an equilibrium system in the absence of momentum conservation. It can be used to describe attractive Brownian particles close to a substrate or liquid-liquid phase separation on short enough time-scales such that inertial effects of the fluid can be neglected [6].

Let us consider a colloidal solution, in which insoluble particle diffuse in a fluid medium, interacting among themselves. To study the colloidal particle motion we

disregard all the degrees of freedom of the liquid, passing from a deterministic description of the colloidal solution, to coupled Brownian motion equations. This is justified if the motion of the particles is taking place close to a boundary with which they can exchange momentum. In this situation, the only order parameter is ρ, the particle density. The hydrodynamic equations read (with the noise current $J_n = 0$ for now):

$$\dot{\rho} = -\boldsymbol{\nabla} \boldsymbol{J} \,, \tag{1.7}$$

$$\boldsymbol{J} = -M[\rho]\boldsymbol{\nabla}\mu + J_n \tag{1.8}$$

where M is the mobility and is equal to $M[\rho] = \beta\rho D[\rho]$, where $D[\rho]$ is the particle diffusivity and $\beta = \frac{1}{K_b T}$ the inverse temperature. For simplicity, we make this dependence local $D[\rho] = D(\rho)$. The particular form of (1.7) comes directly from the fact that ρ is a conserved field. Since this is an equilibrium system, the chemical potential $\mu(\boldsymbol{r})$ of (1.8) can be written as a functional derivative of a free energy $F[\rho]$:

$$\mu(\boldsymbol{r}) = \frac{\delta \mathcal{F}}{\delta \rho(\boldsymbol{r})} \tag{1.9}$$

where F depends on the interaction among particles. For a sufficiently soft, pairwise interaction potential $w(r)$, it can be approximated with the mean-field free energy

$$\beta\mathcal{F}[\rho] = \int \rho(\boldsymbol{r})(\ln \rho(\boldsymbol{r}) - 1)\, d\boldsymbol{r} + \beta \int \rho(\boldsymbol{r}_1)\rho(\boldsymbol{r}_2) w(|\boldsymbol{r}_1 - \boldsymbol{r}_2|)\, d\boldsymbol{r}_1\, d\boldsymbol{r}_2 \,. \tag{1.10}$$

What is left now to do, is to specify the noise term in Eq. (1.7). It can be shown that the fluctuation-dissipation theorem, or equivalently the request that 1.6 is the stationary measure, implies:

$$\boldsymbol{J}_n = \sqrt{2\rho D(\rho)}\boldsymbol{\Lambda} \,, \tag{1.11}$$

$$\langle \Lambda_i(\boldsymbol{r}, t)\Lambda_j(\boldsymbol{r}', t')\rangle = \delta_{ij}\delta(\boldsymbol{r} - \boldsymbol{r}')\delta(t - t') \tag{1.12}$$

where $\boldsymbol{\Lambda}$ is a Gaussian white noise. Note that, in this form, the noise is multiplicative since in (1.11), the Gaussian noise is multiplied by a function of the field ρ.

Finally, to get Model B we need two more steps:

- Taylor expansion of $\mathcal{F}[\rho]$ in weak gradients around the critical density ρ_0
- Taking a constant mobility M

The first step allows us to get rid of the non-local nature of the interaction term (the second one in equation (1.10)). Assuming the variations of ρ to be slow in the interaction range $w(r)$, we can approximate (1.10) with a square gradient theory:

$$\beta\mathcal{F}[\rho] = \int \left(f(\rho) + \frac{K}{2}(\nabla\rho)^2 \right) d\boldsymbol{r} \,. \tag{1.13}$$

If then we expand around a reference density ρ_0. We pass from ρ to $\phi = \rho - \rho_0$ and get the scalar ϕ^4 free energy:

$$\mathcal{F}[\phi] = \int \left(\frac{a}{2}\phi^2 + \frac{b}{4}\phi^4 + \frac{K}{2}(\boldsymbol{\nabla}\phi)^2 \right) d\boldsymbol{r}, \tag{1.14}$$

Where $a = a(T)$, while b and K are positive, and (for simplicity) independent of temperature. Notice that $f(\phi) = \frac{a}{2}\phi^2 + \frac{b}{4}\phi^4$ does not have a linear term in ϕ since it would anyway disappear when performing the functional derivative of $\mathcal{F}$. At the same time, also the cubic term was set to zero by choosing ρ_0 to be the critical density (this implies that the third derivative of f in such point is zero: $f'''(\rho) = 0$).

The second step allows us to get rid of the multiplicative noise. Indeed, if we neglect corrections of order ϕ in the mobility M we obtain:

$$M(\phi) = (\phi + \rho_0)\beta D(\phi + \rho_0) \simeq \beta\rho_0 D(\rho_0) = M \tag{1.15}$$

In principle this would be valid only in uniform phases or close to a critical point where ϕ is small everywhere. However, there are good reasons to think that this does not change the physics qualitatively, even in phase-separated systems. For example, this approach is able to capture not only qualitatively, but even quantitatively, the coarsening laws [6].

We finally get the equations for Model B:

$$\partial_t \phi = -\boldsymbol{\nabla} \cdot \boldsymbol{J}, \tag{1.16}$$

$$\boldsymbol{J} = -M\boldsymbol{\nabla}\mu + \sqrt{2Mk_BT}\boldsymbol{\Lambda} \tag{1.17}$$

$$\mu = \frac{\delta F}{\delta \phi} = a\phi + b\phi^3 - K\nabla^2\phi, \tag{1.18}$$

Although we 'obtained' it first from coarse-graining of a particle model, it should be noted that exactly the same result would be obtained, in a much simpler way, just invoking symmetry arguments and the fact that the density is the only slow field in the dynamics.

1.4.2 Phase diagram of Model B

We can derive interesting properties of the system at a mean-field level. Let's consider uniform states $\phi(\boldsymbol{r}) = \phi_0$. Those states have a free energy density that is equal to:

$$\frac{F}{V} = \frac{a}{2}\phi_0^2 + \frac{b}{4}\phi_0^4 = f(\phi_0). \tag{1.19}$$

Now, according to the sign of $a(T)$, we have two possible cases. When $a > 0$, $f(\phi_0)$ has a single minimum at $\phi_0 = 0$. This means that there is no way to lower the free energy by introducing a phase separation. The state with minimal energy is be the steady-state solution of Model B (with no noise). More interestingly, when $a < 0$,

$f(\phi_0)$ is a double well with minima at the two binodals $\pm\phi_b$ (see Fig.1.4(b)). This means that, for $-\phi_b < \phi_0 < \phi_b$, the free energy of a uniform state is larger than the one of a phase separated state. As is it energetically favorable, the system phase-separate in a dilute phase with density $-\phi_b$ (vapor phase), and a dense phase with density ϕ_b (liquid phase). In particular, for a system of volume V and total density ϕ_0, the volume of the two phases V_l and V_v can be found from the conservation of volume ($V_l + V_v = V$) and density ($(V_l - V_v)\phi_b = V\phi_0$). To be precise, when the system is phase separated the free energy has a non-null contribution from the term in K (the square gradient of ϕ). Anyway, this is a surface term scaling as V^{d-1} (since it gives no contribution far from the interface) and is always worth paying if the system is big enough($V^d >> V^{d-1}$ for $V \to \infty$). Moreover, notice that the system is linearly unstable in between the two spinodals $\bar{\phi} = \pm\phi_s = \pm(-a/3b)^{1/2}$ since there $f''(\phi_0) < 0$(see Fig. 1.4(b)).

When the noise D is not zero, we have a competition between energy and entropy. It turns out that, increasing the noise D, approaches the two binodals values until, for a critical noise value they meet at a tricritical point (see Fig.1.4(a)). Above this point entropy dominates, and phase separation is destroyed. Below, in between the binodals, the system phase separates. In particular, in between the spinodals, the uniform density is linearly unstable, and the system initially phase-separates through the so-called spinodal decomposition (in which bicontinous domains of liquid and vapor are formed). Outside the binodals, the phase separation happen though stochastic fluctuations of the majority phase, resulting in the nucleation of bubbles [or clusters] of the minority phase. In both cases, the final state is a bulk phase separated state.

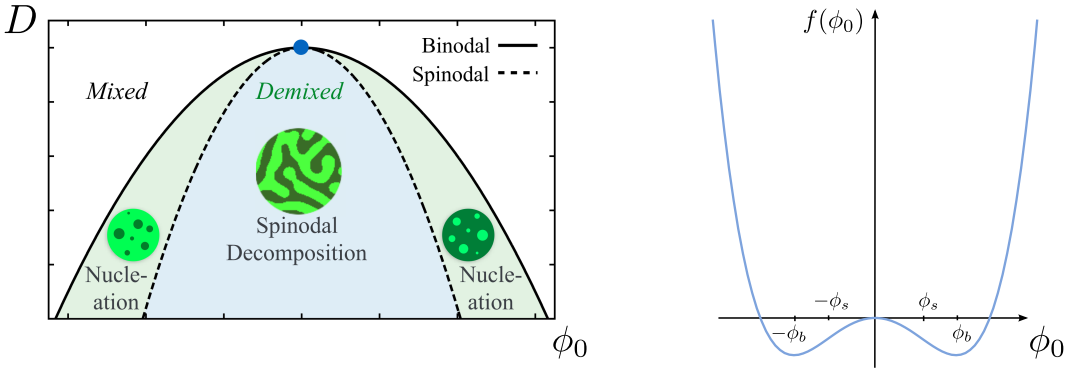

Figure 1.4: (a) Phase diagram in the $D \times \phi_0$ plane of Model B. (b) local free energy for a state of uniform density $\phi(x, y) = \phi_0$

1.4.3 Interface and interfacial tension

Phase separation, and the shape of the interface, arises from a trade-off between the cost of having a sharp interface (K term in (1.14)) and the price of having a density that is not in the two minima $\phi(x) \neq \pm\phi_b$ (the local free energy term $f(\phi)$ would prefer a sharp interface).

Since having an interface is associated with a cost in free energy (term K in equation (1.14)), the system will try to minimize the contact surfaces between the two phases. In most geometries this is achieved by means of a flat interface. In this particular case is easy to find the interfacial profile. Indeed, by using the Lagrange multiplier method, we can minimize $\mathcal{F}$, subject to the boundary conditions $\phi(\pm\infty) = \pm\phi_b$:

$$\frac{\delta}{\delta\phi}\left[\mathcal{F} - \beta\int \phi d\boldsymbol{r}\right] = 0 \tag{1.20}$$

The functional derivative of $\mathcal{F}$ is the chemical potential:

$$\mu(x) = \frac{\delta\mathcal{F}}{\delta\phi} = a\phi + b\phi^3 - K\nabla^2\phi \tag{1.21}$$

Equation (1.20) requires μ to be constant. In particular, using the boundary conditions we obtain:

$$\mu(\pm\phi_b) = \left(\frac{df(\phi)}{d\phi}\right)_{\phi=\phi_b} = 0 \tag{1.22}$$

Then one can show [5] that $\mu(x) = 0$ yields :

$$\phi(x) = \pm\tanh\left(\frac{x - x_0}{\xi_{eq}}\right) \tag{1.23}$$

where $\xi_{eq} = \sqrt{\frac{-K}{2a}}$ is the interfacial width and x_0 the midpoint of the interface.

A crucial quantity in phase separation is interfacial tension. We can define it as the excess of free energy per unit area of a flat interface [5]:

$$\sigma_{eq} = \int K(\partial_x\phi_0(x))^2 dx = \sqrt{\frac{-8Ka^3}{9b^2}}\,. \tag{1.24}$$

In equilibrium systems, the interfacial tension sets many physical properties. For example, it sets the Laplace pressure drop across a liquid-vapor interface according to its local curvature radius R. In particular, for a d-dimensional system we have:

$$\Delta P = \frac{(d-1)\sigma_{eq}}{R} \tag{1.25}$$

This pressure jump is responsible for the Ostwald ripening process, that determines the growth of big bubbles at the expense of smaller one. To better understand this

phenomenon, let's imagine a phase-separated system with two bubbles of radii $R_1 > R_2$ (both in equilibrium with the surrounding liquid). Due to the Ostwald ripening process, we have a flux of density from the biggest bubble (that therefore grows) to the smallest (that shrinks as a consequence). It is a well known fact that the dynamics of the biggest bubble radius R_1 (and similarly the smallest, by exchanging R_1 and R_2) follows:

$$\dot{R}_1 = \frac{\beta}{R\Delta\phi}\left[\frac{1}{R_2} - \frac{1}{R_1}\right] \tag{1.26}$$

where $\Delta\phi$ is equal to the difference in density between the two binodals, and β is the Ostwald ripening rate depending on the interfacial tension though:

$$\beta = \frac{(d-1)\sigma_{eq}}{\Delta\phi} \tag{1.27}$$

Notice that is the sign of σ_{eq} that favors the largest bubble.

The interfacial tension σ_{eq} is also linked to the so-called *capillary wave theory*. In other words, it is responsible for the spectra of the interfacial fluctuations. In particular, let $h(\boldsymbol{x})$ be the height of a vapor-liquid interface and $h(\boldsymbol{q})$ its Fourier transform. Then, the average energy density of modes with absolute value $q = |\boldsymbol{q}|$, equal to $S(\boldsymbol{q}) = \langle |h(q)|^2 \rangle$, is linked to σ_{eq} through:

$$\frac{q^2 S(q)}{D} = \frac{1}{\sigma_{eq}} \tag{1.28}$$

We will see in the next section and in Chapter 3 that for out of equilibrium systems, this is not true anymore, and we cannot rely on a single definition of interfacial tension.

1.5 Field theories for active phase separation

As we saw in Sec. 1.2, active systems violate microscopic time-reversal symmetry. For this reason, phenomena impossible in passive systems – like the motility-induced phase-separation (MIPS) – can arise. As such, there is no fundamental reason to expect that active phase separation is described by Model B in active systems. Yet, the route employed to build Model B, identifying the slow fields and writing any term that is allowed by symmetries in a gradient expansion, remains perfectly valid. For a phase separating system with a single slow field ϕ (density), this means that all terms included in Model B should also be included in the field theory of active phase separation.

It is then a fact that no novel non-linearity can be added to Model B, that is relevant close to criticality in the Renormalisation-group sense (4-d perturbative

expansion) [65]. Possibly due to this reason, for a long time, active phase separation was understood via an approximate mapping to equilibrium liquid-vapor phase separation [48]. Later on, it became clear how this mapping is actually only valid when considering the zeroth order expansion of spatial gradients.

The first attempt to go beyond an equilibrium theory was provided in [51], where the effect of adding the first non-integrable term to the chemical potential of Model B lead to *Active Model B*. This is obtained by replacing Eq. 1.18 with

$$\mu = \frac{\delta F}{\delta \phi} + \lambda(\nabla\phi)^2 = a\phi + b\phi^3 - K\nabla^2\phi + \lambda(\nabla)\phi)^2, \tag{1.29}$$

Crucially, the active term λ cannot be reabsorbed in the free energy of Eq. (1.32). Despite its non equilibrium structure, Active Model B presents the same phenomenology of equilibrium systems. In particular, it only introduces some changes in the coexisting vapor and liquid densities of Model B.

The story got surprising when it was realized that including all terms at the same order of the λ non-linearity (which is, at order $\nabla^4\phi^2$) can dramatically change the phenomenology of phase separation. This lead to Active Model B+ [60], which indeed contains all terms at order $\nabla^4\phi^2$ in a gradient expansion. We now review such model, on which a large part of this thesis is based.

Before that, we should note that Active Model B+ is just the simplest field theory describing active phase separation, on top of which other ingredients could be added if necessary. For example hydrodynamic [58, 66] or polar [67] fields can be added if the phenomenology requires, retracing the path that has been developed at equilibrium in the Hohenberg-Halperin construction [64]. This is still largely unexplored.

1.6 Active Model B+

In this section, we will present Active Model B + (from now on AMB+), following very closely the paper in which it was introduced [60]. All the figures are taken from their article and rearranged to fit in a single column layout.

AMB+ [60] was introduced to describe active matter models in which time reversal symmetry is broken locally: is then a continuum field theory describing active phase separation for a diffusive, conserved density field ϕ when momentum is not conserved. The merits of this theory are the capability of describing all the various kind of active phase separations – observed in both experiments and simulations (see Sec. 1.3.2) – in a complete framework built on the basis of first principles. Starting from the equations of Model B, if we keep an additive noise and M constant, we can obtain AMB+ adding all the terms breaking time reversal symmetry up to a order ($\mathcal{O}(\nabla^4\phi^2)$. The theory obtained in this way is therefore the most general field

theory describing the diffusive dynamics of a single scalar field (up to that order, with coefficients independent of ϕ):

$$\partial_t \phi = -\boldsymbol{\nabla} \cdot \left(\mathbf{J} + \sqrt{2DM} \boldsymbol{\Lambda} \right) , \tag{1.30}$$

$$\mathbf{J}/M = -\boldsymbol{\nabla} \left[\frac{\delta \mathcal{F}}{\delta \phi} + \lambda |\nabla \phi|^2 \right] + \zeta (\nabla^2 \phi) \boldsymbol{\nabla} \phi \, . \tag{1.31}$$

$$\mathcal{F}[\phi] = \int \left\{ \underbrace{\frac{a}{2}\phi^2 + \frac{b}{4}\phi^4}_{f(\phi)} + \frac{K(\phi)}{2} |\nabla \phi|^2 \right\} d\mathbf{r} \tag{1.32}$$

where $K(\phi) > 0$. As it is standard for Model B, for simplicity we set $M = 1$ and $K(\phi) = K = const.$ The dynamics reads

$$\partial_t \phi = \nabla^2 \left(a\phi + b\phi^3 - K\nabla^2 \phi \right) + \lambda \nabla^2 \left| \boldsymbol{\nabla} \phi \right|^2 - \zeta \boldsymbol{\nabla} \left(\nabla^2 \phi \boldsymbol{\nabla} \phi \right) + \sqrt{2DM} \boldsymbol{\nabla} \boldsymbol{\Lambda} \tag{1.33}$$

The differences between AMB+ equations and the one for Model B are the two active terms in λ and ζ, breaking time reversal symmetry. By setting $\zeta = 0$ we obtain equations of Active Model B. Crucially, ζ is fundamentally different from λ. While the λ term is added to the equilibrium chemical potential and merely introduces a non-equilibrium correction to it; the ζ term allows $\boldsymbol{\nabla} \wedge \mathbf{J} \neq 0$ so that, even in steady state, circulating real-space currents are possible. Notice that the rotational part of $\mathbf{J}$ is (by definition) divergence-free and yields no contribution in the dynamics of ϕ (1.30). Moreover, by Helmotz decomposition we can insert the rotational free part of the ζ term inside the divergence part of equation (1.30), redefining the non-equilibrium chemical potential. However, this new chemical potential $\mu[\phi]$ is not local anymore: we will see later how this completely changes the physics of phase separation.

As in Model B, we have chosen the local free energy to be symmetric ($f(\phi) = f(-\phi)$). We loose nothing in generality by doing this, as a cubic term can be reabsorbed shifting the density by a constant. It is now clear that we have the symmetry under the exchange $(\phi, \lambda, \zeta) \to -(\phi, \lambda, \zeta)$. Even though AMB+ is introduced on the basis of first principles, it was shown in [60] that a closely related field theory can be obtained by coarse-graining particles models.

1.6.1 Binodals

Let's start by studying the mean-field case, where the noise is equal to zero ($D = 0$). We will see in this section, how it's possible to derive analytically the binodals. This will allow us to build, in the next section, the mean-field phase diagram of AMB+.

The binodals for the vapor and liquid phase (ϕ_1 and ϕ_2, respectively) are defined as the coexisting densities of two phases at steady state (vapor and liquid, or dense and dilute) separated by a flat interface. Having a flat interface, in absence of noise,

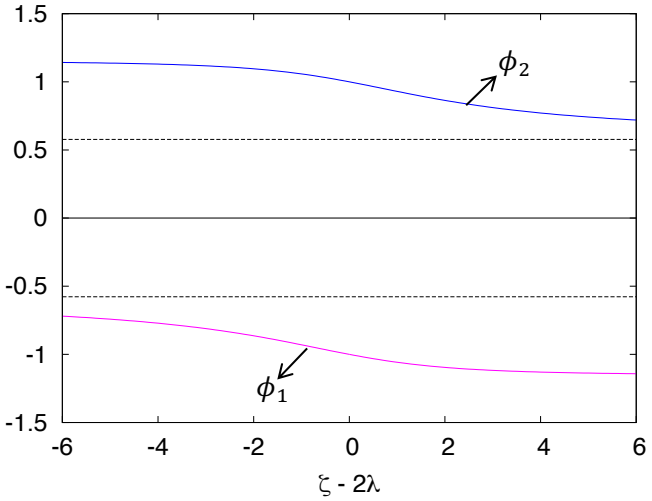

Figure 1.5: The binodals ϕ_1 and ϕ_2 (coexisting densities for a flat interface) for $K = 1$ and any value of A in the mean-field limit ($D = 0$). The binodals only depend on one combination of the two activity parameters ($\zeta - 2\lambda$) and not on these separately. Dashed lines indicate spinodal density defined by $f''(\phi_s) = 0$.

the density profile depends only on the normal coordinate x and the problem is effectively one-dimensional. Then, the current in 1.31 reads:

$$J = -\partial_x \mu \tag{1.34}$$

$$\mu = f'(\phi) - K\phi'' + \left(\lambda - \frac{\zeta}{2}\right)\phi'^2 \tag{1.35}$$

where $\phi' = \partial_x \phi$, and we could regroup the ζ and λ terms since in $d = 1$ we have $\nabla(\nabla\phi)^2 = 2(\nabla^2\phi)\nabla\phi$. Hence, the properties of the system depends just on $\zeta - 2\lambda$, instead of the ζ and λ separately.

Now, to find $\phi_{1,2}$ we need to find the stationary solution $\phi(x)$ with boundary conditions $\phi(\pm\infty) = \phi_{1,2}$ and a (smooth) interface around $x = 0$. At equilibrium this can be done by imposing the equality of the chemical potential and thermodynamic pressure across the interface. Turns out that the same can be done here by introducing some pseudo-variables that lead to the definition of a pseudo-pressure and (formally) to the same equations of equilibrium. All these pseudo-quantities has no direct physical meaning and can be seen as mathematical tools that allow us to convert the new mathematics of AMB+ to the more familiar passive one. In particular, the pseudo-density $\psi(\phi)$ and pseudo-potential $g(\phi)$ satisfy:

$$\frac{\partial^2 \psi}{\partial \phi^2} = \frac{\zeta - 2\lambda}{K}\frac{\partial \psi}{\partial \phi} \quad \text{and} \quad \frac{\partial g}{\partial \psi} = \frac{\partial f}{\partial \phi} \tag{1.36}$$

Of course, in the passive case, we recover the density field and local free energy:

$$\psi \xrightarrow[\lambda,\zeta\to 0]{} \phi \tag{1.37}$$

$$g(\phi) \xrightarrow[\lambda,\zeta\to 0]{} f(\phi) \tag{1.38}$$

Then, similarly to the equilibrium case, we can impose the following two conditions and compute the binodals:

- chemical potential balance: setting $J = 0$ implies $\mu = \bar{\mu}$, a constant value obtained from the boundary conditions:

$$\bar{\mu} = f'(\phi_1) = f'(\phi_2)\,. \tag{1.39}$$

- pseudo-pressure balance: multiplying (1.39) by $\partial_x \psi$ and integrating across the interface gives

$$P(\phi_1) = P(\phi_2) \tag{1.40}$$

  where the bulk pseudo-pressure $P(\phi)$ is defined in terms of $\psi(\phi)$ and $g(\phi)$ as

$$P(\phi) = \psi(\phi)\bar{\mu} - g(\phi)\,. \tag{1.41}$$

Explicit results are easily obtained numerically because the solutions to (1.36) can be found explicitly (see Fig. 1.5). Notice that only in the passive limit ($\zeta = \lambda = 0$) the binodals are equal to the minima of the free energy density $f(\phi)$.

1.6.2 Correction to binodals for a finite-radius droplet

The same approach used for a flat interface can be generalized to curved ones, considering a dense droplet in a dilute environment (see Fig. 1.6(a), the inset on the right). The case of a vapor bubble in a liquid environment can be obtained exploiting the duality relation $(\phi, \lambda, \zeta) \to -(\phi, \lambda, \zeta)$.

Let us consider a stationary state given by a spherically symmetric droplet of radius R with density far form the interface equal to $\phi_+(R)$ (inside) and $\phi_-(R)$ (outside). We look for the values of $\phi_\pm(R)$ such that the configuration is stationary for the mean-field dynamics. Exploiting the spherical symmetry we can once again reduce our equations to one dimension, rewriting them with respect to the radial coordinate from the center of the droplet $r = |\mathbf{r}|$. Our aim is to compute the stationary densities far from the interface: $\phi(r = 0) = \phi_+$ and $\phi(r = +\infty) = \phi_-$, with $\phi_+ > \phi_-$.

The chemical potential can be rewritten including the irrotational part of the ζ term:

$$\mu[\phi] = \frac{\delta \mathcal{F}}{\delta \phi} + \lambda |\nabla \phi|^2 + \mu_\zeta \tag{1.42}$$

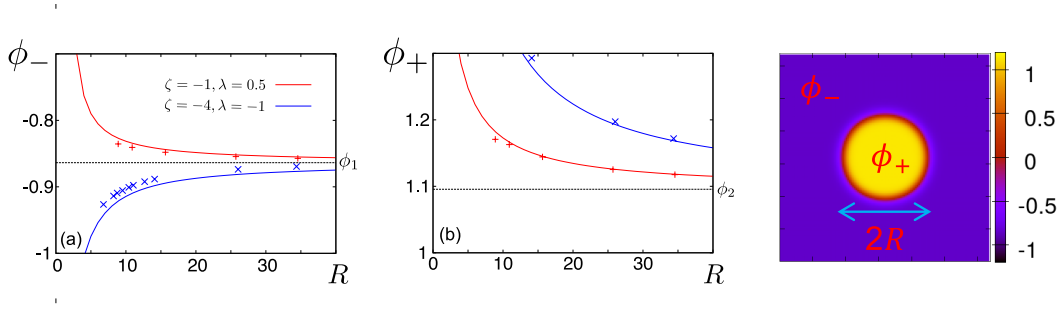

Figure 1.6: Stationary values of the density for a spherical dense droplet in a dilute environment in the mean-field approximation ($D = 0$). We plot in (a) the inner density $\phi_+(R)$ and in (b) the outer density $\phi_-(R)$ as a function of droplet radius R for two different sets of activity parameters: $\zeta = -1$ and $\lambda = 0.5$ (red, corresponding to region A of Fig. 1.7a) and $\zeta = -4$ and $\lambda = -1$ (blue, corresponding to region B of Fig. 1.7a). Points indicate numerical simulations results and lines indicate analytical ones. When the pseudo surface tension σ is positive (red line), $\phi_\pm(R)$ are both decreasing functions of R. Instead, when $\sigma < 0$ (blue line), $\phi_-(R)$ is increasing when R increases.

where μ_ζ is obtained by applying the Helmoltz decomposition to the current produced by the term in ζ:

$$\mathbf{J}_\zeta = \zeta(\nabla^2\phi)\nabla\phi = -\nabla\mu_\zeta + \nabla \wedge \mathbf{A} \tag{1.43}$$

$$\mu_\zeta(\mathbf{r}) = -\int d\mathbf{r}'\,(\nabla\cdot\mathbf{J}_\zeta)(\mathbf{r}')\,\nabla^{-2}(|\mathbf{r}-\mathbf{r}'|) \tag{1.44}$$

with $\nabla^{-2}(|\mathbf{r}-\mathbf{r}'|)$ being the Green function of the Laplacian. Since only the gradient part of $\mathbf{J}_\zeta$ affects the dynamics of ϕ, we can forget about $\mathbf{A}$ in the following. Crucially however, this construction comes at the price of non-local chemical potential $\mu_\zeta[\phi]$.

The full nonequilibrium chemical potential μ can be written using spherical coordinates as:

$$\begin{aligned}\mu &= f'(\phi) - K\phi'' - \frac{(d-1)K}{r}\phi' + \left(\lambda - \frac{\zeta}{2}\right)\phi'^2 \\ &+ (d-1)\zeta\int_r^\infty \frac{\phi'^2(y)}{y}\,dy\,.\end{aligned} \tag{1.45}$$

Here $\phi' = \partial_r\phi$. At steady state $\mu = \mu_I(R)$, a constant value. As we did for the flat interface, we proceed to find the two conditions used to compute the steady-state density levels far from the interface:

- Chemical potential balance: Using the boundary conditions $\phi(0) = \phi_+$ and $\phi(+\infty) = \phi_-$, we have

$$\mu_I(R) = f'(\phi_-) = f'(\phi_+) + \Delta \tag{1.46}$$

where

$$\Delta = (d-1)\zeta \int_0^\infty \frac{\phi'^2(y)}{y}\, dy \tag{1.47}$$

$$= \frac{(d-1)\zeta}{R} \int_0^\infty \phi'^2(y)\, dy + \mathcal{O}\left(\frac{1}{R^2}\right). \tag{1.48}$$

To go from (1.47) to (1.48) we have assumed a sharp interface limit ($R \gg \xi_{eq}$) so that we can approximate $1/r$ as $1/R$. Equation (1.46) states that the full chemical potential μ inside the droplet is equal to that outside so that no current flows across the interface at steady state. However, the equilibrium part of the bulk chemical potential $\mu_{eq}(\phi) = f'(\phi)$ has a jump Δ across the interface.

- Pressure balance: by multiplying (1.46) by $\partial_r \psi$, integrating across the interface, and again assuming that R is much larger than the interfacial width, we get:

$$P(\phi_+) = P(\phi_-) + \frac{(d-1)\sigma}{R} + \mathcal{O}\left(\frac{1}{R^2}\right) \tag{1.49}$$

where σ is a pseudo-tension defined by

$$\sigma = \frac{K}{\zeta - 2\lambda}\Big[\zeta \mathcal{S}_0 - 2\lambda \mathcal{S}_1\Big] \tag{1.50}$$

and depends on the value of two constants that are functional of the full shape of the interface:

$$\mathcal{S}_0 = e^{\frac{\zeta-2\lambda}{K}\phi_2} \int_0^\infty \phi'^2(y)\, dy \tag{1.51}$$

$$\mathcal{S}_1 = \int_0^\infty \phi'^2(y) e^{\frac{\zeta-2\lambda}{K}\phi(y)}\, dy\,. \tag{1.52}$$

The pseudo-pressure balance is formally the same as in equilibrium, where the Laplace pressure jump is equal to:

$$\Delta P_{eq} = \frac{(d-1)\sigma_{eq}}{R} \tag{1.53}$$

$$\sigma_{eq} = K \int_0^\infty \phi'^2(y) dy \tag{1.54}$$

here σ_{eq} is the equilibrium interfacial tension. Of course, at equilibrium ($\zeta = \lambda = 0$) we have $\sigma \to \sigma_{eq}$.

The coexisting densities for a spherical droplet of radius R in a dilute environment $\phi_\pm$ can now be derived from equations (1.46) and (1.49). In order to do so, we need to know the precise shape of the interface. The latter can be computed perturbatively in $1/R$ (see [60] for more details). These results are shown in Fig. 1.6 (lines) along with results from mean-field numerical simulation of AMB+. There is good agreement between the two, given the relatively modest values of R simulated.

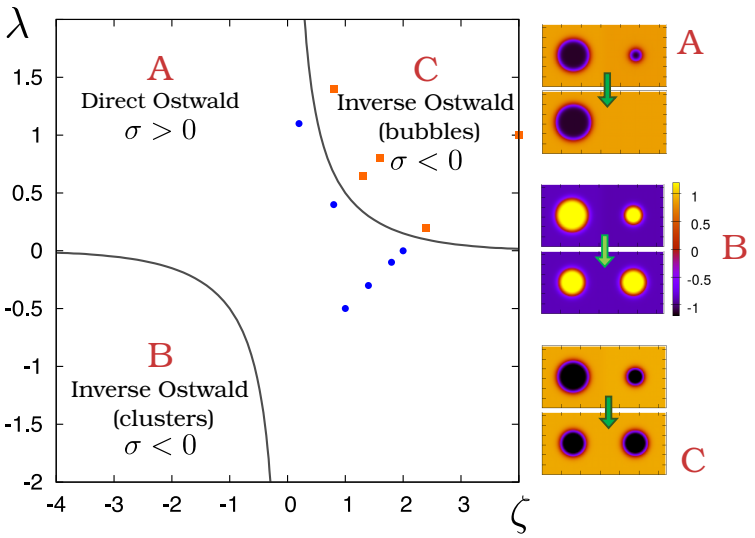

Figure 1.7: Mean field phase diagram of AMB+ with $K = 1$ and any value of $A > 0$, in $d = 2, 3$. Ostwald ripening is reversed where $\sigma < 0$. In region A, $\sigma > 0$, and we have normal/forward Ostwald ripening for both bubbles and droplets. In region B (*resp.* C) Ostwald ripening is reversed for dense droplets dispersed in a dilute environment (*resp.* dilute bubbles in a dense environment). Points are results from simulations of two droplets (red/square for reverse and blue/circle for forward Ostwald ripening).

1.6.3 Mean-field phase diagram

Formally we have a lot of mathematics that can be written in the equilibrium form. However, there is one crucial difference: at equilibrium the interfacial tension σ_{eq} is always positive, while this is not always true in AMB+, where σ can become negative. Studying the sign of equation (1.50) this happens when:

$$|\zeta - 2\lambda| < -\zeta \left| 1 - \frac{\mathcal{S}_0}{\mathcal{S}_1} \right| . \tag{1.55}$$

Once again, the analogous condition for a vapor bubble surrounded by the dense liquid follows from the duality transformation $(\phi, \lambda, \zeta) \to -(\phi, \lambda, \zeta)$. This conditions divide the $\lambda \times \zeta$ phase diagram at $D = 0$ in three regions (see Fig. 1.7(a). In region A, $\sigma > 0$ regardless of the sign of the interfacial curvature. In region B, $\sigma < 0$ for liquid droplets in a vapor environment but $\sigma > 0$ for vapor bubbles in a liquid environment. In region C, conversely, σ is negative for vapor bubbles and positive for liquid droplets.

Even though the way in which σ determines the pseudo-pressure jump at a curved interface, is the same in which σ_{eq} influences equilibrium systems, it does not have a direct connection to the physical mechanical tension as defined for active

systems *e.g.* in [68]. For example, the presence of a negative pseudo-tension does not cause interfaces to become unstable: the coexisting densities $\phi_\pm(R)$ remain well defined. The only effect of negative σ on them is to modulate their behavior with R. In particular, at equilibrium, both $\phi_\pm$ are decreasing functions of R, while this is the case for AMB+ only if $\sigma > 0$! In Fig. 1.6 we show these two distinct behaviours for a particular choice of λ and ζ within region A and B (as defined in Fig. 1.6).

1.6.4 Reverse Ostwald ripening

In this section, we show how negative pseudo-tension affects the Ostwald process, allowing for new features never seen in passive systems. We focus here on region B of Fig. 1.7(a); the behavior in region C then follows by the usual duality relation.

In region A, as in equilibrium systems, $\sigma > 0$ and consequently $\partial_R \phi_-(R)$ is negative. This causes the so-called direct Ostwald ripening process in which the density outside a small droplet is higher than the one outside a big one. This causes a current flows toward bigger bubbles and therefore to macro phase-separated state. On the contrary, in region B the sign of $\partial_R \phi_-(R)$ is positive, causing the Ostwald ripening process to be reversed: the current flows now from big to smaller bubbles. This allows active matter systems to be micro phase-separated as the reverse Ostwald ripening tend to uniform the size of liquid cluster in the system.

This reasoning can be converted into equations by considering a droplet of liquid of size $R(t)$ surrounded by a sea of distant droplets such as the mean density of the vapor phase at $r = \infty$ is $\phi_s = \phi_1 + \epsilon(t)$, where ϵ is the supersaturation. It can be shown [60] that the time evolution of the droplet radius $R(t)$ is equal to:

$$\dot{R} = \frac{\beta}{R\Delta\phi}\left[\frac{1}{R_s} - \frac{1}{R}\right] + \mathcal{O}\left(\frac{1}{R^3}\right) \tag{1.56}$$

where R_s is a fixed-point radius, β is a rate parameter, and $\Delta\phi = \phi_2 - \phi_1$. The explicit expressions for R_s is:

$$R_s = \frac{\Delta\psi\,\beta}{f'(\phi_s)\Delta\psi - \Delta g} \tag{1.57}$$

and likewise for β:

$$\beta = \frac{(d-1)\sigma}{\Delta\psi}\,. \tag{1.58}$$

where $\Delta\psi = \psi(\phi_2) - \psi(\phi_1)$, and σ is the pseudo-tension defined in (1.50).

In equilibrium models and in region A of the mean-field phase diagram of AMB+ (Fig. 1.7), the surface tension σ is always positive and thus β and R_s are also positive. R_s is then an unstable fixed-point radius: droplets smaller than R_s shrink and droplets larger than R_s grow.

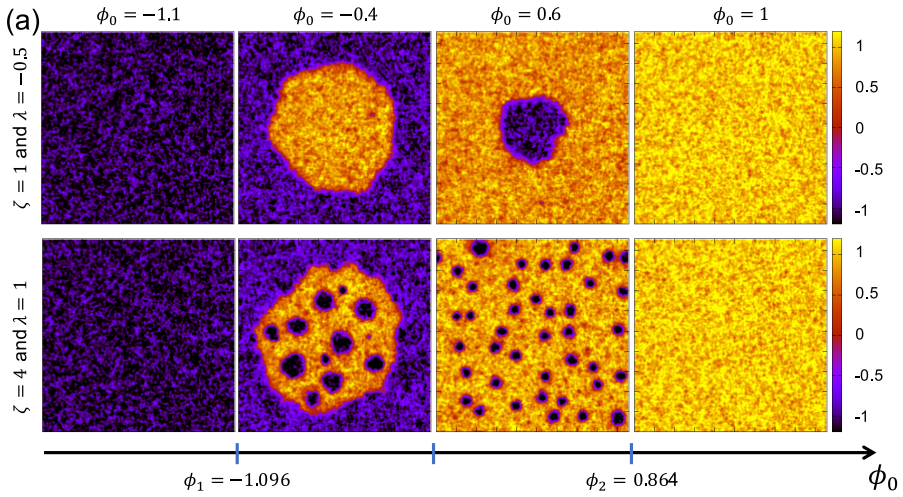

Figure 1.8: Steady state phase diagram as a function of global density $\phi_0 = \frac{1}{V}\int d\mathbf{r}\phi$ for two different sets of activity parameters: $\zeta = 1, \lambda = -0.5$ (region A in Fig. 1.7(a)), and $\zeta = 4, \lambda = 1$ (region C). These two points have the same mean-field binodals, since $\zeta - 2\lambda = 2$ in both cases. In A, the steady state phase diagram resembles equilibrium Model B with full phase separation into dense (yellow) and dilute (blue) phases. In C, besides the low and high density uniform phases, we observe either bubbly phase separation or a bubbly liquid. Since AMB+ is symmetric under $(\phi, \lambda, \zeta) \to -(\phi, \lambda, \zeta)$, the phase diagram in region B is obtained by exchanging dense with dilute regions.

In AMB+ the pseudo-tension σ is negative in region B and C of the phase diagram (Fig. 1.7) and so the rate β is also negative. It can be shown that for small ϵ in regime B ($\sigma < 0$), $R_s > 0$ and $\beta < 0$. R_s is now a stable fixed point radius: droplets of smaller than R_s grow and those larger than R_s shrink. This is the regime of reverse Ostwald ripening for liquid droplets dispersed in a continuous vapor phase.

Regime C in the mean field phase diagram (Fig. 1.7(a)) follows directly from the duality relation of AMB+. Note that there is no choice of parameters for which *both* droplets and bubbles are subject to the reverse Ostwald mechanism. As a consequence, microphase separation occurs in AMB+ on one side of the phase diagram or the other, but not both.

1.6.5 Finite noise phase-diagram

Thanks to the reverse Ostwald ripening process, we can have microphase-separated stationary states, at least when the noise is present (the steady state is independent on the initial condition chosen). Indeed in presence of noise, when droplets/bubbles are nucleated, their size tends to converge to the average one of the others. We show

in Fig. 1.8 the phase diagram, displaying the steady-state density field $\phi(x, y)$ as a function of (average) global density $\phi_0 = \frac{1}{V} \int d\mathbf{r}\, \phi(\mathbf{r}, t)$.

Outside the binodals, $\phi_0 < \phi_1$ or $\phi_0 > \phi_2$, the uniform phase is always stable. In region A (top row), the phase diagram resembles that of passive Model B, with bulk phase separation into dense liquid and dilute vapor phases. The only difference is given by the binodals value $\phi_{1,2}$ that are shifted.

The phenomenology in region C (bottom row) is much more interesting. Besides the low-density and high-density uniform phases when ϕ_0 is outside the binodals, for $\frac{\phi_1+\phi_2}{2} \lesssim \phi_0 \lesssim \phi_2$ in region C we observe initial coarsening of dilute bubbles. At long times, however, the coarsening arrests and the number of bubbles fluctuates around some average. This represents nonequilibrium microphase separation in the form of a bubbly liquid. Again, in region B, the duality transformation allows us to say that the steady state for the inverse parameters -λ, ζ is instead a cluster phase. At global densities ϕ_0 in the range $\phi_1 \lesssim \phi_0 \lesssim \frac{\phi_1+\phi_2}{2}$ within region C, the system creates a globally inhomogeneous steady state resembling conventional bulk phase separation, except that within the dense phase, vapor bubbles are continuously formed and then expelled to the exterior bulk vapor (the same happens in simulations of active Brownian particles interacting through a pairwise, repulsion potential, as we saw in Fig.1.3). The bubbly phase separation is best understood as a bulk coexistence between a bubbly liquid and a conventional vapor. By duality, there is a range of densities within region B in which there is bulk coexistence between a cluster phase and dense liquid. No reports of this in either experiments or particle-based simulations has been seen up to now.

The dynamical properties of the bubbly liquid phase (and its cluster-phase dual) are intriguing. When the noise is low bubbles are created by nucleation and destroyed by coalescence with other bubbles. At high noises, however, they can also disappear by shrinking.

In the next chapter, we analyze in details these two novel type of phase separations. In particular, beyond confirming these results, we will present some new and unexpected results, related, for example, to the time convergence to the bubbly liquid and to the bubbly phase separated state.

Chapter 2

Statistical properties of bubbly phase separation and bubbly liquid

In the previous chapter, we briefly reviewed our theoretical understanding of phase separation in active systems. In particular, we presented various evidence, from both experiments and numerical simulations, that its description in analogy with the liquid-vapor phase separation in passive systems is far from satisfactory. Furthermore, we discussed how field theoretical analysis [60] predicts that purely non-equilibrium types of phase separation should be generically expected in active systems. Specifically, we reviewed Active Model B+ (AMB+), the minimal generalization of Model B to systems where detailed balance is locally broken. This approach predicted that the Ostwald process – the main mechanism leading to the completion of phase separation in passive fluids – goes into reverse ($\sigma < 0$) at high enough activity. When this happens, the system self-organizes, depending on the global density, into a micro-phase separated state formed of vapor bubbles (or liquid clusters), or into bubbly phase separation (the coexistence of this microphase separated state with an homogeneous phase).

Yet, [60] fell short of analyzing the statistical properties of both microphase separated state and bubbly phase separation. This is the aim of the present chapter, where we performed large-scale numerical analysis of AMB+ to measure quantities such as the bubble-size distribution, and the convergence time to equilibration. In order to perform efficient simulations, we developed from scratch a parallel pseudo-spectral code that integrates Eq. (1.30).

In Sec. 2.1, we detail and motivate our choice of parameters. Then, in Sec.2.2, we confirm the phase diagram obtained in [60]. The following two sections, 2.3 and 2.4, are devoted to the in-depth study of the statistical properties of the bubbly liquid and the bubbly phase separation, respectively. In Sec. 2.4.4, we focus on the

study of the transition from the bubbly liquid and bubbly phase separation to the homogeneous liquid and vapor phases, respectively. We end the chapter with 2.5, by studying the characteristic domain growth of the density field. Details on the numerical code we developed are given in Appendix A.

2.1 Physical parameters

In this section, we present the physical parameters chosen to study AMB+ equations (1.30). Since our aim is to study the statistical properties of bubbly liquid, and bubbly phase separation in depth, we focused on a particular choice of the physical parameters. In fact, we performed a more extensive exploration of the parameter space, but this did not reveal qualitative differences with respect to the results presented here (outside the region of parameters studied in chapter 3).

Unless otherwise specified, the parameters appearing in (1.30)-(1.32) are chosen as in [60]: $K = 1, M = 1, b = -a = A = 1/4$. Instead, we varied the noise level D, the activity parameters ζ and λ, and the global density $\phi_0 = \int \phi d\mathbf{r}/V$ (that being a conserved quantity, enters the dynamics through the initial conditions). For simplicity, we restrict our study to the case of $\zeta = 2\lambda$, which is particularly easy to understand analytically, because the activity does not change the mean-field value of the binodals (as we discussed in Sec.1.6).

Since AMB+ equations are symmetric under the exchange $(\phi, \zeta, \lambda) \to -(\phi, \zeta, \lambda)$, we concentrate on $\zeta > 0$ case. As such, the reader should bear in mind that every time we write about 'vapor bubbles' in the micro-phase separated state (homogeneous bubbly phase), these results are also valid for 'liquid clusters' in the micro-phase separated state that they form, using the symmetry specified above.

We now briefly present the technical parameters used for our integration scheme. We performed simulations of (1.30) in dimension $d = 2$, for system of size $L_x \times L_y$ with periodic boundary conditions. Equations were integrated in time through a direct Euler scheme with time-step $dt = 0.02$. The spatial part of the equations was computed with a parallel pseudo-spectral code that allowed us to simulate larger systems on longer time-scales with respect to simulations of previous studies [60, 69, 51]. The space discretization is set to $dx = 1$. For a more detailed exposition, and consideration on the stability of the equations, see A.1.

2.2 Phase diagram

As a first step, we confirm the finite-noise phase diagram of AMB+ that we presented in Sec. 1.6. We indeed re-obtained it performing simulations with the pseudo-spectral code described in Appendix A.

First, we simulated systems with sizes and times comparable with the relatively modest ones used in [60] ($L_x = L_y = 192$ and $t < 10^5$). Then, we proceeded with larger system-sizes and longer times. In both cases, we could observe the same phenomenology of [60]: for low and high global densities ϕ_0 the system is found in a uniform state (vapor at low densities, and liquid at high ones). For intermediate density levels, the system phase separate between a dense phase (liquid) and

a dilute one (vapor). In order to check whether the system is actually phase separated we build the PDF of the local density $\phi(x, y)$. This quantity, that we will call $P(\phi)$, corresponds to the steady-state probability to have a density $\phi(x, y)$ in a point chosen at random. When the system is phase separated, $P(\phi)$ displays two peaks, the vapor one, at lower densities, and the liquid one. In Fig. 2.2 we see how increasing the global density ϕ_0, we have a transfer of probability from the vapor to the liquid peak. A peculiar feature, that we will discuss in more details in Sec. 2.4.4, is that while the vapor density remains constant, the liquid density varies with the global density.

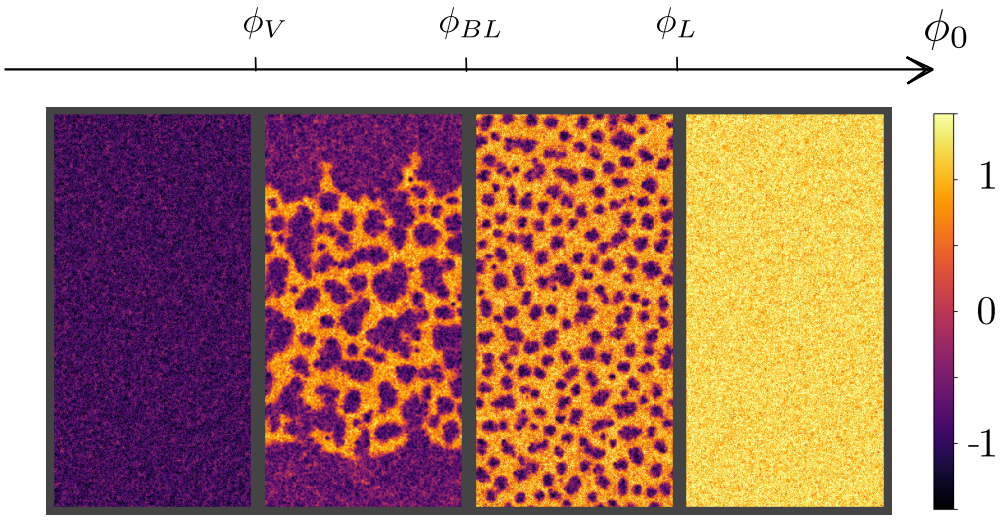

Figure 2.1: From left to right, snapshots of all the different phases of AMB+ along the line $\zeta = 2\lambda$: homogeneous vapor phase, bubbly phase separation, bubbly liquid phase, and homogeneous liquid. The definition of $\phi_V, \phi_{BL}, \phi_L$ will be provided in the next sections.
$D = 0.3, V = 512 \times 256$.

In between the two homogeneous phases, we observe the bubbly liquid at higher densities ϕ_0 and the bubbly phase separation at lower ones. Notice that the two phases cannot be discriminated by observing their $P(\phi)$. In Fig. 2.1 we present the phase diagram for $\zeta = 2\lambda = 2$, $D = 0.3$ and size 512×256, by showing the steady-state density field in the various phases we presented above. This is the equivalent of the bottom row of Fig. 1.8. The two snapshot differ for the particular choice of parameters (but both are in the region with reversed Ostwald ripening) and in the shape of the bubbly liquid phase when the system is bubbly phase separated (*i.e.* the second snapshots in both pictures). In one case is circular, in the other one is a band. This is not surprising, since normal Ostwald ripening for the liquid phase

minimize the lenght of the liquid-vapor interface, and therefore the actual shape of bubbly liquid depends on the fraction of bubbly phase in the system and the particular geometry of the system.

Being able to observe these phases confirms the validity of our code, and shows at the same time the robustness of results presented in [60], when increasing time and sizes. In the next sections, we perform an in-depth study of the statistical properties of these phases. Then, we study the transitions between them.

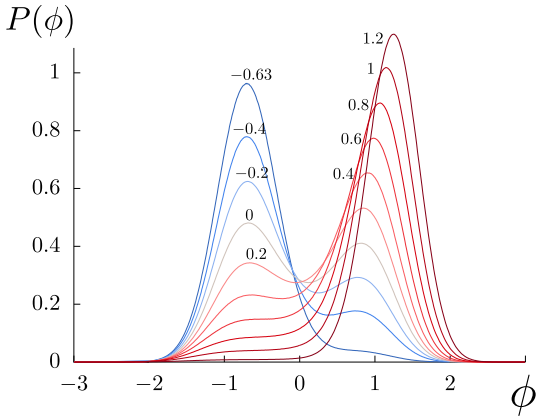

Figure 2.2: PDF of the local density $P(\phi)$ for phase-separated states at different global density ϕ_0 (shown next to each curve). We can clearly see how $P(\phi)$ displays two peaks, corresponding to the average vapor and liquid densities. Curves in blue correspond to the bubbly phase separation, red ones to the bubbly liquid. Notice how increasing ϕ_0, we have a transfer of probability from the vapor to the liquid peak, and how the latter, unlike the vapor one, shifts at larger densities (more on this in Sec. 2.4.4). Parameters are chosen as follows: $V = 512 \times 256, D = 0.3, \zeta = 2\lambda = 2$

2.3 Micro-phase separation (Homogeneous bubbly phase)

We start by studying the statistical properties of the micro-phase separated state (that we otherwise call homogeneous bubbly phase). This is a micro-phase-separated state between vapor bubbles (whose density is equal to the mean field binodals, plus correction due to the noise and the interface curvature) and a liquid background. We recall that AMB+ is invariant under $(\phi, \lambda, \zeta) \to -(\phi, \lambda, \zeta)$ so that our results equally apply to the opposite values of λ and ζ, where one finds a micro-phase separated state formed of liquid clusters. Taking this in mind, we refer below to 'vapor bubbles' for simplicity in the presentation.

The properties of this phase are determined by the relation between the reverse Ostwald ripening process and noise, whose is responsible for the nucleation and coalescence processes. In the steady state, bubbles of vapor diffuse in the liquid thanks to the presence of noise. This never ending random walk, allows bubbles to meet and merge through coalescence events. The resulting bubble has a radius R that is not in equilibrium with the outside liquid (in the sense explained in Fig. 1.6). It will therefore relax to the correct density, losing part of its volume. This allows new nucleation events to take place, following a noise-induced density fluctuation. At the same time, bubbles also interact via reverse Ostwald ripening, thus uniforming their size to the average one of bubbles around them.

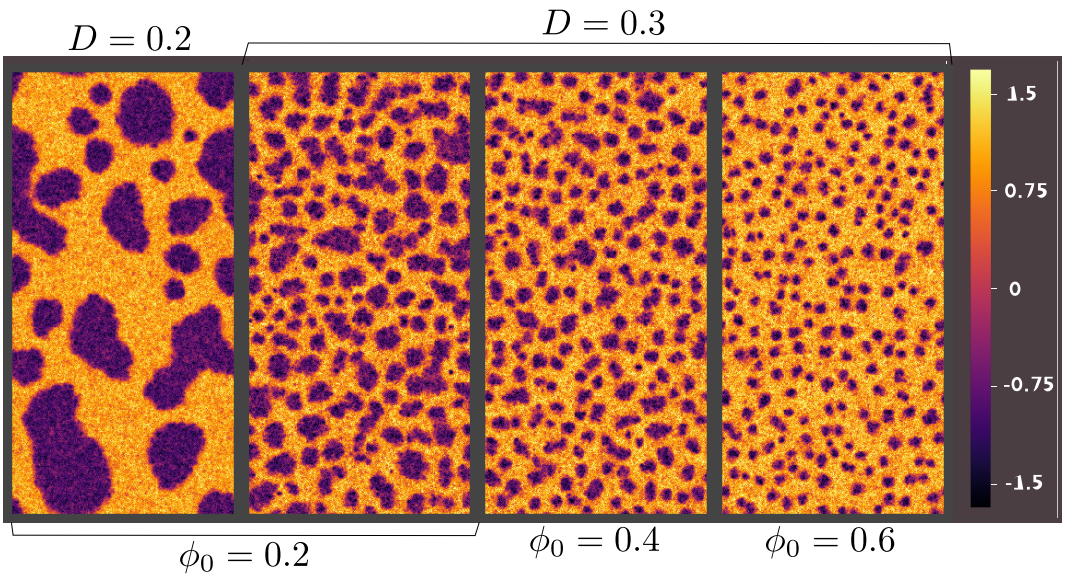

Figure 2.3: Homogeneous bubbly phase in the steady state at different noise levels D and global densities ϕ_0. System size: 512×256. We can qualitatively see how the number of bubbles, their average dimension and variability are affected by ϕ_0 and D.

When the Ostwald ripening process dominates over noise, nucleation and coalescence events happen on time-scales that are much longer then the ones needed for the Ostwald process to uniformise the size of different bubbles. In this regime, nucleation and coalescence events are rare, and all the bubbles in the system tend to have the same typical size (with a small variability). The Ostwald ripening process dominates over noise in three cases:

- When the noise level D is low. In this case bubbles diffuse slowly, and nucleation events are rare.
- For large and negative surface tension σ, where the (reversed) Ostwald process

is very fast. This happens far from to the transition line at $\sigma = 0$ of Fig. 1.7(a). On the line $\zeta = 2\lambda$ this is obtained by increasing ζ.

- At fixed parameters of AMB+, increasing the global density towards the liquid binodal makes both nucleation and coalescence more rare. If we were working on Model B, indeed, it is known that the nucleation rate diverges approaching the liquid binodal from below, and one expects a similar phenomenology here (although checking it computationally is prohibitively expensive). Moreover, increasing ϕ_0 decreases the number of bubbles, and hence coalescence is suppressed, as bubbles have to travel for longer in order to meet.

In order to quantitatively study the statistics of bubble sizes, we developed a breath-first search algorithm, see Appendix A.2. This allows to extract the bubble size distribution $P(A)$. In Fig. 2.4, we can see that when reverse Ostwald ripening dominates, $P(A)$ is peaked around the typical bubble size and decays exponentially fast away from it.

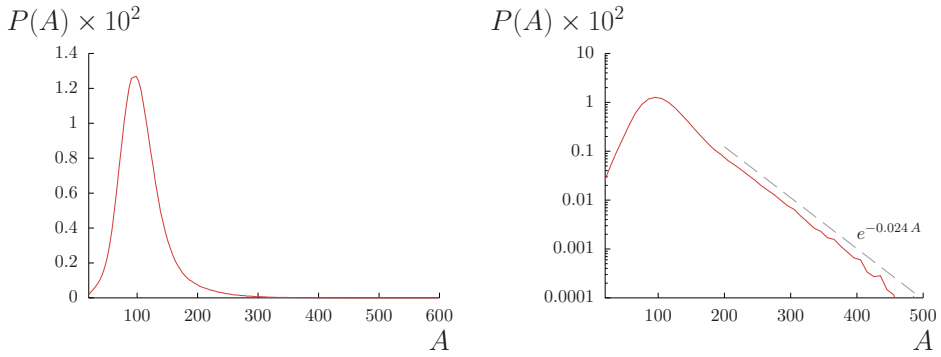

Figure 2.4: Bubble size distribution $P(A)$ in the bubbly liquid when Ostwald ripening dominates over noise: bubbles have more or less all the same size. The distribution $P(A)$ is peaked around a typical value and has exponential tail away from it. System parameters: $\phi_0 = 0.6, D = 0.3, L_x = 2L_y = 512, \zeta = 2\lambda = 2$.

If now we increase the noise, or decrease either $\zeta = 2\lambda$ or the global density ϕ_0, we do not have time-scale separation between Ostwald ripening and the coalescence processes. The typical size is less defined, and the bubble sizes variability increases. This reflects on the shape of $P(A)$: the typical size peak becomes less prominent, the variability of bubbles increases and the exponential tails are slower. In Fig. 2.5, we report the variation in shape of the bubble size distribution as we vary (one at a time) ϕ_0, $\zeta = 2\lambda$ and D. This proves the claims made above that all these three parameters allow to vary the relative strength of the Ostwald process vs coalescence and nucleation.

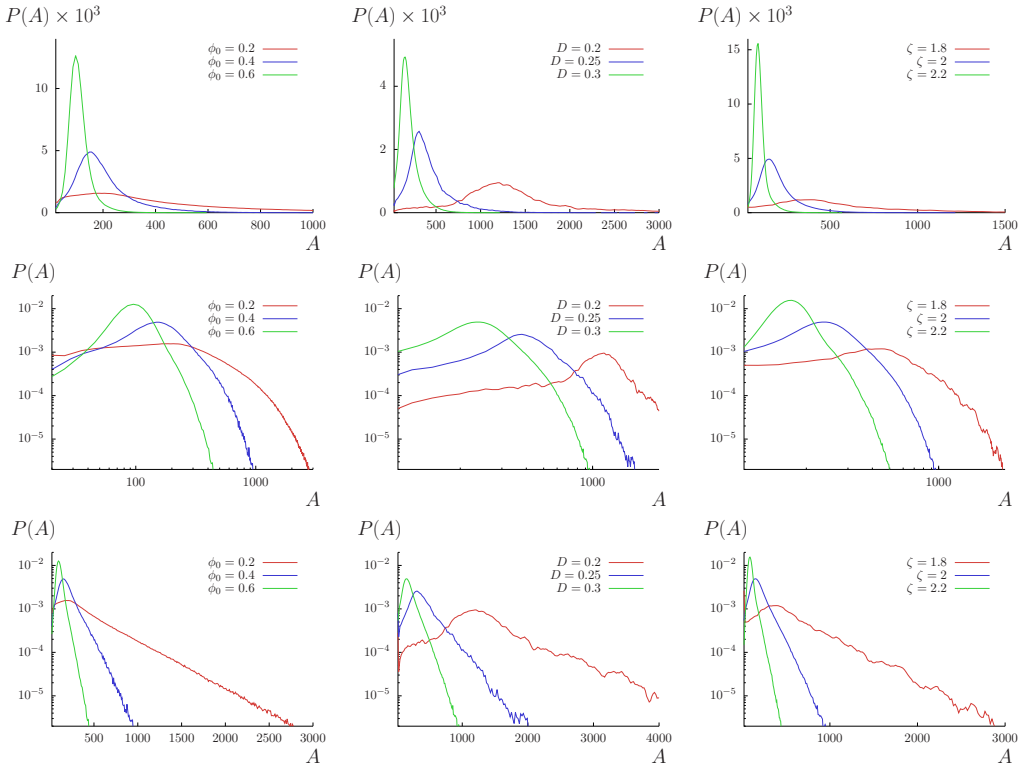

Figure 2.5: Behavior of the bubble size distribution $P(A)$ in the bubbly liquid varying ϕ_0, D and $\zeta = 2\lambda$ in the first, second and third column, respectively. From top to bottom, the different rows represent the same data in linear, log-log and log-lin scales. Notice how, the stronger is Ostwald ripening (for high values of D, ζ or ϕ_0), the more the distribution is peaked around a typical value and the variability of the bubbles size is smaller. Moreover notice (last row) that $P(A)$ has an exponential tail whose slope depends on the parameters. These were chosen as:
First column: variable ϕ_0, $D = 0.3$, $\zeta = 2\lambda = 2$, $Lx = 2L_y = 512$
Second column: $\phi_0 = 0.4$, variable D, $\zeta = 2\lambda = 2$, $Lx = 2L_y = 256$
Third column: ϕ_0, $D = 0.3$, variable $\zeta = 2\lambda$, $Lx = 2L_y = 256$

The effect of the noise level D, and of the activity term $\zeta = 2\lambda$, are not limited to the competition between the Ostwald ripening and the coalescence (and therefore to the bubble size variability). They also affect other aspects of the bubbly liquid, such as the average number of bubbles or their size (see Fig. 2.6). In particular, when D or $\zeta = 2\lambda$ increase, the average bubble number increases accordingly, while their mean size decreases.

Getting an analytical understanding of how nucleation (and anti-nucleation that

– albeit rare – is never exactly absent), bubble diffusion (and hence coalescence), and Ostwald ripening compete in order to set a typical bubble size or – even more deeply – the PDF of bubble sizes, seems out of reach. Indeed, there are several issues blocking the way. Among these, the most difficult to overcome is the analytical understanding of nucleation. More precisely, the fact that we are dealing with a system that does not have time-reversal symmetry, does not allow applying methods and concept from classical nucleation theory (well-developed for homogeneous nucleation in classical fluids). However, we will discuss in Chapter 4 a minimal model that implements all the physical ingredients described above to describe directly the dynamics and statistical properties of the bubbles.

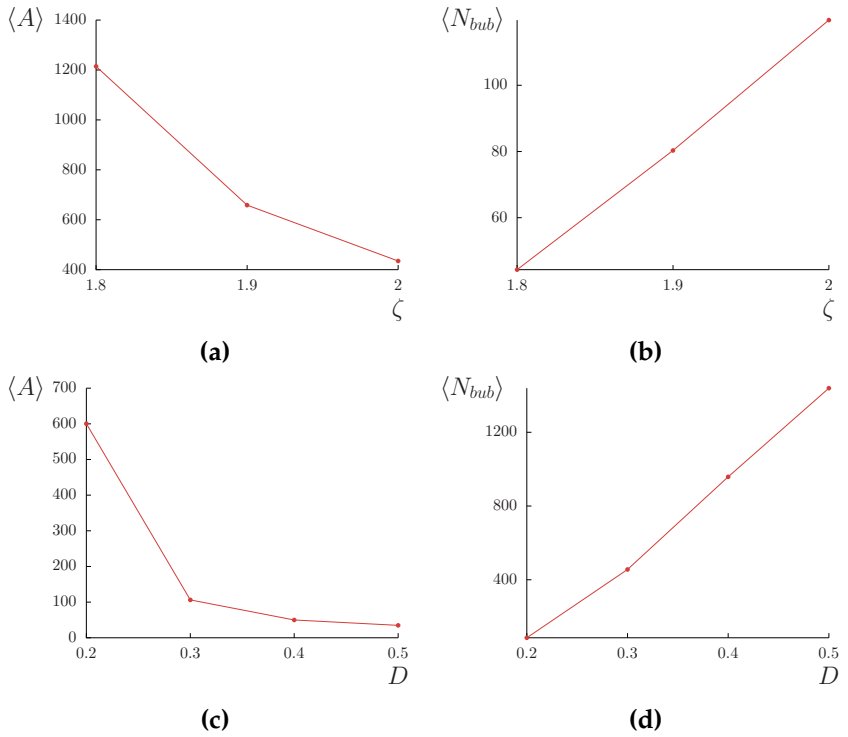

Figure 2.6: Average number of bubbles and volume in the steady-state as a function of $\zeta = 2\lambda$ and D. The chosen parameters are:
(a,b): $\zeta = 2\lambda, D = 0.3, \phi_0 = 0.2, V = 512 \times 256$
(c,d): $\zeta = 2\lambda = 2, \phi_0 = 0.6, V = 512 \times 512$

2.3.1 Varying the global density

Of particular interest is the study of the average number of bubbles in the steady state increasing ϕ_0 (Fig. 2.7(a)). Strikingly, this function is not monotonous: it increases for low values of ϕ_0, reaches a maximum value, and then decreases to

zero. In other word it exists a density ϕ_L above which no bubbles are found, and the system is not phase separated anymore. In other words, this density sets the transition from bubbly to homogeneous liquid.

To provide further proof of this fact, we studied the PDF of the local density $P(\phi)$ (red curves of Fig. 2.2). As we previously discussed, we can interpret the second peak of $P(A)$ as the typical density value of the liquid, $\bar{\phi}_l$). If we subtract to this value the global density ϕ_0 we obtain Fig. 2.7(c). The latter is clearly showing that above a certain density (1.3 for the chosen parameters), $\bar{\phi}_l = \phi_0$. In other words, we no longer have two phases but just the liquid one: the system is homogeneous. In Sec. 2.4.4, we investigate the asymptotic behavior of ϕ_L by increasing the system size.

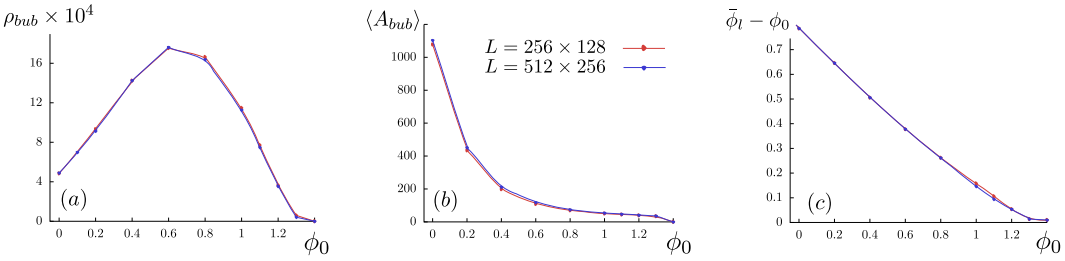

Figure 2.7: Some features of the bubbly liquid as a function of the global density for two different sizes. Noise level $D = 0.3$ in all the cases.
(a) Density of bubbles $\rho_{bub} = N_{bubbles}/V$.
(b) Average bubble area in the steady state.
(c) Distance of the typical liquid density $\bar{\phi}_l$ (second peak of Fig. (c)) from ϕ_0. It becomes zero when the system is in the homogeneous liquid phase.

2.3.2 Convergence in time and system size

So far, we have presented results for a fixed system-size ($L_x = 2L_y = 512$ and 256). We now study the convergence, both in time and system-size when the system goes towards the micro-phase separated state. As we will see in the following, there is a very strong difference between this case and the bubbly phase separated one. For the moment, we only focus on the first case.

We estimate the typical time for convergence to the steady state τ_{ss} by looking at the time-series of the number of bubbles $N_{bub}(t)$. More specifically, to compute τ_{ss}, we first obtain the average number of bubble $\langle N_{bub} \rangle$ in the steady-state and its standard deviation ΔN_{bub}. Then, we evaluate τ_{ss} as the first time $N_{bub}(t)$ enters the interval of width ΔN_{bub} around $\langle N_{bub} \rangle$ (see Fig. 2.8). In order to disregard significant noise fluctuation, we performed this analysis on a smoothed time series, obtained through a moving average.

When the system heads towards micro-phase separation, the convergence in

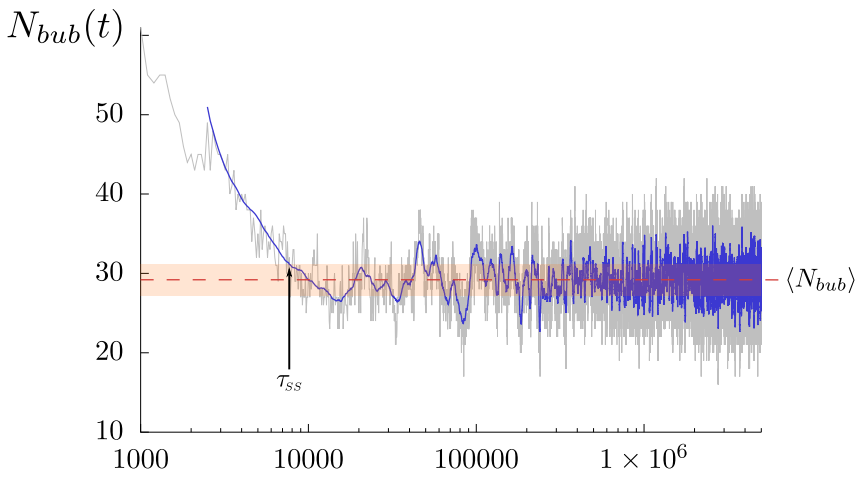

Figure 2.8: Example of a time series of the number of bubble in the bubbly liquid, before (gray) and after (blue) the smoothing process though a moving average. The convergence time τ_{ss} is computed as the first passage time of $N_{bub}(t)$ in the interval $[\langle N_{bub} \rangle - \Delta N_{bub}, \langle N_{bub} \rangle + \Delta N_{bub}]$ where $\langle N_{bub} \rangle$ is the steady-state average of the number of bubbles and ΔN_{bub} its standard deviation.

time is fast and practically independent of the system-size simulated (see Fig. 2.17(a,b)). This makes the statistical analysis of the homogeneous bubbly liquid a relatively easy task. To study the convergence in system-size, we compared time-series for different system sizes and check that they converge all to the same average value, on the same typical time-scale. In the steady-state we expect to have a system-size independent $P(A)$ once convergence in the system size is achieved. The latter is attained at relatively small system size (with respect to what we can comfortably simulate with our code, and also compared to the bubbly phase separation, as we will see in Sec. 2.4.1). See Fig. 2.9 for some examples.

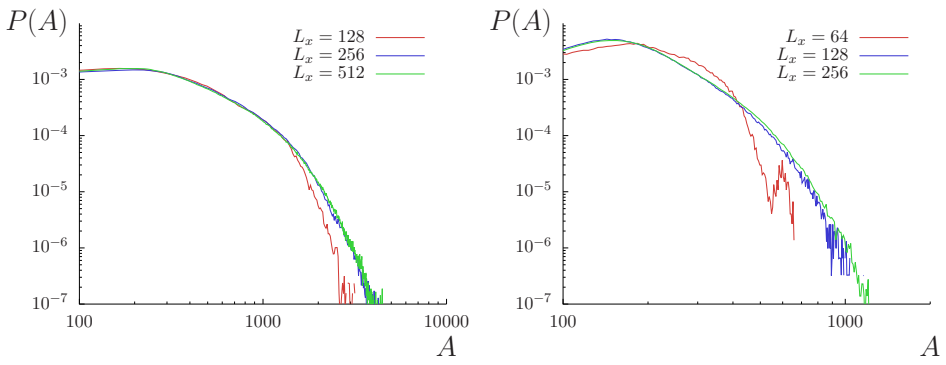

(a) $\phi_0 = 0.2$ **(b)** $\phi_0 = 0.4$

Figure 2.9: Convergence is system size of the bubble size distribution $P(A)$ in the bubbly liquid. As we can see, the system tends to converge in size faster for $\phi_0 = 0.4$, where the distribution has shorter tails. Parameters: $\zeta = 2\lambda = 2, D = 0.3$

2.4 Bubbly phase separation

At low density, we find the bubbly phase separation: a bulk phase separation between the bubbly liquid at density ϕ_{BL} and a uniform vapor phase, in the form of a macroscopic vapor reservoir (examples of the steady-state density field are given in Fig. 2.10). The latter, in particular, is fundamentally different from a vapor bubble. Indeed, even though they are both composed by vapor at the same density (up to correction of order $1/R$ as we saw in Sec.1.6), its size scales linearly with the system-size, and its presence is persistent in time. In other words, the bubbly liquid at density ϕ_{BL} occupies a volume V_{BL} of the system , while vapor at a density ϕ_V occupies the rest of the volume $V_V = V - V_{BL}$ respecting the *lever rule*, that imposes the conservation of the global density ϕ_0:

$$\phi_0 V = \phi_{BL} V_{BL} + \phi_V (V - V_{BL}) \tag{2.1}$$

This means that, exactly like in every bulk phase separation, varying ϕ_0 from ϕ_V to ϕ_{BL}, the system is found in a bubbly phase separated state with the volume of bubbly liquid that goes from 0 to V (the volume of the vapor reservoir, conversely, goes from V to 0).

The aim of the present section is to show that this state is indeed a bona-fide phase separation between the micro-phase separated state and the homogeneous vapor phase (that was hypothesized, but not proved, in [60]). Moreover, we will discuss the surprising fact that the convergence in time to the bubbly phase-separated state, is extremely slow, and dramatically increases with system-size.

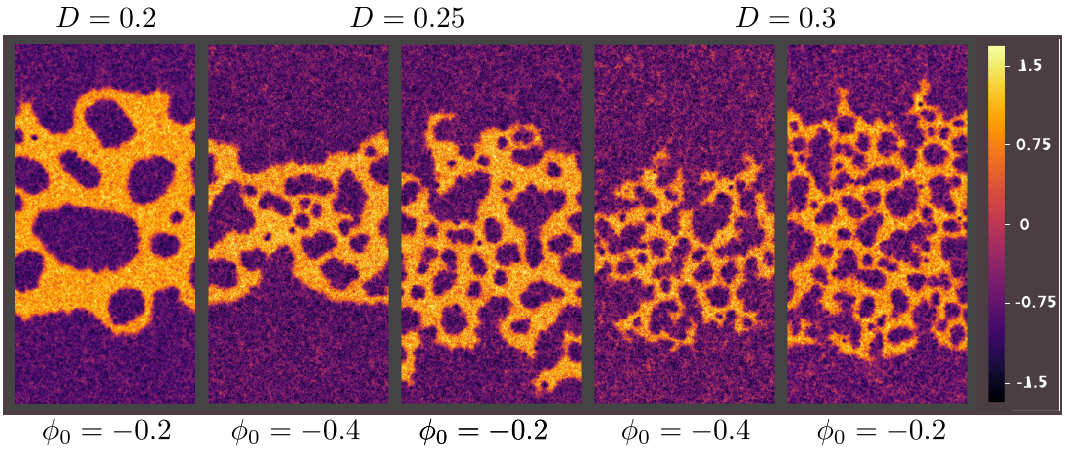

Figure 2.10: Snapshot of BPS for two noise and ϕ_0 values. System size 512×256.

Proving this point is somehow delicate: while the density of the vapor reservoir is uniform (in the sense that is given by the mean-field vapor binodal plus noise-induced fluctuations), the bubbly liquid is, itslef, microphase separated between the pure liquid and vapor bubbles. In order to obtain reliable results, we thus need to use system-sizes that are much larger than the largest bubble observed in the bubbly liquid. This is a very demanding task. Thanks to the efficient parallel pseudo-spectral code that we developed, we were able to overcome this difficulty.

We considered systems in a rectangular geometry $L_x \times L_y = L_x/2$. This is convenient because, when the system is phase separated, it presents a flat (on average) interface between the micro-phase separated state and the vapor, which allows to easily compute the average density within the bubbly liquid as a function of the vertical coordinate y (see Fig. 2.11). We refer to this geometry saying that the system forms a 'band'. More precisely, we compute ϕ_V and ϕ_{BL} projecting the local density $\phi(x, y)$ along the x-direction:

$$\phi(x,t) = \frac{1}{L_y} \int_0^{L_y} \phi(x,y,t) \tag{2.2}$$

Further averaging $\phi(x,t)$ over time, we obtain a smooth profile $\phi(x) = \langle \phi(x,t) \rangle$ (see Fig.2.11). The two densities ϕ_V and ϕ_{BL} are then easily distinguishable, meaning that the typical fluctuations within one of the two phases is much smaller than the density difference between the vapor and the bubbly liquid.

If we are really in front of a phase-separated system, both ϕ_{BL} and ϕ_V must be independent both from the global density and system-size when the latter is large enough. This is what we prove in Fig. 2.12. It should be noted that obtaining these results needed a considerable computational effort: the simulations at $L_x = 1024$, even using our parallel pseudo-spectral code, run for a few months (we will discuss

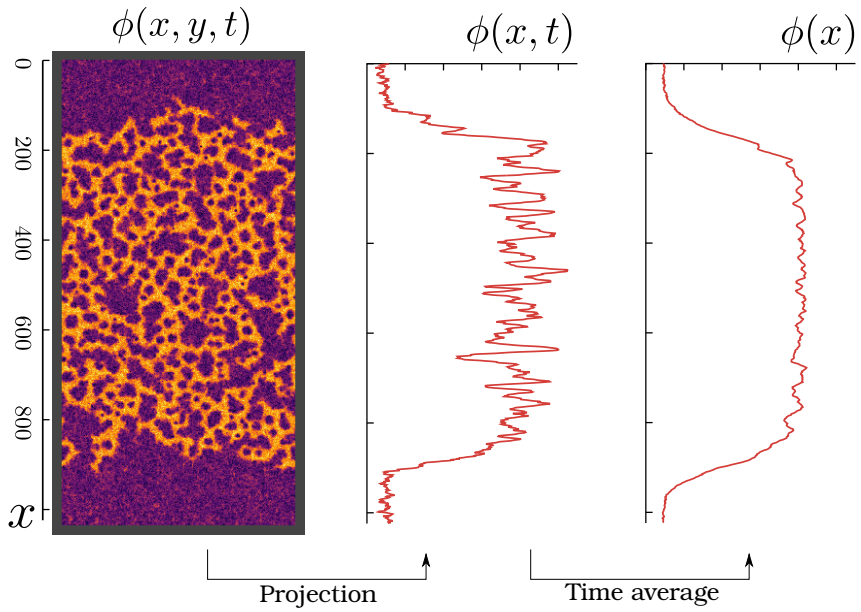

Figure 2.11: In this figure we show how is possible to extract the smoothed band profile $\phi(x)$ of the bubbly phase separated state, starting from the density field $\phi(x,y,t)$. First, we extract the density profile of a single time t by projecting the local density $\phi(x,y,t)$ along the $x-$axis. Then, we averaged over time $\phi(x,t)$ to smooth the profile. In this way we get: $\phi(x) = \langle\phi(x,t)\rangle$.

more in details below why this was necessary). In conclusion, we confirmed the expectation that bubbly phase separation is – indeed – a phase separation between the outside vapor region and a microphase separated bubbly liquid.

2.4.1 Convergence in time

We now study convergence in time to the bubbly phase separated state, and we compare it to the one found when heading towards the homogeneous bubbly liquid. A quantity that will provide useful to do so is the average density of the bubbly liquid as a function of time $\phi_{BL}(t)$. Indeed, unlike standard liquid-vapor phase separation, the dense phase, whose density is $\phi_{BL}(t)$, is itself microphase separated and the interface between the two phases is not easily defined: it has frequent large fluctuations and overhangs. Measuring it is not obvious at first sight; before discussing the convergence in time and system size, we thus describe precisely our procedure.

We have followed two procedures to measure $\phi_{BL}(t)$. In the first method, we average the density in all the system but the vapor reservoir. In order to do so, we locate the vapor reservoir using a *breath first search* algorithm (see Appendix A.2) and then we average the density field outside it. The second, more refined

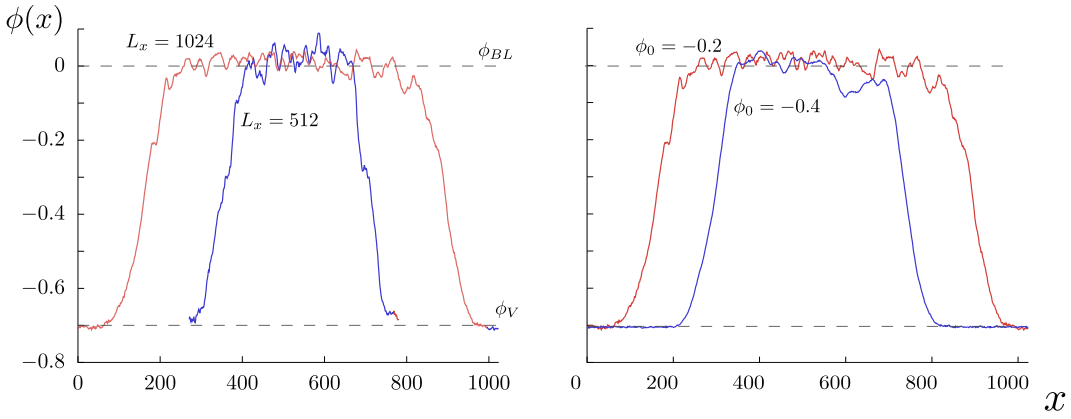

Figure 2.12: Average density profile (obtained as explained in Fig. 2.11) in the bubbly phase separation. We can clearly distinguish the two density levels of the bubbly-liquid ϕ_{BL} and of the vapor ϕ_V. These do not depend on the global density ϕ_0, nor on the system size (when chosen large enough). Simulation parameters: $D = 0.3$. Left: $\phi_0 = -0.2$. Right: $L_x = 2L_y = 1024$

method, relies on the projection of the density field along the x-axis $\phi(x)$ (as defined in equation (2.2) and Fig. 2.11). It consists in extracting $\phi_{BL}(t)$ from the local field $\phi_{x,y}$ projected along the axis perpendicular to the band (this will work just for rectangular geometries), providing us the band profile. From there, we can perform an average in the inner part of the bubbly liquid. This allows us to disregard the interface and therefore to have more reliable estimates of $\phi_{BL}(t)$ (see Fig. B.2) as:

$$\phi_{BL}(t) = \frac{1}{w} \int_{x_1}^{x_1+w} \phi(x,t)\,. \tag{2.3}$$

More details are given in Appendix B.2.

In Fig. 2.13 we provide a comparison between the two methods to compute $\phi_{BL}(t)$. They give qualitative consistent results. As expected, however, the first method leads to a systematic overestimation since we are including the interface between the micro-phase separated state and the vapor, which is much broader than the liquid-vapor interface.

We now pass to discuss the convergence in time towards the bubbly phase separated state, comparing it to the case where it converges to micro-phase separation. As for the bubbly liquid, we can compute the convergence time τ_{ss} using the time-series of the number of bubbles. However, for the bubbly-phase separation we can also rely on the average density of the bubbly liquid $\phi_{BL}(t)$. In Fig. 2.14, we show the comparison between the two time-series for the same system; As we can see, they provide a consistent estimate of the convergence time (about 2×10^7).

The convergence towards bubbly phase separated state, is strikingly different from the one to the bubbly liquid. While, as already discussed in Sec. 2.3.2, τ_{ss} is

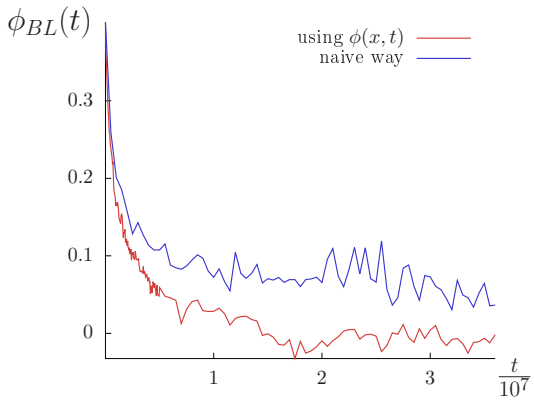

Figure 2.13: Comparison between the two methods used to compute the average density of the bubbly liquid $\phi_{BL}(t)$ in a bubbly phase-separated state. In blue the simplest that consist in averaging the density in all the system but the vapor reservoir (this method overestimates $\phi_{BL}(t)$). In red the method that relies on the band profile $\phi(x)$ as described in the text.

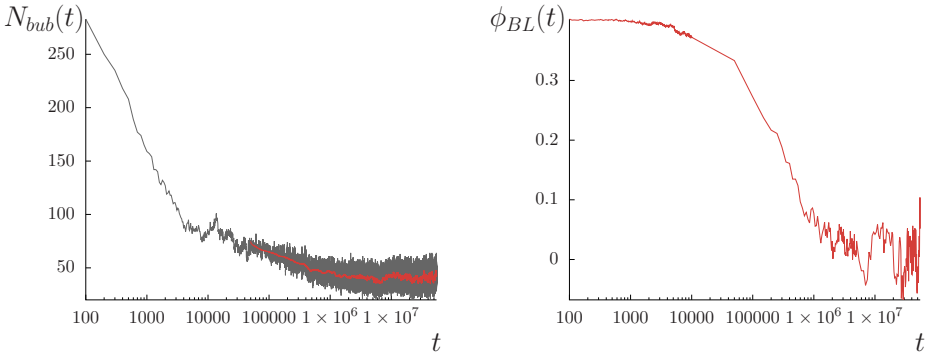

Figure 2.14: Time series of the number of bubbles (left) and of the average density inside the bubbly liquid (right) for the bubbly-phase state. Both time series can be used to estimate the convergence time τ_{ss} after which the system is in the steady-state. Parameters are chosen as follows: $D = 0.3, L_x = 2L_y = 1024, \zeta = 2\lambda = 2$.

independent of system size when converging towards the bubbly liquid, it depends on it very strongly when the system is converging to a bubbly phase separated state. In this case, varying the system-size between 256×128 to 1024×512, we roughly estimate that τ_{ss} increases linearly with the system volume. Importantly, the same result is obtained starting from both uniform or band initial conditions (see Appendix C.1 for a precise definition of the initial conditions). In Fig. 2.17(d), we compare these two cases and show that the asymptotic values are the same. Once again: obtaining results converged in time up to system size 1024×512 was a con-

siderable computational effort. For example, it took few months for the simulation of size 1024×512 to reach times of order 10^7.

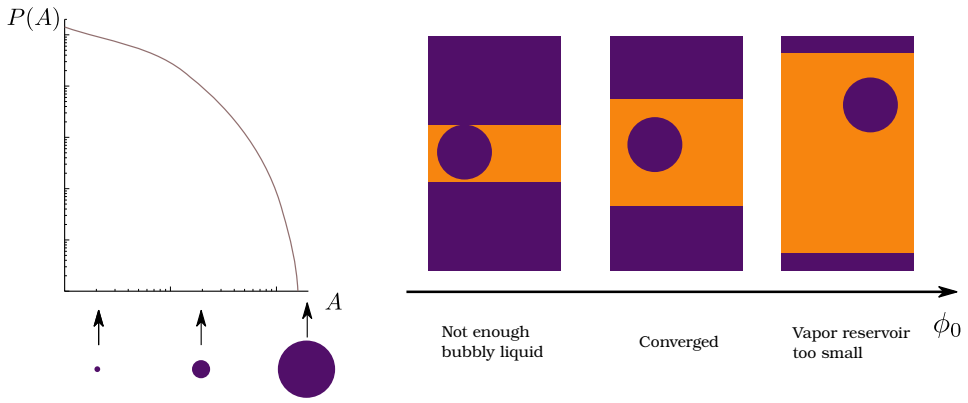

Figure 2.15: Sketch explaining the convergence in system size in the bubbly phase separation. Let $P(A)$ be the converged bubble size distribution for a certain set of parameters. If now we consider a given system-size, and a certain global density ϕ_0, we fix both the volume of the vapor reservoir and of the bubbly liquid. Then, if ϕ_0 is too low (first system from the left) then the volume of the bubbly liquid is not enough to accommodate the biggest bubble of $P(A)$; therefore, for that particular size, its bubble size distribution has shorter tails. On the contrary, when ϕ_0 is too large (third snapshot), the vapor reservoir has size comparable with the biggest bubbles of the bubbly liquid. In other words, we cannot distinguish its state from the bubbly liquid one.

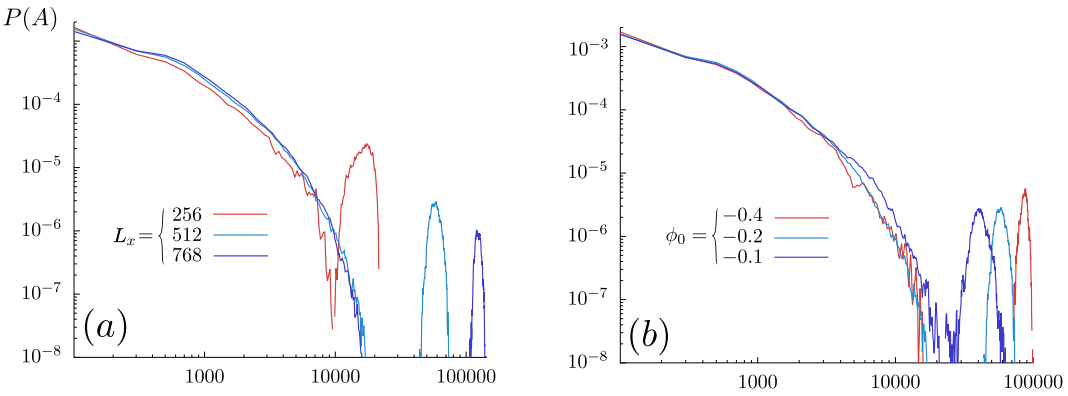

Figure 2.16: System size convergence of the bubble size distribution $P(A)$ for $D = 0.25$ and $\zeta = 2\lambda = 2$.
(a) P(A) converging in system size for $L_x = L_y/2 = 512$.
(b) Converged $P(A)$ for different global densities.

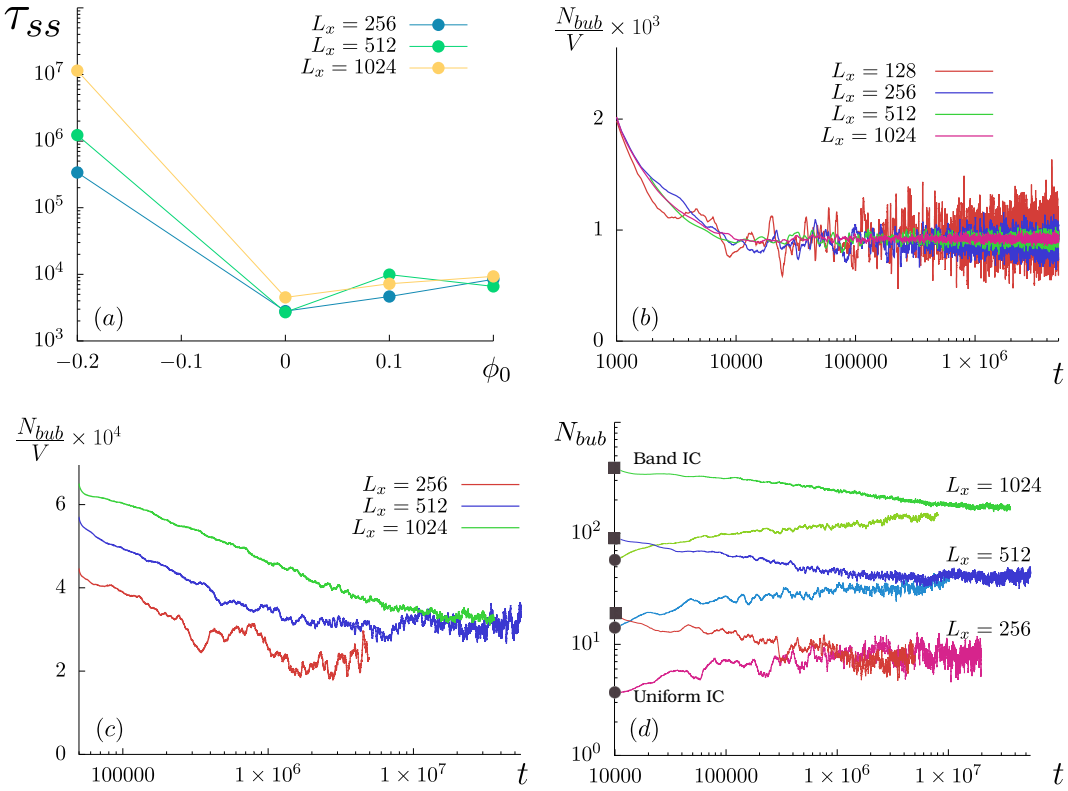

Figure 2.17: Convergence time τ_{ss} and some time-series from which it was computed. $D = 0.3$, $L_x = 2L_y, \zeta = 2\lambda = 2$.
(a) Convergence time τ_{ss} as a function of ϕ_0 and system size $L_x = 2L_y$. In the bubbly liquid ($\phi_0 > 0.01$) it does not depend much on system size, while in the bubbly phase separation the dependence is dramatic. Initial conditions: bubbly liquid: uniform ($\phi(x, y) = \phi_0$), bubbly phase separation: band of uniform liquid in a vapor background.
(b) Number of bubbles per unit volume in the bubbly liquid ($\phi_0 = 0.2$). The convergence time is clearly system-size independent.
(c) Number of bubbles per unit volume in the bubbly phase separation ($\phi_0 = -0.2$) for different system size. It clearly increases dramatically with L_x
(d) Number of bubbles versus time for different system sizes L_x and initial conditions (band and uniform). With this plot we check that the system-size dependence of τ_{ss} in the bubbly phase separation was not an artifact due to the different initial condition employed.

2.4.2 System size convergence

The convergence in time towards bubbly phase separation is even more striking, given that our results are converged in system-size. We dedicate this section to prove this point more rigorously with respect to Fig. 2.12, showing the density

D	ϕ_{BL}	ϕ_V
0.2	0.21	-0.84
0.25	0.15	-0.77
0.3	0.01	-0.70

Table 2.1: Average density of the vapor reservoir and of the bubbly liquid for system converged in time and size. $\zeta = 2\lambda = 2$.

profiles at different sizes and global densities.

As we saw already for the micro-phase separated state (Sec. 2.3.2), the most stringent test of system-size convergence is provided by comparing the steady-state PDF of bubble size $P(A)$, that we now analyze. Moreover, we complement this check by inspecting the time series of the number of bubbles and the average density in the bubbly liquid ϕ_{BL}. Having limited computational resources, we had to choose carefully the global densities ϕ_0 at which we run our simulations. In Fig. 2.15 we explain why, in general, we used intermediate densities that were sufficiently far from the transitions to the bubbly liquid and the homogeneous vapor phase.

The bubble size distributions $P(A)$ in the bubbly phase separation, are composed by two separates part (Fig. 2.16). One, at smaller sizes, relative to bubbles in the bubbly liquid. The other, at a separated, larger scale, concerns the vapor reservoir (seen as a big bubble by our algorithm to locate bubbles). Once the system-size convergence is attained, the distribution relative to bubbles in the bubbly liquid, is independent of system size, and of the global density ϕ_0. On the contrary, by increasing the volume of the system, the peak at large sizes shifts to larger sizes accordingly. This is somehow obvious in the context of a bulk phase separation, as the average volume occupied by the vapor reservoir scales linearly with system volume (this can be directly obtained from the lever rule in Eq. (2.1)). In Fig. 2.16 we can see the converged bubble size distribution $P(A)$ for noise level $D = 0.25$.

All these expectations are confirmed: the part of the $P(A)$ corresponding to the bubbly liquid does depend neither on the system size nor on the global density ϕ_0, and the peak describing the outer vapor scales linearly with system size.

A particularly strong form of system-size dependence is found setting the global density close to ϕ_{BL}, the density of the bubbly liquid when the system is globally in a bubbly phase separated state (see next section for an in-depth discussion of ϕ_{BL}). In Fig. 2.18, we report results for $\phi_0 = 0$. At small system sizes, the system is found in a microphase separated state. In such a regime, we find that the bubble PDF has an intermediate power-law regime $P(A) \sim A^{-\alpha}$, with $\alpha = 1.5$. Increasing system size, as far as $\phi_V < \phi_0 < \phi_{BL}$, the system settles in a bubbly phase separated state. We show similar intermediate power laws in Fig. 2.19 for smaller noise levels. The main differences with the previous case are the exponent α, here equal to 1.5, and the persistence of this state in the asymptotic regime.

As we write this text, we still do not have an analytical understanding of how and when these power laws arise. Interesting physics may be understood by studying analytically this problem, and future studies may shed light on their emergence.

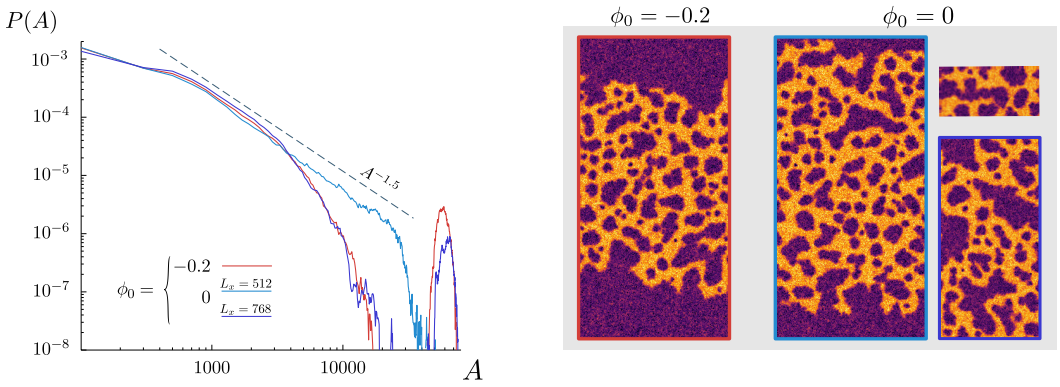

Figure 2.18: **Left:** intermediate power law of the bubble size distribution $P(A) \sim A^{-1.5}$ for $D = 0.25, \phi_0 = 0, L_x = 512 = 2L_y$. Notice how we pass form a bubbly liquid state for small sizes (less than 512×256) to a bubbly phase separated state by increasing system size. In red we represent for comparison the converged $P(A)$ of the bubbly liquid state at $\phi_0 = -0.2$.
Right: snapshot of the density field in the steady-state for the same systems on the left side. At $\phi_0 = -0.2$, the state is converged in time and system size. For $\phi_0 = 0$ we can see various sizes ($L_x = 2L_y = 1024, 512, 256$), and how we pass from a bubbly state to a bubbly-phase separated one.

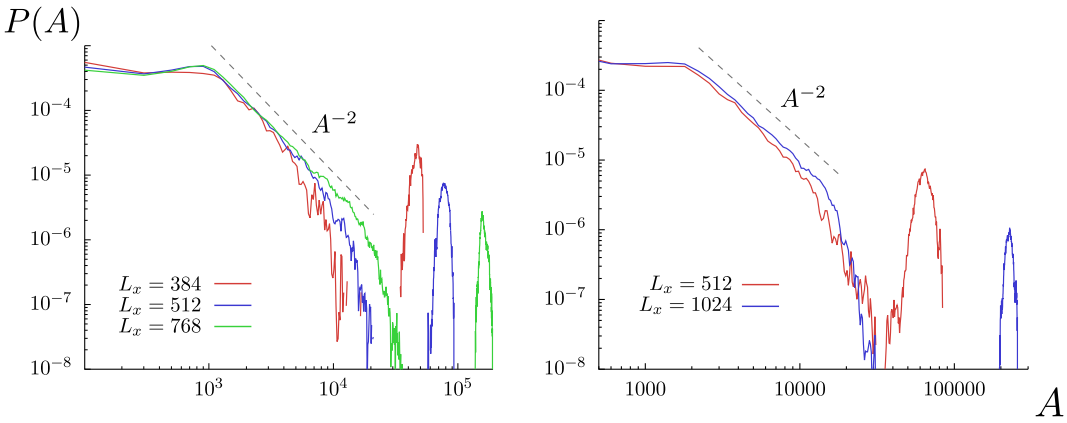

Figure 2.19: This is the bubble size distribution $P(A)$ for the bubbly phase separation, showing an intermediate power law $P(A) \sim A^{-2}$. Simulations parameters:
Left: $\zeta = 2\lambda = 2.4, \phi_0 = -0.3, D = 0.17$
Right: $\zeta = 2\lambda = 2.4, \phi_0 = -0.2, D = 0.2$

2.4.3 Estimating ϕ_{BL}

As we have seen before, the microphase separated state exists only at high enough densities, and it is replaced by bubbly phase separation at lower densities. Although it is obviously very difficult to locate the precise transition value of the density, all our measurements are compatible with the natural expectation that it corresponds to ϕ_{BL}, the value of the density of the bubbly liquid when the system is, globally, bubbly phase separated. In this section, in order to estimate ϕ_{BL}, we study the time-series of the average density inside the bubbly liquid (*e.g.* see $\phi_{BL}(t)$ of Fig. 2.14). Once we determine when the system is in its steady state, we average $\phi_{BL}(t)$ over time to obtain an estimate of ϕ_{BL}.

2.4.4 Computing liquid and vapor densities

We now look more in details to the transitions towards the homogeneous liquid and vapor phases. In particular, at low density we study the transition of the bubbly phase separation towards the homogeneous vapor phase (by decreasing global density ϕ_0). At higher densities, instead, we study the transition of the bubbly liquid towards the homogeneous liquid phase (by increasing ϕ_0). We refer to these transition density as ϕ_V and ϕ_L, respectively. Between these two transitions, the one at low density is the easiest to understand. As we explained already, the bubbly phase separation is a bulk phase separation between two phases with defined densities: ϕ_V for the vapor reservoir, and ϕ_{BL} for the bubbly liquid. Therefore, for global densities below ϕ_V we only have the vapor phase. To determine ϕ_V we have various choices.

A first way to estimate ϕ_V is to exploit the PDF of the local density field $P(\phi)$ (some examples are reported in Fig. 2.2). It must be noted, however, that $P(\phi)$ contains information on the vapor reservoir but also on the bubbles in the bubbly liquid. No matter how big the system is, a fraction of the total vapor is contained in small bubbles living inside the bubbly liquid. The latter, as we saw in Sec. 1.6, are expected to have a density that is equal to the mean field binodal ϕ_1 plus correction of order $1/R$ (the inverse of their radius R). Hence, we expect this method to be affected by systematic errors.

A second possibility is to compute ϕ_V as the average density of the vapor reservoir, when the system is bubbly phase separated. In practice, we can easily isolate the latter using the algorithm to locate bubbles described in the Appendix A.2.1. At small sizes this measurement is affected by the presence of the interface, for which density values range from liquid to vapor levels. As the system size grows, however, the interface becomes quickly much smaller than the volume of the system and the estimate of ϕ_V becomes more and more reliable.

In Fig. 2.20 we show that the two methods described above give consistent results with a systematic bias in the estimation via $P(\phi)$. In Table 2.1, we report our estimates of ϕ_V for different noise value at $\zeta = 2\lambda$: as expected, the highest the noise, the further away ϕ_V is from its mean-field value ($\phi_V = \phi_1 = -1$).

The estimation of ϕ_L in systems with finite noise is considerably harder. In Sec. 2.3, we saw that for a given size, we have a transition to the homogeneous liquid phase above a certain density. The latter can be extrapolated by studying the dependence of observables like the average number of bubbles in the steady state on ϕ_0(Fig. 2.7). The next step is to understand how this density behaves in the limit of infinite time and system-size.

In equilibrium phase separation, the transition towards the homogeneous liquid takes place at a particular global density, which corresponds to (i) the average liquid density in bulk phase separated systems; (ii) the second peak of the PDF of the local density $P(\phi)$; (iii) the density at which the nucleation time-scale diverges.

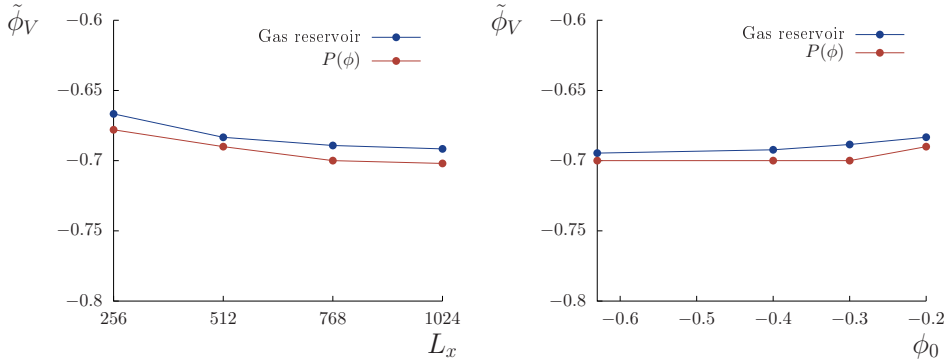

(a) $\phi_0 = -0.2$ **(b)** $L_x = 512$

Figure 2.20: Estimate $\tilde{\phi}_V$ of ϕ_V using the two methods described in the text, and their behavior changing ϕ_0 and system size. $D = 0.3, L_x = 2L_y$

It is natural to ask whether, in AMB+, one has a similar interpretation for the density beyond which the system forms a homogeneous liquid. As we shall see, the situation is more complex when Ostwald ripening is reversed. First, it is clear that (i) above cannot be generalized to AMB+ when Ostwald ripening is reversed, because the system is micro-phase separated.

Even (ii) cannot be exploited. Indeed, in the bubbly liquid the second peak of $P(\phi)$, corresponding to the typical liquid density, is not constant with ϕ_0, presenting a clear shift as we increase the global density (see Fig. 2.2 and Appendix B.1 where we check the stability of these results with time resolution). This behavior can be easily explained through the following mean field argument. In Sec. 1.6, we saw that for noiseless systems, the steady-state density of the liquid outside a bubble depends on the bubble radius R, and hence on its size. When the system is in the bubbly liquid state, the size of bubbles decreases when increasing ϕ_0. Hence, the liquid density is expected to increase as a function of ϕ_0. Notice that this mean-field understanding cannot be used to conclude whether there is a finite value of ϕ_0 beyond which no bubble is found (homogeneous liquid). Indeed, as explained in Sec.1.6, the correction to the binodals is known analytically only perturbatively in $1/R$. Hence, such information cannot be extrapolated up to $R = 0$.

The last available route (iii) is to extrapolate ϕ_L from the divergence of the nucleation time. This task, however, is computationally hard even for equilibrium systems as one is looking for the divergence of the typical time of a rare event to occur [5]. For these reasons, even at equilibrium, we could not obtain clean results computationally. As a further layer of complexity, we have that out of equilibrium, we lack the same analytical understanding of nucleation similar to the *Kramer's rate*.

2.5 Phase ordering kinetics

Domain coarsening induced by a temperature quench (phase ordering kinetics), has been studied for over 50 years (see the review of Bray [6]) . One of the main point addressed by these theories is the domain growth of the different phases in the system. The theory relies on the so-called scaling hypothesis that assume the existence, at late times, of a single characteristic length scale $L(t)$ such that the domain structure is statistically independent of time when lengths are scaled by $L(t)$. Given the density field $\phi(\boldsymbol{r}, t)$, the characteristic length is computed relying on the of structure factor $S(\boldsymbol{q}, t)$, defined as Fourier transform of the correlation function:

$$C(\boldsymbol{r}, t) = \langle \phi(\boldsymbol{x} + r, t)\phi(\boldsymbol{x} + r, t) \rangle \tag{2.4}$$

being therefore equal to:

$$S(\boldsymbol{q}, t) = \langle \phi(\boldsymbol{q})\phi(-\boldsymbol{q}) \rangle \tag{2.5}$$

where angle brackets indicate an average over different realization. The existence of a single characteristic length scale, implied by the scaling hypothesis, is equivalent to say that the correlation function and the structure factor have the following scaling forms:

$$C(r, t) = f(r/L) \tag{2.6}$$
$$S(q, t) = L^d g(qL) \tag{2.7}$$

where $g = \mathcal{F}[f]$. For this reason we are typically interested in the structure factor $S(q, t)$, obtained by averaging $S(\boldsymbol{q}, t)$ over shells of radius $q = |\boldsymbol{q}|$:

$$S(q) = \langle |\phi(\boldsymbol{q})|^2 \rangle_q \tag{2.8}$$

Finally, the typical length scale can be estimated as the inverse of the first moment of $S(q)$:

$$L(t) = 2\pi \frac{\int S(q)dq}{\int qS(q)dq} \tag{2.9}$$

In the classical phase-separated system the characteristic domain size grows as a power law of the time and $L(t) \sim t^\alpha$, where the exponent α depends on the transport properties of the system. In particular, for diffusive systems with conserved fields (*i.e.* the one described by Model B) it was firstly shown by Liftshitz [70] that, for extremely off-critical systems (ϕ_0 far from zero), $\alpha = 1/3$. In these systems, bubbles are scarce and so are coalescence events. The principal growing mechanism is therefore the direct Ostwald ripening process. It was shown later on (by Siggia [71]) that the coalescence mechanism generates the same exponent. This is due to the fact that diffusion processes limit the speed of the ordering kinetics in both cases. After more than 20 years of debate since the first Liftshitz paper, Huse [72] extended

the Liftshitz-Slyosov theory to cases presenting a bicontinuos structure of vapor and liquid (ϕ_0 is around zero in the language of Model B). In other words, the theory was extended to cases in which the two phases occupy a comparable volume fraction. His argument goes like this: along the interfaces the chemical potential scales as $\mu \sim \sigma/L$, varying over a length scale of order L. The current, and therefore the interface velocity v, scales as $\nabla\mu \sim \sigma/L^2$, giving $dL/dt \sim \sigma/L^2$ and finally $L(t) \sim (\sigma t)^{1/3}$.

For active systems the debate is still ongoing. A recent example comes from Pattanayak and his group [69], claiming that the growth of $L(t) \sim t^\alpha$ for Active Model B presents a crossover between an early time Liftshiz-Slyosov exponent $\alpha = 1/3$ to a $\alpha = 1/4$ at later times. This result is surprising, as it was obtained when $\zeta = 0$, in the case where Ostwald ripening is normal and hence there seems to be no obvious mechanism leading to a late-time $1/4$ growth law.

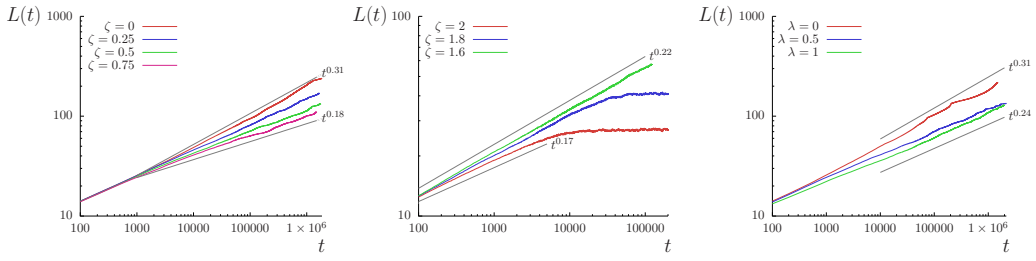

(a) $D = 0, \zeta = 2\lambda$ **(b)** $D = 0.3, \zeta = 2\lambda$ **(c)** $D = 0, \zeta = 0$

Figure 2.21: Characteristic length scale $L(t)$ growth in time. It displays a power law that depends on the activity. System size 1024×1024, global density chosen as the midpoint between mean-field binodals $\phi_0 = \frac{\phi_2 - \phi_1}{2}$. In particular: (a,b) $\phi = 0$ and (c) $\phi_0 = 0, 0.06, 0.12$ for $\lambda = 0, 0.5, 1$, respectively.

We would like now to present our attempt to understand their results in the more general setting of AMB+. Simulations were done on square systems of size $L_x \times L_x$, starting from a random initial condition for a global density equal to the mid-point of the mean-field binodals $\phi_0 = \frac{\phi_1 + \phi_2}{2}$. We simulated system on our usual $\zeta = 2\lambda$ line, as well of the line corresponding to AMB ($\zeta = 0$), to compare with [69]. As we can observe in Fig. 2.21, it seems from our results that the stronger is the activity, the smallest is the speed of domains growth. This results in an apparent power law growth $L(t) \sim t^\alpha$ with $\alpha \leq 0.33$. Moreover, differently from Pattanayak work [69], we did not observer any 'early time $t^{1/3}$' growth. These results are rather surprising, and we cannot exclude that are merely due to finite-size or finite-time effects. Indeed, we actually know that the scaling problem can be delicate, and therefore requires to be extra careful. This was for example shown in [73] for Model H, which takes hydrodynamics into account. There, it emerges clearly that one should be very careful in order to obtain the right exponents as the scaling regime

for long times may need very long simulations and large systems.

Further investigation of these surprising results is an interesting future direction.

2.6 Conclusions

In this chapter, we performed an in-depth analysis of the statistical properties of the bubbly liquid and of the bubbly phase separation in AMB+. These results were achieved by means of our efficient parallel pseudo-spectral code, that allowed us to simulate larger systems for longer times with respect to previous studies [60]. One of the major results was to prove that the bubbly phase separation is, at least for the parameters chosen and as was conjectured in [60], a bulk phase separation between the bubbly liquid at global density ϕ_{BL} and the uniform vapor phase at density ϕ_V.

Remarkably, and thanks to a significant computational effort, we were able to obtain results that are converged both in time and system-size, and in both the microphase separated regime and the bubbly phase separation one. It was rather surprising to discover that the convergence, both in time and system size, is significantly longer when the system is heading towards bubbly phase separation than when it is heading towards a microphase separated state. In particular, it was unexpected that the typical time for convergence increases with system-size when converging towards a bubbly phase-separated state even once that system-size convergence is achieved. At this stage we have no analytical understanding of this fact.

Some points remain unsolved and probably calls for analytical understanding. In particular, our limited knowledge of nucleation processes in AMB+, did not allow us to fully understand the infinite time and space limit of the transition between the microphase separated state and the homogeneous liquid. This is so because we do not have any estimation of the minimal vapor bubble that the system can support (the analogous of the nucleation radius in equilibrium fluids).

Another open point that we could not fully resolve is whether activity changes the standard $t^{1/3}$ coarsening law that is well known for Model B [6]. Indeed, measuring the scaling of the typical length scale when heading towards phase separation, we did not find $t^{1/3}$ except for Model B parameters, see Sec. 2.5. This is surprising, it is currently unclear whether is just an artifact of the finite time and size of our simulations.

Chapter 3

Capillary interfacial tension in active phase separation: Fluctuations of the liquid-vapor interface and active foam state

As we saw in Sec. 1.4.1, in passive systems the interfacial tension is a well-defined quantity and is responsible for the Ostwald ripening process and the Laplace pressure jump. Moreover, it also determines the elastic properties of the interface by setting the spectrum of capillary waves (that by definition are waves traveling along the phase boundary of a fluid) [74].

In active systems a proper definition of the interfacial liquid-vapor interfacial tension has been debated on the basis of numerical and analytical studies [75, 68, 76, 77, 78, 79, 80]. In this chapter, we will show that a unique definition of interfacial tension does not exist. Indeed, we are able for the first time to determine analytically σ_{cw}, the capillary wave interfacial tension that sets the fluctuation properties of the interface and the spectrum of the capillary waves. We will also show that σ_{cw} differs from σ, the tension introduced in Sec. 1.6 determining the Laplace pressure, and the Ostwald ripening rate. Our results are based on the study of AMB+, which allowed for significant analytical progress. Extending them to other active systems, such as particle models is a very interesting future direction.

In passive systems undergoing phase-separation, the definition of the capillary tension σ_{cw} emerges naturally by deriving an effective equation that describes the evolution to a height perturbation to the interface. This was for example shown in the framework of Model B in [81]. We generalise this work to AMB+, obtaining the effective evolution of the interfacial height of the liquid-vapor interface explicitly, and compare theoretical predictions with direct numerical simulations of AMB+. This shows that we are able to capture perfectly both the decay rate of interfacial

fluctuations and the spectrum of capillary waves.

Surprisingly, we further discover that $\sigma_{\rm cw}$ can get negative in a region of the AMB+ phase diagram. In this case, the liquid-vapor interface is unstable against height fluctuations with a mechanism similar to the one described by Mullins and Sekerka in solidification [82]. In this regime, depending on the global composition, the system self-organizes, either into a microphase-separated state in which coalescence is highly inhibited, or into an 'active foam' state. These represent new types of active phase separation that were previously unknown; we characterize numerically their statistical properties.

The results contained in this Chapter were published in *Physical Review Letters* [3].

The Chapter is organized as follows. In Sec. 3.1, we derive the effective equation for the interface. Our main result is (3.2); a reader not interested in the technical details can skip the rest of this section. In Sec. 3.2 we derive the phase diagram at mean-field level in terms of AMB+ in terms of σ and σ_{cw}. In Sec. 3.1 we derive and verify by direct numerical simulations capillary wave theory. Finally, in Sec. 3.4, we describe the instability of the interface when $\sigma_{cw} < 0$, explain why the system remains phase separated, and the novel active phases we obtain in this regime: a new micro-phase separated state and active foams.

3.1 Effective equation for the interface

Let us assume the system is in phase separated with an interface that, on average, is flat. Due to noise, though, this interface fluctuates in time. To describe these fluctuations, we look for an effective equation describing the vertical displacement from the rest position of the interface. Our analysis closely follow a technique introduced in [6] for passive systems undergoing phase separation, and is valid for small amplitude, long-wavelength perturbations of the interfacial height.

We first assume the absence of overhangs in the interface, so that is possible to define a proper function $\hat{h}(\mathbf{x}, t)$, describing the interfacial height. The latter is defined on a $(d-1)$ plane, and has in-plane and vertical coordinates $(\mathbf{x}, y) = \mathbf{r}$. On a rapid time-scale, we expect diffusion to quasi-statically relax the value of $\phi(\mathbf{r}, t)$ to a value that depends only on the distance from the interface. Since the latter is equivalent to the vertical distance from the interface (for small amplitude and long-wavelength perturbations), we can make the following assumption (see also Fig. 3.1):

$$\phi(\mathbf{r}, t) = \varphi(y - \hat{h}(\mathbf{x}, t)), \tag{3.1}$$

where φ is the interfacial profile. Notice that, since the mass is conserved, the spatial average of $\hat{h}$ is constant. We choose the reference frame for which this average is zero.

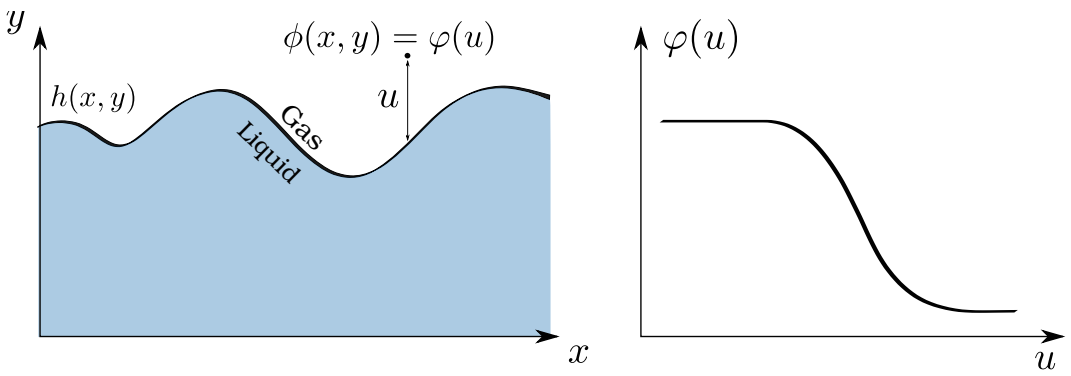

Figure 3.1: Graphical representation of the interface $h(x, y)$. Following the assumption made in the main text, we can write the field $\phi(x, y)$ in a point (x, y) as a function $\varphi(u)$ of the distance from the interface u. We represent the interface in $2D$ for simplicity.

For convenience we report here the result of our analysis, along with the definitions of the terms we will be using in the following. It turns out that $\hat{h}$ solves a non-local equation in space, so we work in terms of its Fourier transform $h(\mathbf{q}_x, t)$.

The effective equation for the interfacial height that we obtain is given by

$$\partial_t h = -\frac{2\sigma_{\rm cw}(q)q^3}{A(q)}h + \chi + \mathcal{O}(h^2) \tag{3.2}$$

where $q = |\mathbf{q}|$, $\nabla_{\mathbf{x}}$ is the gradient with respect to $\mathbf{x}$, $\mathcal{F}[\cdot] = \int d\mathbf{x}\, e^{-i\mathbf{q}\cdot\mathbf{x}}\,\cdot$ is the Fourier transform operator along the $\mathbf{x}$ direction, and

$$A(q) = \int dy_1 dy_2\, \psi'(y_1)\varphi'(y_2)\exp\left(-q|y_1 - y_2|\right)\,. \tag{3.3}$$

The capillary wave surface tension is given by

$$\begin{aligned}\sigma_{\rm cw}(q) &= \sigma_\lambda + \frac{3\zeta}{2}\int dy_1 dy_2\, \frac{(y_1 - y_2)}{|y_1 - y_2|}\frac{\psi'(y_1)\varphi'^2(y_2)}{e^{q|y_1 - y_2|}} \\ \sigma_\lambda &= K\int dy\, \varphi'(y)\psi'(y)\,.\end{aligned} \tag{3.4}$$

Finally, the noise χ is Gaussian and has correlations:

$$\langle \chi(\mathbf{q}_1, t_1)\chi(\mathbf{q}_2, t_2)\rangle = C_\chi(q_1)\delta(\mathbf{q}_1 + \mathbf{q}_2)\delta(t_1 - t_2) \tag{3.5}$$

where

$$C_\chi(q) = 4(2\pi)^{d-1}\frac{DB(q)}{A^2(q)}q + \mathcal{O}(h^2) \tag{3.6}$$

$$B(q) = \int dy_1 dy_2\, \psi'(y_1)\psi'(y_2)\exp(-q|y_1 - y_2|)\,. \tag{3.7}$$

In the next section, we show how such results are obtained. We will start from the mean-field case $D = 0$, adding the noise in a second step.

3.1.1 Mean-field approximation

Before proceeding, we introduce a useful operator, the inverse of the Laplacian ∇^{-2}. By definition, if we apply such operator on a function $\hat{s}$, the resulting $\nabla^{-2}\hat{s}(\mathbf{x}, y) = \hat{g}$ is such that $\nabla^2\hat{g} = \hat{s}$. It is easy to show that the Fourier transform of $\hat{g}$ along $\mathbf{x}$ is given by

$$g(\mathbf{q}, y) = -\frac{1}{2q}\int dy_1 e^{-q|y - y_1|}s(\mathbf{q}, y_1)\,. \tag{3.8}$$

this result will prove useful later on.

Setting $D = 0$ and applying ∇^{-2} to Eq. (3.1) into Eq. (1.30) we obtain:

$$\nabla^{-2}\partial_t\varphi = f'(\varphi) - K\nabla^2\varphi + \lambda|\nabla\varphi|^2 - \zeta\nabla^{-2}\nabla\cdot\left[(\nabla^2\varphi)\nabla\varphi\right] \tag{3.9}$$

1. Model B

Let us first consider the equilibrium case $\lambda = \zeta = 0$, hence generalizing the approach of [81] to arbitrary q-values. Applying the chain rule to (3.9) gives

$$-\nabla^{-2}\left[\varphi'\partial_t\hat{h}\right] = f'(\varphi) - K\varphi''(1+|\nabla_{\mathbf{x}}\hat{h}|^2) + K\varphi'\nabla^2_{\mathbf{x}}\hat{h}$$

To localize the equation around the interface, we multiply by φ' and integrate over $u = y - \hat{h}(\mathbf{x},t)$ across the interface:

$$-\int dy\ \varphi'(y-\hat{h}(\mathbf{x}))\nabla^{-2}\left[\varphi'\partial_t\hat{h}\right](\mathbf{x},y) = \Delta f + \sigma_{eq}\nabla^2_{\mathbf{x}}\hat{h} \tag{3.10}$$

where $\Delta f = f(\phi_2) - f(\phi_1)$ and σ_{eq} was defined in Eq. (1.24). The last equality was obtained by assuming that $\phi(y\to\infty) = \phi_2$ and $\phi(y\to-\infty) = \phi_1$, and that φ' vanishes in the bulk. Fourier transforming along the $\mathbf{x}$ direction and using (3.8) gives the deterministic part of the effective interface equation for Model B

$$\partial_t h = -\frac{2\sigma_{eq}q^3}{A_{eq}(q)}h + \mathcal{O}(h^2) \tag{3.11}$$

where

$$A_{eq}(q) = \int dy_1 dy_2\, \varphi'(y_1)\varphi'(y_2)\exp\left(-q|y_1-y_2|\right) \tag{3.12}$$

Observe that the term coming from Δf in (3.10) is proportional to q multiplied by the Dirac delta $q\delta(\mathbf{q})$, and thus vanishes.

2. AMB+

We now consider $\lambda, \zeta \neq 0$. From (3.9), the analog of (3.10) now reads

$$-\nabla^{-2}\left[\varphi'\partial_t\hat{h}\right] = \mu_\lambda + \mu_\zeta \tag{3.13}$$

where

$$\begin{aligned}
\mu_\lambda &= f'(\varphi) + (1+|\nabla_{\mathbf{x}}\hat{h}|^2)(\lambda\varphi'^2 - K\varphi'') + K\varphi'\nabla^2_{\mathbf{x}}\hat{h} \\
\mu_\zeta &= -\zeta\nabla^{-2}\Big\{\nabla_{\mathbf{x}}\cdot\Big[\left(\varphi''|\nabla_{\mathbf{x}}\hat{h}|^2 - \varphi'\nabla^2_{\mathbf{x}}\hat{h} + \varphi''\right) \\
&\quad \left(-\varphi'\nabla_{\mathbf{x}}\hat{h}\right)\Big] + \partial_y\left[\left(\varphi''|\nabla_{\mathbf{x}}\hat{h}|^2 - \varphi'\nabla^2_{\mathbf{x}}\hat{h} + \varphi''\right)\varphi'\right]\Big\}\,.
\end{aligned} \tag{3.14}$$

In order to progress we need to express AMB+ in term of the pseudo-variables ψ, g (solutions of Eq. (1.36), *cfr.* Sec. 1.6). We then multiply (3.13) by ψ', integrate across the interface and apply the Fourier transform along $\mathbf{x}$.

Left-hand side For the left-hand side of (3.13) we obtain:

$$\frac{A(q)}{2q}\partial_t h(\mathbf{q},t) + \mathcal{O}(h^2) \tag{3.15}$$

where $A(q)$ is defined in equation (3.3).

Right-hand side, μ_λ On the right-hand side of (3.13), the first term in μ_λ vanishes by straightforwardly applying the definition of g (Eq. (1.36)):

$$\delta(\mathbf{q})\int_{-\infty}^{\infty} du\,\psi'(u)f'(\varphi(u)) = g(\psi_2) - g(\psi_1) = 0$$

To evaluate the second term in μ_λ we exploit the definition of ψ in Eq. (1.36):

$$\int_{-\infty}^{\infty} du\,(\lambda\varphi'^2(u) - K\varphi''(u))\psi'(u) = \frac{\zeta}{2}\int_{-\infty}^{\infty} du\,\varphi'^2(u)\psi'(u) \tag{3.16}$$

The contribution in (3.16) will be canceled by an opposite one coming from μ_ζ. The third term in μ_λ gives:

$$-q^2\sigma_\lambda h(\mathbf{q},t) \tag{3.17}$$

where σ_λ was defined in equation (3.4).

Right-hand side, μ_ζ We now consider μ_ζ in (3.14). Expanding in powers of $\hat{h}$, we have

$$\begin{aligned}\nabla^2_{\mathbf{x}}\left(\tfrac{1}{\zeta}\mu_\zeta\right) &= -\tfrac{1}{2}\partial_y^2(\varphi'^2) + \tfrac{3}{2}\partial_y(\varphi'^2)\nabla^2_{\mathbf{x}}\hat{h} \\ -\varphi'^2\nabla_{\mathbf{x}}\cdot[\nabla^2_{\mathbf{x}}h\nabla_{\mathbf{x}}\hat{h}] &- \partial_y^2(\varphi'^2)|\nabla_{\mathbf{x}}\hat{h}|^2 + \mathcal{O}(\zeta q^3 h^3)\,.\end{aligned} \tag{3.18}$$

Then, we Fourier transform, invert the Laplacian using (3.8) and exploit

$$\partial_u e^{-q|y-u|} = q\ \mathrm{sgn}(y-u)e^{-q|y-u|} \tag{3.19}$$

where sgn is the sign function. Applying the same procedure as before and adding up the result with (3.15), (3.16), (3.17) we obtain the deterministic part of (3.2).

3.1.2 Finite noise effect

We now consider the noise effect. First of all, we choose to work in the Stratonovich convention. This is a natural choice, given that our Ansatz assumes that the density field relaxes very rapidly to fluctuations of h. Within Stratonovich convention the equality (we have used before)

$$\partial_t\phi = -\varphi'(y - \hat{h}(\mathbf{x}))\partial_t\hat{h}(\mathbf{x}) \tag{3.20}$$

is exact even when $D \neq 0$.

We are left with deriving the noise χ and show that its correlation is given by (3.6). We first consider

$$\xi(\mathbf{x}, y, t) = (\nabla^{-2}\eta)(\mathbf{x}, y, t) \tag{3.21}$$

where $\eta = -\nabla \cdot \sqrt{2D}\mathbf{\Lambda}$. The noise term ξ, being a linear transformation of η, is also a Gaussian noise. Its correlation reads

$$C_\xi(\mathbf{x}, y, t) = -2D\nabla^{-2}\delta(\mathbf{x})\delta(y)\delta(t) \tag{3.22}$$

and its Fourier transform along $\mathbf{x}$, using the inverse Laplacian expression in (3.8), is

$$C_\xi(q, y, t) = \frac{D}{q}e^{-q|y|}\delta(t) \tag{3.23}$$

The noise χ is given by

$$\chi(\mathbf{q}, t) = \frac{2q}{A(q)}\mathcal{F}\left[\int dy\, \psi'(y - \hat{h}(\mathbf{x}))\xi(\mathbf{x}, y, t)\right](\mathbf{q}, t)$$

which is also Gaussian. It is now a lengthly but straightforward calculation to show that the correlation of χ is given by (3.6). This concludes the derivation of the effective interface equation (3.2).

3.1.3 Capillary wave tension

For wavelengths much larger than the interfacial width $\xi \sim \xi_{eq} = (K/2a)^{1/2}$, we can replace $\sigma_{\rm cw}(q)$, $A(q)$ and $B(q)$ entering in the effective interface equation (3.2) with their limiting values as $q \to 0$. These, with a slight abuse of notation, are denoted as $\sigma_{\rm cw}$, A and B. Explicitly, the resulting capillary-wave tension $\sigma_{\rm cw}$ obeys

$$\sigma_{\rm cw} = \sigma_\lambda - \zeta \int dy \left[\psi(y) - \frac{\psi_1 + \psi_2}{2}\right]\varphi'^2(y) \tag{3.24}$$

where $\psi_{1,2} = \psi(\phi_{1,2})$ are the pseudo-densities at the binodals. As expected $\sigma_{\rm cw}$ reduces, in the equilibrium limit ($\lambda, \zeta \to 0$), to the standard interfacial tension $\sigma_{\rm eq} = K\int dy\, \varphi'^2(y)$ [83] which governs not only the capillary fluctuation spectrum, but also the Laplace pressure and the rate of Ostwald ripening [81, 6]. Switching on activity breaks this degeneracy. Indeed, the tension determining the rate of Ostwald ripening of a bubble was given in [60] as

$$\sigma = \sigma_\lambda - \zeta \int dy\, [\psi - \psi(0)]\, \varphi'^2(y) \tag{3.25}$$

where $\psi(0)$ is the value of the pseudo-density at the droplet center. Therefore σ is in general not equal to $\sigma_{\rm cw}$. However, σ_{cw} has a rather natural interpretation in terms of σ: it is the average tension between the one experienced by vapor bubbles and the one experienced by liquid droplets.

3.2 AMB+ phase diagram in terms of surface tensions

In order to obtain explicit predictions from (3.2), we need to evaluate $\sigma_{\rm cw}$, A and B. We now describe how to obtain them with a simple numerical procedure we implemented. This will allow us to draw the phase diagram of AMB+ in terms of σ_{cw}.

The crucial ingredient to compute $\sigma_{\rm cw}$, A and B is the interfacial shape $\varphi(y)$. At equilibrium, this is well-known [83]:

$$\varphi_{\rm eq}(y) = \pm \tanh(y/\xi_{\rm eq}) \tag{3.26}$$

with $\xi_{\rm eq} = \sqrt{2K/A}$ and $\sigma_{\rm eq} = \sqrt{8KA/9}$. We obtain, in this case, $A = B = 4$.

Another interesting limiting case, for which computations are easier, is $2\lambda = \zeta$. It is readily shown that, in this case, $\varphi = \varphi_{\rm eq}$ so that $\sigma_{\rm cw} = \sigma_{\rm eq}$, that are still different from the Ostwald tensions $\sigma = \sigma_{\rm eq}(1 \mp \zeta/K)$ for bubble growth $(-)$, and liquid droplet growth $(+)$, respectively [60].

For general values of λ, ζ we do not have closed-form results for $\sigma_{\rm cw}$; however, a change of variable to $w(\varphi) = \varphi'^2$ in the integrals defining $\sigma_{\rm cw}, A, B$ allows use of a simple numerical procedure, as first used in [51], to find the low q behavior. First, as shown in [60], the binodals are easily obtained numerically solving the coupled equations

$$\mu = f'(\phi_1) = f'(\phi_2) \tag{3.27}$$

$$\mu\psi_1 - g(\phi_1) = \mu\psi_2 - g(\phi_2). \tag{3.28}$$

It is then easy to show that w solves

$$Kw' = (2\lambda - \zeta)w = 2(f' - \mu) \tag{3.29}$$

which is solved by

$$w(x) = e^{-\frac{\zeta-2\lambda}{K}x}\left[c + \frac{2}{K}\int_1^x e^{\frac{\zeta-2\lambda}{K}y}(f'(x) - \mu)dy\right]. \tag{3.30}$$

The knowledge of $\phi_{1,2}$ allows to fix the integration constant c and the numerical evaluation of w via (3.30) is straightforward.

By studying the sign of the interfacial tensions $\sigma_{\rm cw}$ and σ, we can build the full phase diagram of AMB+ at a mean-field level (see Fig. 3.2). For small activity, or for $\lambda\zeta < 0$ both interfacial tension are positive. The system undergoes bulk phase separation, exactly like in equilibrium. For higher activity levels and $\lambda\zeta > 0$, we find an area of the phase diagram for which $\sigma_{\rm cw} > 0$ and $\sigma < 0$; here vapor bubbles undergoing reversed Ostwald ripening have stable interfaces and, depending on the global density, the system is either micro-phase separated or in bubbly phase separation [60]. In Chapter 2 we studied the statistical properties of these two phases in this area. At high activity, when $\lambda\zeta > 0$, a new regime emerges where $\sigma_{\rm cw} < 0$ and liquid-vapor interfaces (also the flat ones) become locally unstable.

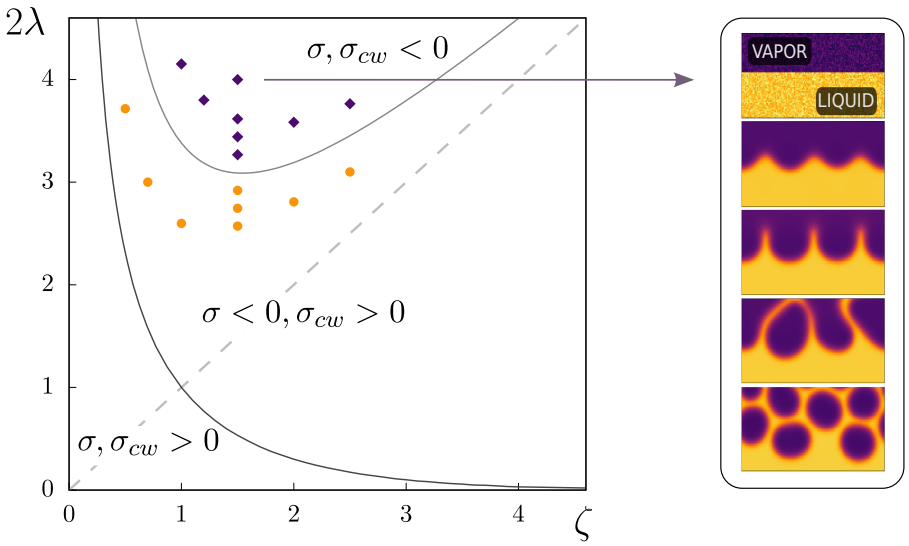

Figure 3.2: Mean-field phase diagram of AMB+ for $\zeta > 0$, showing sign regimes of interfacial tensions σ and $\sigma_{\rm cw}$. When $\sigma_{\rm cw} > 0$, the interface is stable, and unstable otherwise. Orange circles and blue squares respectively denote the results of direct simulations of AMB+ where the interface instability is or is not observed starting from a phase separated state with superposition of noise (see snapshots on the right). This shows the accuracy of our analytical prediction of the critical line $\sigma_{\rm cw} = 0$. Right: interfacial instability ($\zeta = 1.5, \lambda = 2$). To get the full phase diagram, we can exploit the symmetry $(\lambda, \zeta, \phi) \to -(\lambda, \zeta, \phi)$ and obtain the other two transition lines for $\lambda, \zeta < 0$. Notice that no transition line is present when $\lambda\zeta < 0$.

3.3 Capillary wave theory and decay rate of interfacial fluctuations in active phase separation

We first consider the regime where $\sigma_{\rm cw} > 0$. In the absence of noise, our theory predicts that capillary tension governs the relaxation of the interface, through

$$h(\mathbf{q}, t) = h(\mathbf{q}, 0) \exp(-t/\tau(q)) \tag{3.31}$$

where the typical time-scale $\tau(q)$ is defined by

$$\frac{1}{\tau(q)} = \frac{2\sigma_{\rm cw}(q) q^3}{A(q)} \tag{3.32}$$

In order to compute $\tau(q)$ at $q \neq 0$, we extracted the interface profile from simulations of AMB+ at $D = 0$. It is important to notice that such prediction holds for either sign of the Ostwald tension σ.

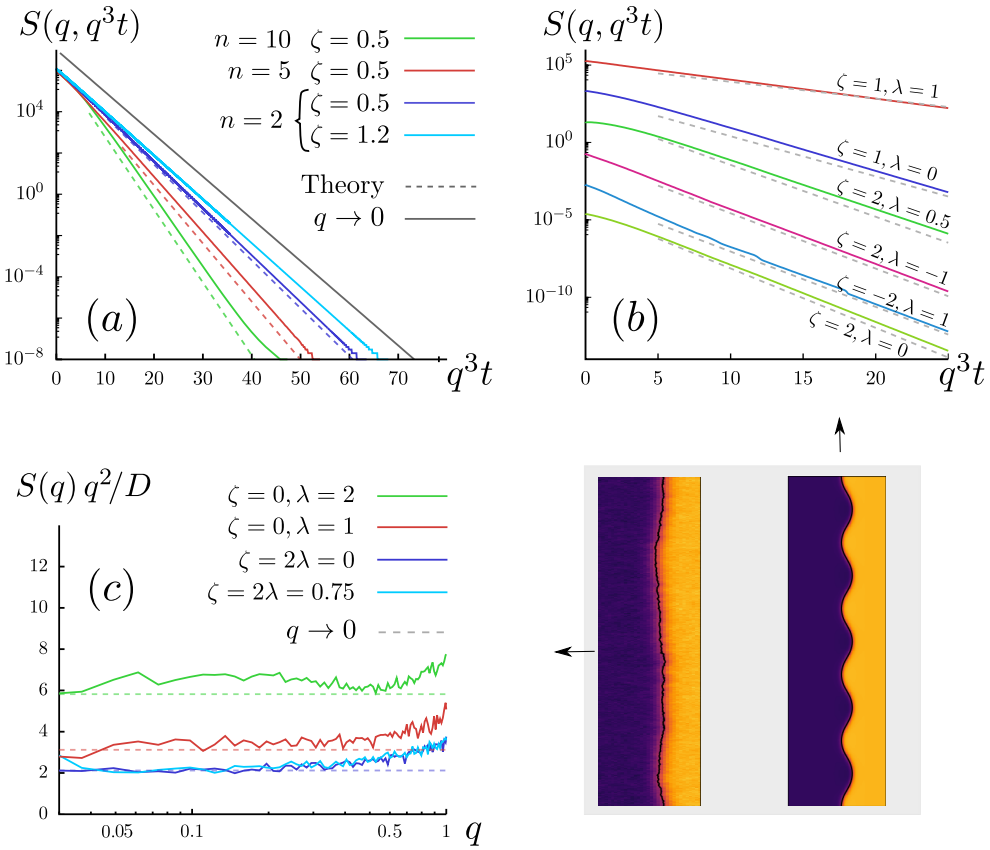

Figure 3.3: (a) Relaxation of $S(q,t)$ in the regime $\sigma_{\rm cw} > 0$ for a single mode $q = 2\pi n/L_x$ with $L_x = L_y = 256$ and noise $D = 0$. The initial condition, shown in the snapshot on the right, corresponds to a flat liquid-vapor interface excited by a sinusoidal perturbation corresponding to mode q. The dotted lines correspond to the theoretical predictions obtained using $\tau(q)$ (3.32). Simulations are done along the line $\zeta = 2\lambda$, therefore all the theoretical prediction converge to the same prediction for $q \to 0$ (continuous gray line).
(b) Relaxation of $S(q,t)$ for various $\zeta \neq \lambda$ and low wave-length ($q = 2\pi 4/L_x, L_x = L_y = 512$). Dotted lines represent the theoretical prediction for $q \to 0$.
(c) Scaled structure factor $q^2 S(q)/D$ vs q compared to the $q \to 0$ analytical prediction; results are averaged over 30 realizations of duration 10^6 after equilibration. A typical snapshot in steady state is shown on its right. Noise level is equal to $D = 5 \times 10^{-3}$.

To check this prediction, we performed simulations of AMB+ for $D = 0$ starting from a phase separated state with the interface perturbed via a single mode q, and

checked the relaxation of $S(q,t) = \langle |h(q,t)|^2 \rangle$ for such particular mode. Fig. 3.3 confirms Equation (3.31) perfectly for either sign of the Ostwald tension σ.

Our theory also predicts the stationary structure factor of the interface $S(q) = \lim_{t\to\infty} \langle |h(\mathbf{q},t)|^2 \rangle$:

$$S(q) = \frac{(2\pi)^{d-1} D}{\sigma_{\rm cw}(q) q^2} \frac{B(q)}{A(q)} \xrightarrow[q\xi^{-1}\ll 1]{} \frac{(2\pi)^{d-1} D_{\rm eff}}{\sigma_{\rm cw} q^2} \tag{3.33}$$

where $D_{\rm eff} = D(\psi_2 - \psi_1)/(\phi_2 - \phi_1)$ is an effective capillary temperature. This result generalizes the capillary wave theory. Its equilibrium analog, $S(q) \propto D/\sigma_{\rm eq} q^2$ [74], is often justified using equipartition arguments but, even in equilibrium, higher order gradient terms give sub-leading corrections at finite q [84, 85]. Hence the hallmark of activity is not the similar corrections entering in (3.33); instead activity impacts the interfacial fluctuations by renormalizing the temperature $D \to D_{\rm eff}$ and, separately, replacing $\sigma_{\rm eq}$ with $\sigma_{\rm cw}$. Even though (3.33) also neglects the additional nonlinearities omitted from (3.2), it is quite accurate at small D (Fig. 3.3). The use of capillary wave theory in phase-separated active systems was previously advocated heuristically [78, 68, 77] but until now, only qualitative estimates were provided for the coefficient $D_{\rm eff}/\sigma_{\rm cw}$ in (3.33).

3.4 Unstable interfaces

We now turn to study the region where $\sigma_{\rm cw} < 0$. Here, a drastically new non-equilibrium phenomenology arises. Although the vapor-liquid interface is unstable to height fluctuations, we will see that the system remains phase separated. Unlike in equilibrium, where de-mixing itself cannot be sustained at negative tension, the active interface does not undergo diffusive collapse but remains stable against normal perturbations. After describing the stability to normal perturbations, we describe the physical mechanism that drives the instability of the interface against height perturbations. Finally, we perform numerical simulations of AMB+ at $D \neq 0$, discuss the new phase separated steady states reached by the system when $\sigma_{cw} < 0$, and study their statistical properties numerically.

3.4.1 Stability against normal perturbations

We start from showing that, whatever the sign of σ and σ_{cw}, the liquid vapor interface is stable against normal perturbations of the flat interface φ at mean-field level ($D = 0$). For simplicity, we restrict to the case of one-dimensional interfaces which, due to mass conservation, take the form

$$\phi(x,y,t) = \varphi(y) + \partial_y \epsilon(y,t) \tag{3.34}$$

where φ is the profile of the interface perpendicular to it and, hence, it solves

$$\partial_y^2 \left[f''(\varphi) - K\partial_y^2\varphi + (\lambda - \zeta/2)\varphi'^2 \right] = 0\,. \tag{3.35}$$

Therefore, we have for ϵ

$$\partial_t \epsilon = \mathcal{L}\epsilon + \mathcal{O}(\epsilon^2) \tag{3.36}$$

where the linear operator $\mathcal{L}$ is

$$\mathcal{L} = \partial_y \left[f''(\varphi) - K\partial_y^2 + (2\lambda - \zeta)\varphi'\partial_y \right] \partial_y\,. \tag{3.37}$$

We are thus led to study the spectrum of $\mathcal{L}$. In equilibrium, this problem is tractable analytically because $\mathcal{L}$ is self-adjoint. It was found [86, 87] that the spectrum of $\mathcal{L}$ is continuous and touches 0 in an infinite system (it is in fact $(-\infty, 0)$), implying that the decay of ϵ in time is algebraic in an infinite system. From (3.37) we see that the same result applies for $2\lambda = \zeta$.

For generic λ and ζ, we studied numerically the spectrum of $\mathcal{L}$ for finite systems. By Fourier transforming along y, and for the choice of a double well local free energy f, we consider the kernel $\mathcal{L}(q_1, q_2)$ of $\mathcal{L}$ defined from the relation $(\mathcal{L}\epsilon)(q_1) = \int dq_2 \mathcal{L}(q_1, q_2)\epsilon(q_2)$ for any test function ϵ. Explicitly:

$$\begin{aligned} \mathcal{L}(q_1, q_2) &= (-Kq_1^4 + Aq^2)\delta(q_1 - q_2) \\ &- 3Aq_1q_2\mathcal{F}_y[\varphi^2](q_1 - q_2) \\ &+ (2\lambda - \zeta)q_1q_2^2(q_1 - q_2)\mathcal{F}_y[\varphi](q_1 - q_2) \end{aligned} \tag{3.38}$$

where $\mathcal{F}_y[\cdot]$ denotes the Fourier transform operator along y. We discretised $\mathcal{L}(q_1, q_2)$ on a grid with discretization step $\Delta x = 1$ and total length L_y, so that $q_i = 2\pi n_i/L_y$, $n_i = 1, ..., N$, $N\Delta x = L_y$. We then computed numerically the eigenvalues α_i of $\mathcal{L}$ for several values of λ, ζ. Some of our results are reported in Fig. 3.4, showing that the qualitative picture is the same as at equilibrium: the spectrum of $\mathcal{L}$ is expected to be continuous and to touch 0 for an infinite system.

It should be observed that these conclusions apply irrespectively of the sign of both σ and σ_{cw}: in both cases, φ is stable against normal perturbations. This is crucial in order to sustain phase separation even when $\sigma_{cw} < 0$, as we shall see below it happens.

3.4.2 Instability against height perturbations

Next, we numerically simulated AMB+ at $D = 0$, with a noisy initial condition. Orange and blue dots in Fig. 3.2 respectively represent cases where the interfacial fluctuation is damped or amplified (Movie 1 of [3]), showing the accuracy of our analytical predictions.

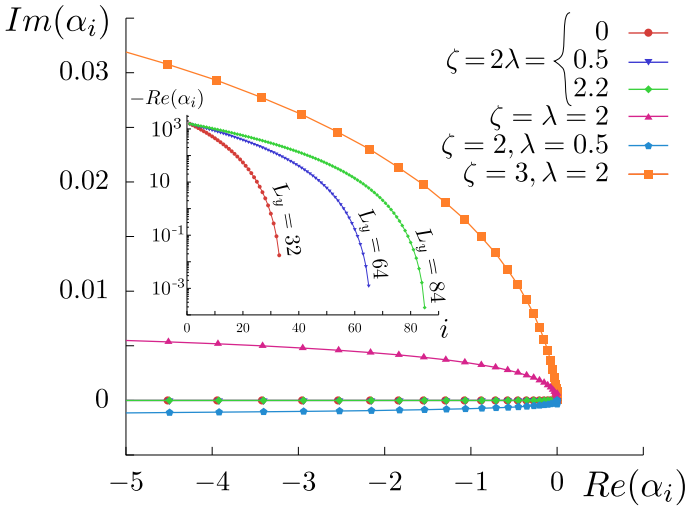

Figure 3.4: Eigenvalues α_i of $\mathcal{L}(q_1, q_2)$ for a system of linear size $L_y = 128$ in the vicinity of $Re(\alpha_i) = 0$ (the minimal eigenvalues for this system size have real part of order -10^3), spatial discretization $\Delta x = 1$ and values of the parameters as in the legend. The solid lines are our estimate of the continuous spectrum of $\mathcal{L}(q_1, q_2)$ in the infinite system-size limit, obtained from a fit of the discrete spectrum. Although the spectrum is modified with respect to the equilibrium case, its crucial properties are not: all eigenvalues are negative and touch 0 in the infinite system-size limit implying that the vapor-liquid interface is stable to normal perturbations but disturbances will only decay algebraically in time. Inset: $-Re(\alpha_i)$ for $\zeta = 2, \lambda = 0.5$ as a function of i for three system sizes, showing that the eigenvalue with the largest real part approaches zero.

The mechanism for the interfacial instability (Fig. 3.5) is reminiscent of the Mullins-Sekerka instability driving pattern formation in solidification [82]. In both cases the instability is driven by a single diffusing field: latent heat in crystal growth, and density in the present situation. Such a diffusing field settles to quasi-stationary values on the two sides of the interface which depend on the local curvature, with extrema denoted by $\phi_{\pm}^{B,D}$ in Fig. 3.5.

By approximating $\phi_{\pm}^{B,D}$ as the densities near the interface of a vapor bubble (B) or liquid droplet (D), we find that the diffusive current on the vapor side is always stabilizing. In contrast, depending on whether Ostwald ripening is normal or reversed, the current on the liquid side is stabilizing or destabilizing. If both currents are stabilizing, of course, the interface is stable. If not, the strongest current will determine the interfacial behavior. When the current on the liquid side is destabilising and stronger than the current on the vapor side, the interface is unstable. This condition is met when $\sigma_{\rm cw} < 0$ and fluctuations grow.

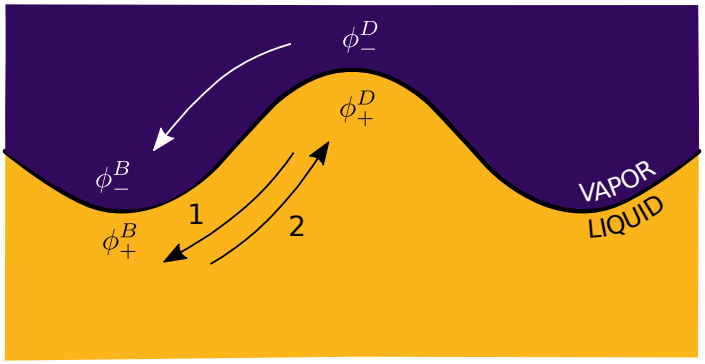

Figure 3.5: Mechanism of the interfacial instability when $\sigma_{\rm cw} < 0$. The densities on the two sides of the interface adjust quasi-statically at values that depend on its local curvature, leading to diffusive density fluxes. That on the vapor side is always stabilising (white arrow); that in the liquid is stabilising when $\sigma > 0$ (arrow 1) and becomes destabilising when $\sigma < 0$ (arrow 2). This (one-sided) reverse-Ostwald current does not trigger an instablity unless the current in the liquid outweighs that in the vapor, which requires $\sigma_{\rm cw} < 0$.

In Fig. 3.6 we support this mechanistic picture, plotting the quasi-static current close to the perturbed interface. We consider three sets of parameter values corresponding to normal Ostwald ripening ($\sigma > 0$), reversed Ostwald ripening but stable interface ($\sigma < 0$, $\sigma_{cw} > 0$), and unstable interface ($\sigma < 0, \sigma_{cw} < 0$). The current on the vapor side is always stabilizing while it is stabilizing in the liquid side only if $\sigma > 0$. However, $\sigma < 0$ is not sufficient to drive the instability. For this, the destabilizing current on the liquid side needs to be stronger than the one on the vapor side. This happens only in the rightmost case of Fig. 3.6, which corresponds to $\sigma_{cw} < 0$. To show this, we have measured the average current $\bar{J}_L$ in the liquid projected along $e_{\mathbf{x}} = \mathbf{x}/|\mathbf{x}|$ defined as

$$\bar{J}_L^2 = \int dx \int_{\{y|\phi(\mathbf{x},y,t)>\phi_{th}\}} dy (\mathbf{J}\cdot e_{\mathbf{x}})^2 \tag{3.39}$$

and the analogous quantity in the vapor $\bar{J}_V$.

The instability of the flat interface is critical at the onset of the instability: when crossing the critical λ value, the most unstable mode is the smallest available one ($q = 0$ in an infinite system). To show this we exploited the analytical expression of the damping rate of equation (3.32). In particular, we extracted from simulations at $D = 0$ and system-size $L_x = L_y = 256$ the interfacial profile $\varphi(y)$ and then used it to evaluate $\tau(q)$ at arbitrarily low q. The results for $\zeta = 1$ and varying λ are reported in Fig. 3.7.

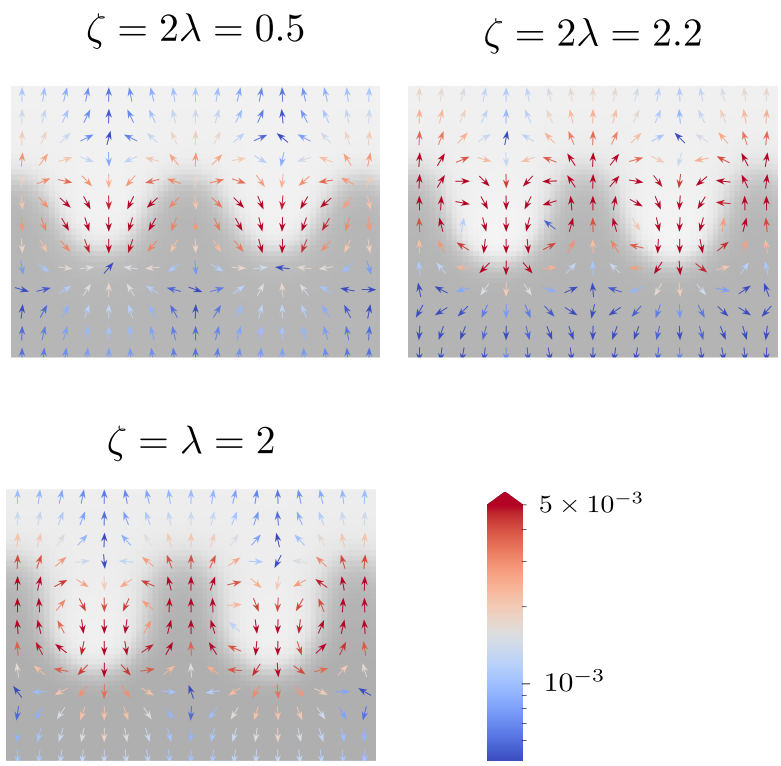

Figure 3.6: Current **J** close to (left) the stable interface and normal Ostwald ripening ($\zeta = 2\lambda = 0.5$), (middle) stable interface and reversed Ostwald ripening for bubbles ($\zeta = 2\lambda = 2.2$) and (right) unstable interface ($\zeta = \lambda = 2$). Simulations are at mean-field ($D = 0$). The liquid is shown in dark gray and the magnitude of the current in colors. Only a small part of the system is shown. We measured $\bar{J}_V - \bar{J}_L = 0.04$ for $2\lambda = \zeta = 0.5$, $\bar{J}_V - \bar{J}_L = 0.08$ for $2\lambda = \zeta = 2.2$ and $\bar{J}_V - \bar{J}_L = -0.02$ for $2\lambda = \zeta = 2$. This confirms that the instability arises only when the current on the liquid side overwhelms the one on the vapor side.

3.4.3 New active phases

To study the effects of the interface stability on the phenomenology of AMB+, we performed simulations with a small but finite noise level (to ensure reproducible steady states). Starting from a near-uniform initial state, we find that the final phase separation is strongly affected by the interfacial instability. The stable case, $\sigma_{\rm cw} > 0$, was explored in [60]. For the unstable case, $\sigma_{\rm cw} < 0$, the stationary states seen by varying the global density $\phi_0 = \int \phi d\mathbf{r}/V$ are reported in Fig. 3.8 and Movie 2 of [3].

When ϕ_0 lies outside the mean-field binodals $\phi_{1,2}$, the system remains homo-

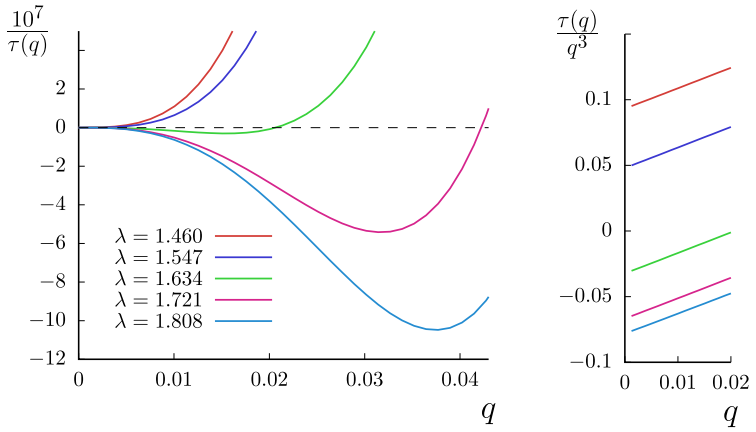

Figure 3.7: (Left) Damping rate $1/\tau(q)$ vs q at $\zeta = 1.5$ crossing the stability line, located at $\lambda \simeq 1.6$. The most unstable mode (the minimum of $1/\tau(q)$) goes to $q = 0$ as one approaches the critical λ. (Right) Plot of $\tau(q)/q^3$, showing that the change of sign of the damping rate happens at the estimated critical value of λ.

geneous. Within them, at large ϕ_0 such that the liquid is the majority phase, we find a microphase-separated state where coalescence of crowded bubbles is highly inhibited. The bubble size distribution $P(A)$ is strongly peaked, the more peaked the lower the noise, suggesting that the average bubble size $\langle A \rangle$ is finite when $D \to 0$. Our results are converged in time for $D > 0.1$; at lower noise the system gets trapped into metastable states, evolving only due to rare fluctuations of the bubbles interface.

In Fig. 3.10 we plot the evolution, starting from an homogeneous state or a fully phase separated state, of the average size of bubbles and their number while converging to the microphase separated state. As shown, the convergence slows down when decreasing the noise value. This is because the initially formed bubbles are stable to small perturbations of their interface and evolution to the steady state is possible only by rare events at low noise.

Understanding analytically the stability of circular bubbles would be key to compute $\langle A \rangle$ and $P(A)$. Clearly, though, the average size is not set by the most unstable mode of the flat interface, as the steady state is attained by a series of secondary instabilities (Movie 1 and 3 of [3]). This phenomenology is at odds with the bubble phase at $\sigma_{\rm cw} > 0$ [60], where a balance between nucleation, coalescence and reversed Ostwald causes $\langle A \rangle \to \infty$ when $D \to 0$. The difference between these two microphase separated states is also apparent in the dynamical evolution starting from bulk phase separation (Movie 3 of [3]). When $\sigma_{\rm cw} < 0$ bubbles enters the liquid by buckling of the interface, rather than by nucleation, as in the $\sigma_{\rm cw} > 0$ case.

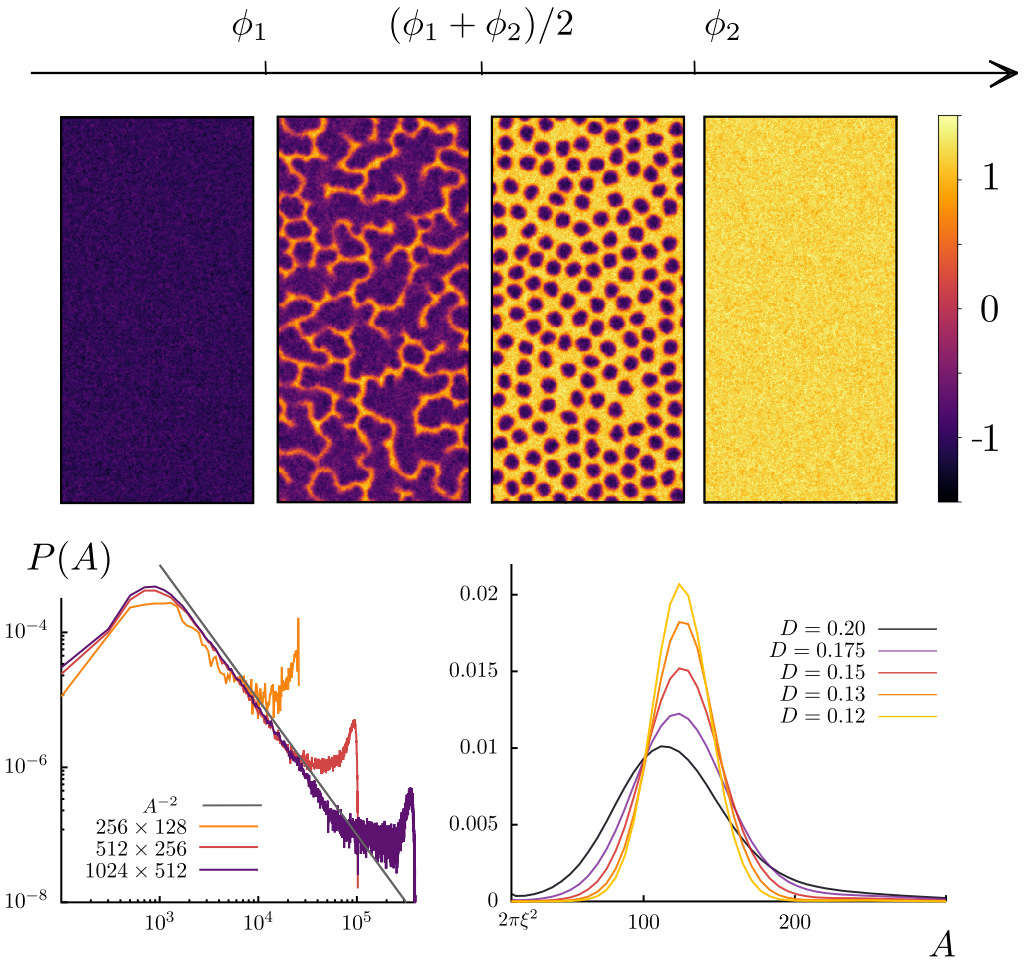

Figure 3.8: (Top) phase diagram when $\sigma_{\rm cw} < 0$ as a function of the global density $\phi_0 = -1, -0.4, 0.4, 1.2$ at $D = 0.05, L_x = 256, L_y = 512$ and $\lambda = 1.75, \zeta = 2$, for which $\phi_1 = -0.9, \phi_2 = 1.08$. At high and low ϕ_0, the system is homogeneous (liquid or vapor states). Within the binodals, when the liquid is the majority phase, the system shows microphase-separated vapor bubbles whose coalescence is highly inhibited. At lower ϕ_0, the system forms a continuously evolving active foam state. (Bottom): area distribution of vapor regions for the active foam state ($\phi_0 = -0.4$) and in the microphase-separated state for the noise values in the legend ($\phi_0 = 0.2$).

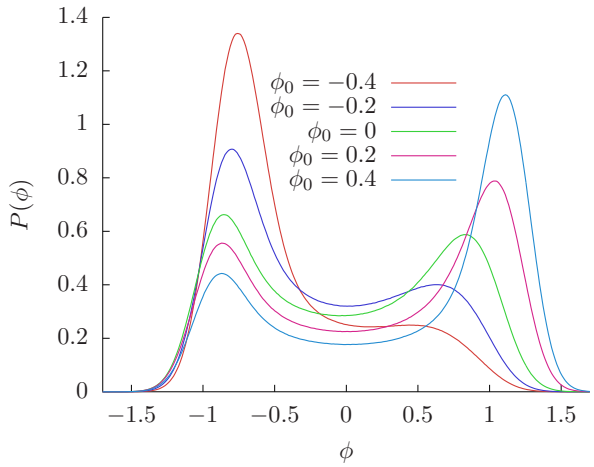

Figure 3.9: PDF of the density for $\zeta = 2$, $\lambda = 1.75$, $D = 0.05$ in a system 128×256 and several global densities ϕ_0 reported in the legend.

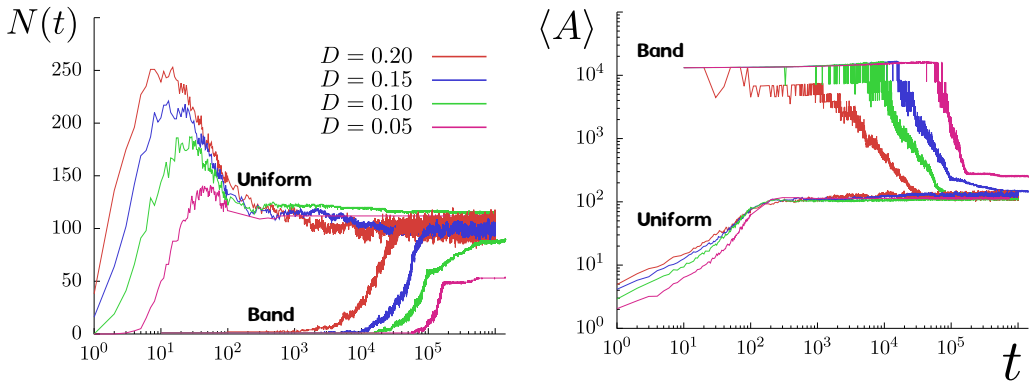

Figure 3.10: Evolution in time of the average bubble size $\langle A \rangle$ and of their number $N(t)$ for $\zeta = 2, \lambda = 1.75$ and various noise values starting either from an uniform or from a band (a fully phase separated state with a flat interface).

When the liquid is the minority phase, bubbles cannot avoid touching and coalescing. One might expect that the system attains a micro-phase separated state of liquid droplets (for $\zeta > 0$); this is not the case because, as is clear from our mechanistic argument above, the interfaces bends toward the vapor side. Instead, we find a previously unknown form of phase separation, which we call the 'active foam' state. Thin filaments of liquid are dispersed in the vapor phase, and continuously break and reconnect. These filaments are bent on the most unstable length-scale of the flat interface, as if there were an underlying 'virtual packing' of polyhedral

bubbles separated by thin films – but with many of these films absent. The area distribution of the vapor regions (Fig. 3.8b) is now peaked at at size that corresponds to the merging of two bubbles, but a power-law tail A^{-2} emerges, only cut off by the system-size. Note that the boundaries in ϕ_0 between the different phases of Fig. 3.8 are qualitative: while the vapor density is almost independent of ϕ_0 the liquid density varies markedly. In Fig. 3.9, we report the PDF of the density as a function of the global density ϕ_0. The vapor density is found, to a good accuracy, independent of ϕ_0. Instead, the liquid density varies rather significantly with ϕ_0. This is expected because of two reasons: the liquid density with which a finite size vapor bubble is in equilibrium differs from the binodal [60] and the presence of multiple droplets further change such value. Obtaining the dependence of the liquid density on ϕ_0 is an open problem.

3.5 Conclusions

A proper definition of the interfacial liquid-vapor interfacial tension in active systems has been debated for long time [75, 68, 76, 77, 78, 79, 80]. We have shown that a unique definition does not exist and, for the first time, we determined analytically σ_{cw}, the capillary wave interfacial tension that set the fluctuation properties of the interface (capillary waves). Our results show that σ_{cw} differ from the tension determining the Laplace pressure or the Ostwald ripening rate. Our analytical results agree perfectly with simulations on AMB+.

The techniques introduced here could be used to elucidate the capillary tension in particle-based active models, by applying them to various field-theoretical descriptions obtained by explicit coarse-graining [60, 52, 88], or to describe confluent biological tissues, where the measured interfacial tension was recently shown to be dependent on the measuring protocol [89].

Finally, although the reversal of the "Ostwald tension" σ was previously understood [60], it is remarkable that (a) the capillary tension can likewise become negative, and that (b) this leads to new types of phase separation including active foam states. Our approach is based on AMB+, whose generic, leading-order form is agnostic as to the microscopic mechanisms underlying activity (and even phase separation). This means that the microscopic ingredients needed for our new phases remain to be identified. For the exact same reason, we expect them to be widely present, not only in motility-induced phase separation [48], but in other phase-separating systems with locally broken detailed balance, such as in biological tissues [89].

Chapter 4

Minimal model for micro and bubbly phase separation

In passive fluids Ostwald ripening is the main dynamical mechanism leading to full phase separation. In active systems detailed balance is broken, and Ostwald ripening can go into reverse (Sec. 1.6). This leads to a rich phenomenology: micro-phase separation at low densities and bubbly phase separation at higher ones. In Chapter 2, we studied the statistics of both these phases when system convergence is attained within AMB+.

In models of self-propelled particles, bubbly phase separation was observed already a decade ago in simulations of active brownian particles interacting by pairwise repulsion [59], and more recent works confirmed it [2, 78]. Instead, the micro-phase separated state formed of vapor bubbles was never observed in particle models until very recently [1, 2] where they were found at densities below, but close, to the liquid binodal.

Studying the statistical properties of bubbly phase separation and micro-phase separation in particle models, however, has proven rather difficult. In [1], we have shown computationally in two particle models that bubbles have a very strong variability in size, and asymptotic results both in time and system size can be practically obtained only very close to the liquid binodal. Indeed, the PDF of bubble sizes was found to be power-law for intermediate sizes of the bubbles, complicating the statistical analysis. Attaining convergence within the bubbly phase-separated regime has proven practically impossible so far.

Within bubbly phase separation, the macroscopic bubble shrinks by reversed Ostwald ripening but grows by coalescence with smaller bubbles. While it is easy to tune the rate of Ostwald ripening in AMB+ (because this is directly given the surface tensions σ, that we related explicitly to AMB+ parameters), it is less clear how to tune the diffusivity of bubbles in terms of AMB+ parameters, and hence their coalescence rate.

In order to study the relative effect of reversed Ostwald ripening and coalescence, we introduce and study in this Chapter a minimal model where the degrees of freedom are the vapor bubbles themselves (effective bubbles model). These diffuse in space with diffusivity D, coalesce upon touching, and undergo reversed Ostwald process with rate β. Differently from a similar model that we introduced in [1], the present one takes care of the Ostwald process and of coalescence realistically. The advantage of the effective bubbles model studied in this Chapter over AMB+ and particle models is that we can independently tune the rate β of the Ostwald process versus the diffusivity D of bubbles which, in turns, determines the coalescence rate.

Importantly, we show that the non-dimensional ratio D/β sets the strength of finite-size effects and can change the density of the bubbly liquid when the system is globally is bubbly phase-separated.

When D/β is small or large (with respect to unity), we obtain results that are converged in system-size. At $D/\beta \ll 1$ we find micro-phase separation when the liquid is the majority phase and bubbly phase separation when it is the minority phase.

Upon increasing D/β, bubbly phase separation is favored: at fixed system size, it is observed at higher densities. This suggests that this is the regime in which the particle models as those studied in [59, 1] are. However, the bubble size distribution broadens and finite-size effects increase so that obtaining convergence in system size requires larger systems: we could obtain converged results up to $D/\beta = 0.5$ and for $D/\beta > 10$. We further show that, at high diffusivity, the density ϕ_{BL} marking the transition between micro-phase separation and bubbly phase separation increases, and probably it converges to the liquid binodal in the limit of $D/\beta \to \infty$.

For intermediate values of $0.5 < D/\beta < 10$ finite-size effects are stronger, and we could not reach system-size convergence so far. It seems unlikely, however, that different physics is at play. This point will be investigated in details in the near future by means of a more efficient code.

The chapter is organized as follows: in Sec. 4.1, we present the model and its parameters. Then, in Sec. 4.2, we study the D/β phase diagram, as well as the statistical properties of the bubbly phase and bubbly phase separation. Finally, in Sec. 4.2, we extend these results for D/β and discuss the differences. The technical details concerning the algorithm we used are in Appendix C.1.

4.1 Minimal model

As we saw in Chapter 2, the interplay between Ostwald ripening, bubble diffusion and nucleation determines the statistical properties of bubbly phase separation and bubbly liquid. By tuning the noise and activity parameters λ and ζ of AMB+ equations (1.30), we are, in practice, tuning the competition between reverse Ostwald ripening and the bubble coalescence. It is essentially this competition that determines the kind of phase-separation we have for a specific set of parameters. In the following, we devise a minimal model where we can control independently Ostwald ripening, nucleation and coalescence rate. We will see that this allows to show that the crucial ingredient determining the statistical properties of micro- and bubbly phase separation is the ratio between the rate of the Ostwald process and the diffusivity of vapor bubbles. This is instead difficult to study within AMB+ because one has no direct access to changing these rates independently (for example, changing λ, ζ in AMB+ does change the Ostwald ripening, but the effect on nucleation or coalescence is not under control).

Our minimal model describes the evolution in time of $N(t)$ bubbles diffusing in a two-dimensional system of size $V = L \times L$ with periodic boundary condition. Bubbles are spherical objects identified by their position and radius $(\boldsymbol{x}_i, R_i) \in (V, \mathbb{R}^+)$ and interact with each other directly, by coalescing upon contact, and indirectly, though reverse Ostwald ripening. The total number of bubbles decrease through coalescence and increases though nucleation of bubbles of radius R_0. Crucially, the total volume of vapor $V_G = \sum_i^{N(t)} \pi R_i^2(t)$ is conserved, as we will see more in details after the model definition.

Given the list of positions and radius of all $N(t)$ bubbles in the system, the time evolution from time t to $t + \Delta t$ is achieved through the following steps:

1. **Diffusion**: bubbles diffuse freely in space through the following dynamics:

$$\dot{\mathbf{x}}_i = \sqrt{\frac{2D}{R_i}}\eta_i \tag{4.1}$$

   where η_i are Gaussian noise with zero mean, unitary variance, and correlations given by $\langle \eta_i(t)\eta_j(s)\rangle = \delta_{ij}\delta(t-s)$. D is a diffusivity constant per unit length ($[D] = m^3/s$). For brevity, we will refer to it as diffusivity constant. It is indeed very natural that a vapor bubble diffuses accordingly to (4.1), at least when R is large enough, as this is the case for liquid droplets in a binary liquid ([71]). It would be however interesting to obtain a first principle derivation of Eq. (4.1).

2. **Reversed Ostwald process**: Each bubble i interacts with its first nearest neighbor (that we will indicate with the symbol ∂_i). For each bubble i and its nearest

neighbor ∂i, the radius evolves through the Ostwald ripening dynamics (that was derived in Eq. (1.56)):

$$\dot{R}_i = \frac{\beta}{R_i}\left[\frac{1}{R_i} - \frac{1}{R_{\partial_i}}\right] \tag{4.2}$$

$$\dot{R}_{\partial_i} = \frac{\beta}{R_{\partial_i}}\left[\frac{1}{R_{\partial_i}} - \frac{1}{R_i}\right] \tag{4.3}$$

where $\beta > 0$ is a free parameter of the model determining the Ostwald ripening rate, and is measured in $[D] = m^3/s$. It is important to notice that Eq. (4.2)-(4.3) conserve the total vapor volume of each pair of bubbles. Indeed, if we compute the volume variation in the pair we obtain:

$$\dot{A}_i + \dot{A}_{\partial_i} = 2\pi\left[R_i\dot{R}_i + R_{\partial_i}\dot{R}_{\partial_i}\right] = 0 \tag{4.4}$$

where we used 4.2 and 4.3 in the last passage.

3. **Coalescence**: Bubbles that are in contact with each other coalesce (i.e. merge into one larger bubble). In particular, let's consider the graph having bubbles as nodes, and links (i, j) between them for each pair of bubbles i, j in contact (i.e. whose distance $d(i, j)$ is smaller than $R_i + R_j$). Connected components on this graph are cluster of bubbles in contact, and can be found by running a deep first search on the whole graph. We merge each cluster by creating a new bubble positioned in the center of mass of the cluster. The volume of the resulting bubble is equal to the one of the biggest bubble plus a portion α_C of the volume of the others. In equations:

$$\sum_{j=1}^{N}(\mathbf{x}_j, R_j) \to \left(\frac{\sum_{j=1}^{n} R_j^2\mathbf{x}_j}{\sum_{j=1}^{n} R_j^2}, \sqrt{R_i^2 + \alpha_C\sum_{j\neq i}^{n-1} R_j^2}\right) \tag{4.5}$$

where $0 < \alpha_C < 1$ is a parameter of the model, n is the total number of bubbles in the cluster, and i is the largest bubble. Notice that i is singled out in order for the total volume to be certainly larger than the volume of the largest bubble.

4. **Nucleation** In step (c), each coalescence event lowers the amount of gas volume by:

$$\frac{(1-\alpha_C)\sum_{j\neq i} R_j^2}{R_0^2} \tag{4.6}$$

where i is the largest bubble that took part in the nucleation. To compensate the vapor loss, we nucleate N_{loss} bubbles of radius R_0, in such a way that $N_{loss}\pi R_0^2$ equates to the total vapor lost in the coalescence (up to fluctuations

of order ϕR_0^2 due to the discretization of N_{loss}). The positions of nucleated bubbles are chosen at random, one at a time, until a position in which they do not overlap with other bubbles is found.

As observed above, Ostwald ripening conserves the volume. At the same time, the volume lost by coalescence is reintroduced through nucleation. Therefore, in this model the total vapor volume is conserved (up to the fluctuations caused by the fact that N_{loss} is an integer). We have:

$$\sum_i \pi R_i^2 = const = V_G \tag{4.7}$$

The same is true for the vapor and liquid fractions in the system, $v_g = V_G/V$ and $v_l = 1 - v_g$, respectively; we will describe the system through these parameters (that enter the equations through initial conditions). In this sense, v_g (or v_l) has the same role that the global density has in AMB+ and particles models. The two choices are equivalent when considering constant vapor and liquid density ϕ_L and ϕ_V. Indeed, there exist a bijective relationship between the volume fraction $v_g = V_g/V$ and the global density ϕ_0:

$$\phi_0 = \phi_L + v_g(\phi_V - \phi_L)\,. \tag{4.8}$$

4.1.1 Discussion on the assumptions of the minimal bubble model

Let us comment on the assumptions made to define the minimal model defined above. First, both in AMB+ and particle models, bubbles are not necessarily spherical, having possibly more convoluted shapes according to some parameters choice. Here, we disregard this aspect.

Second, we assumed bubbles to diffuse accordingly to (4.1). As already mentioned, this mimics what is known for liquid droplets in a binary liquid ([71]).

Third, we consider vapor and liquid densities that are constant, which is not exactly true. The main reasons are the corrections of order $1/R$ to the vapor density for bubble of radius R; and the fact that, both in continuum and particle models, these quantity are fluctuating.

Fourth, our assumption that mass is lost during coalescence events it might be surprising at first sight. In fact, there is a very clear physical reason for this. As shown in Section 1.6, a vapor bubble of radius R is in equilibrium with a liquid density that varies with R. Specifically, when Ostwald ripening is reversed for vapor bubbles, the liquid density $\phi_+(R)$ decreases with R (and this is the very reason for which Ostwald ripening is reversed). Consider now two vapor bubbles of equal radii R that coalesce into one of radius R_f. Once the resulting bubble has equilibrated with the outer liquid, the density of such liquid is lower than the one surrounding the original bubbles. This means that some of the vapor composing the two initial bubbles is ejected in the outside liquid, and thus that $R_f < \sqrt{2}R$: mass

is lost in a coalescence event. Because the Ostwald process conserves mass exactly, this also means that nucleation is the only process that can take into account for the mass lost during coalescence, and we approximate this process as instantaneous. As such, we obtain a model that exactly conserves the total mass (as it must be).

Finally, the Ostwald ripening interaction between multiple vapor bubbles close to each other is not known. Indeed, equation (1.56) for Ostwald ripening, considers a bubble that is very far away from other bubbles and sees them just through a correction to the density of the liquid. Setting up our model, we assumed that this can be approximated as a sum of pairwise interactions and, for simplicity, we opted for an interaction with just the nearest neighbor.

Despite our crude approximations, we show below that much of the phenomenology found both in AMB+ and particle models is reproduced. This serves as a-posteriori check that all these details are not crucial at phenomenological level, although they could quantitatively change some of the fine properties of micro and bubbly phase separation.

4.1.2 Parameters

In this section we will review in more details the parameters of the model and how we choose them.

The free parameters in the model are:

- $D > 0$: set the diffusion constant for bubbles ($[D] = m^3/s$). This should not be confounded with the noise intensity D appearing in AMB+ equations (1.30).
- β: sets the speed with which a bubble loses or gains volume through the reverse Ostwald ripening process. The dimensions of β are the same as the diffusivity D ($[\beta] = m^3/s$). We choose $\beta > 0$, corresponding to reverse Ostwald ripening. The opposite case, corresponds to systems with standard equilibrium-like phase separation. In that case, the steady state is a single large bubble (vapor-liquid bulk phase separation). Indeed, if we initialize the system in a state with a large bubble in a sea a smaller bubbles, the large bubble can only grow (though both Ostwald Ripening and coalescence). We checked this fact numerically.
- $0 < \alpha_C < 1$: $1 - \alpha_C$ sets how much mass is lost in a binary coalescence ($[\alpha_C] = 1$). The higher α_C, the more efficient the coalescence process is.
- $R_0 > 0$: Radius at which bubbles are nucleated. It sets the spatial scale of the system ($[R_0] = m$).
- $0 < v_g < 1$: Vapor fraction in the system, computed as the total volume occupied by vapor V_G divided by the system volume V. As V_G is conserved by the dynamics of this model and V is constant, v_g is also a conserved quantity.

As we are free to choose time and a length scales arbitrarily, we fix $2R_0 = 1$ and $\beta = 1$. Moreover, we focus on the diffusivity and Ostwald ripening interplay and we fix $\alpha_C = 0.9$. Since β and L set the spatial and temporal scale of the simulations, by varying D we are actually tuning the competition between diffusion – and hence coalescence – and reverse Ostwald ripening. The same can be said for v_g that regulates the vapor at disposal in the system. Indeed, when less vapor is available bubbles are more distant and the coalescence process is less important.

Technical parameters of the system are, instead, the system volume $V = L \times L$ and the time resolution given by $\Delta t > 0$. We used different temporal discretisations for the bubble diffusion and the Ostwald dynamics. Indeed, the two processes requires different precision to provide reliable results. For the Ostwald dynamics we use $\Delta t_{Ost} = 0.01$, as higher values resolves badly the nonlinearities of Eqs. (4.2)-(4.3). Unless otherwise stated, $\Delta t = 0.1$. In Appendix C.2 we describe the motivation of this choice and its stability.

4.2 Low noise phase diagram

Is this minimal model able to reproduce the phenomenology of micro- and bubbly phase separation? We will show that this is not only the case, but that this minimal model even shed light on the physics of these phases. In this section, we start from the case of small D/β and hence the Ostwald process dominates over coalescence. As we will see, in this regime finite-size effects are small and time-convergence is fast: it is hence the simplest regime to study computationally. In Section 4.3 we compare this regime to the opposite one, at high diffusivity D/β.

In Figure 4.1 we provide snapshots in the steady state for different vapor fractions v_g. Both microphase separation at high density and bubbly phase separation at low density are observed. We then check whether the statistical properties of these two phases are analogous to the one we studied in Chapter 2, and whether this conclusion holds asymptotically in system size.

4.2.1 Micro-phase separation (homogeneous bubbly liquid)

At high densities $1 - v_g$, the system is found in the micro-phase separated state. In this phase a sea of bubbles of different sizes nucleate, diffuse, and coalesce. Analogously at what we did in Chapter 2 for AMB+, we analyze the statistical properties of the bubbly liquid by building and studying the bubble size distribution $P(A)$. In Figure 4.2, we report the results of these study: in the deep bubbly liquid the bubble size distribution $P(A)$ presents a peak corresponding to the typical size of bubbles, and an exponential tail. These results are converged in both time and system-size.

For the system parameters presented in Figure 4.2, Ostwald ripening dominates

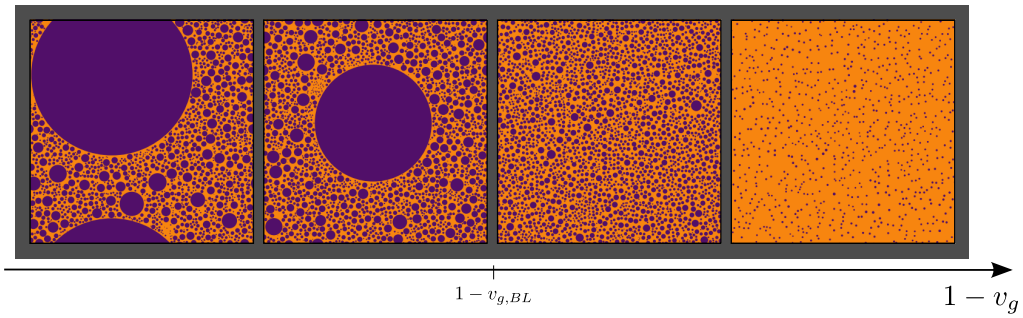

Figure 4.1: Finite size phase diagram at fixed diffusivity $D = 0.01$. We can observe the emergence of a micro-phase separated state that we identify with the bubbly liquid, and a macro phase separated state between a large bubble and a sea of smaller bubbles around (bubbly phase separation). Snapshots for system size $L = 400$. From left to right, vapor fractions are as follows: $v_g = 0.7, 0.6, 0.4, 0.05$

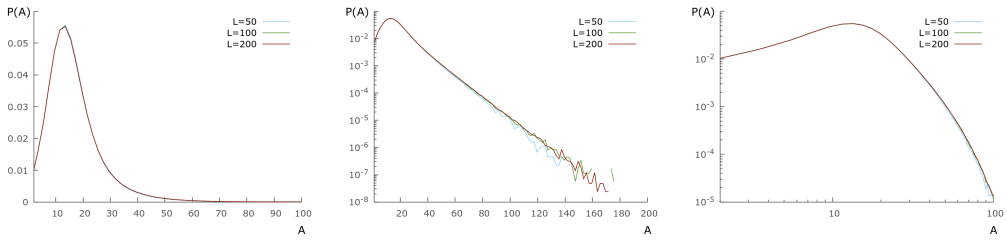

Figure 4.2: Convergence in size of the PDF of bubble size $P(A)$ in the bubbly liquid at noise level $D = 0.1$ and $v_g = 0.3$. From left to right we present the same data in lin, loglin and log formats. Notice how $P(A)$ presents a peak corresponding to the typical bubble size, and exponential tails.

over coalescence: this results in bubbles with similar sizes and small size variability. Now, if we increase the amount of vapor in the system (and thus v_g) or the bubble diffusivity D, the peak is less defined and the exponential cut-off is shifted at larger values (see Fig. 4.3). This results in a larger average bubble size, as we see in Fig. 4.5. The mechanism behind this is the same we explained in Chapter 2. Indeed, by increasing the vapor available in the system we decrease (on average) the distances between bubbles, and favor coalescence over Ostwald ripening (that instead tends to uniform bubble sizes); this generates a larger variability of bubbles sizes. In the same way, if we increase diffusivity, bubbles will move faster and coalesce more frequently.

In Chapter 1.6, we saw that a crucial difference between the bubbly liquid and the bubbly phase separation reside in the convergence time. We will study this aspect also in the minimal bubbles model, by extrapolating the convergence time

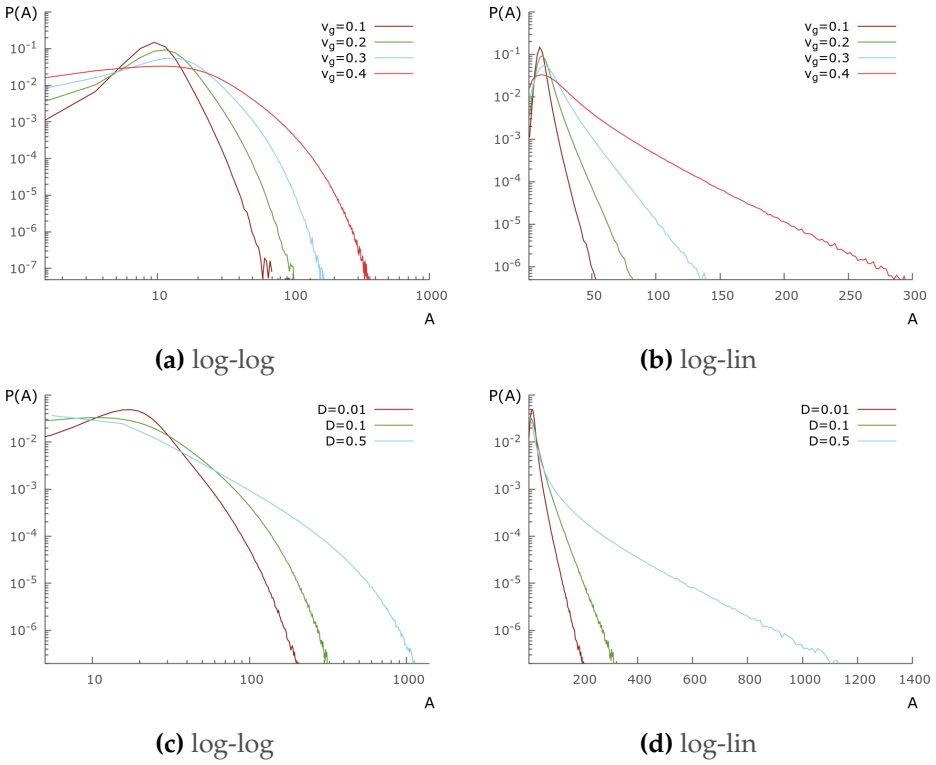

(a) log-log **(b)** log-lin

(c) log-log **(d)** log-lin

Figure 4.3: Bubble size distribution $P(A)$ in the bubbly liquid phase by varying v_g (first line) and D (second one). In the first column we present the data in log scale, while in the second in log-lin scale to highlight the exponential tail of the distribution. Notice how, when coalescence is favored against Ostwald ripening (by increasing v_g or D) bubble size variability is increased: the peak of $P(A)$ becomes less prominent, and its exponential tails slower.
Parameters are chosen as follows:
(a,b): $L = 200, D = 0.1, v_g \in [0.1, 0.4]$
(c,d): $L = 200, D \in [0.01, 0.5], v_g = 0.4$

τ_{ss} from the time series of the average number of bubbles $A_{bub}(t)$. In particular, we use the same techniques used for AMB+ (see Section 2.3.2). As we can see in Fig.4.4, convergence in time is fast and does not depend on system size. Indeed, by changing system-size, we merely rescale fluctuations around the average value. On the contrary we do have a dependence of τ_{ss} on the diffusivity D: the higher D, the faster the convergence time is. These results are very similar to those we obtained in Chapter 2 for AMB+ in the homogeneous bubbly phase. We now turn to analyse bubbly phase separation.

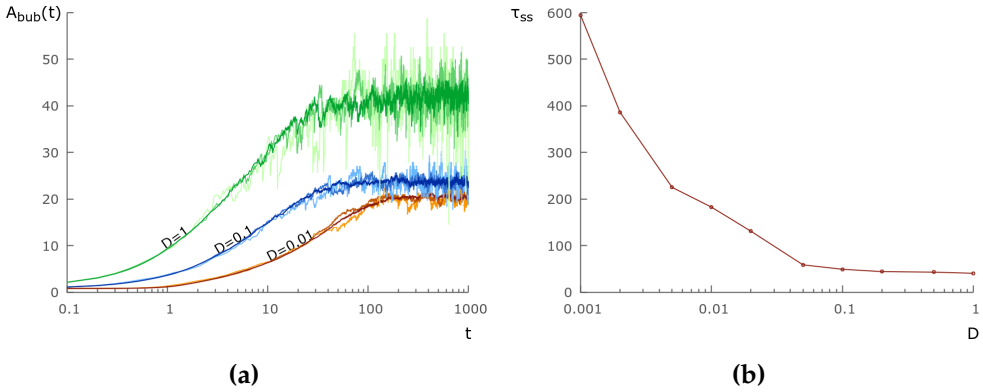

Figure 4.4: Behavior of the convergence time τ_{ss} in the bubbly liquid ($v_g = 0.4$) when varying the diffusivity D.
(a) Time series of the average bubble size. For each diffusivity constant ($D = 0.01, 0.1, 1$), we show three time series at different system sizes (($L = 50, 100, 200$, from light to dark color). As we can see, the convergence time does not depend on the system size while it depends on D.
(b) From time series analogous to the one in (a) we extracted the convergence time τ_{ss} as we described in Section 2.3.2 for AMB+. Notice how the convergence time decreases when increasing D.

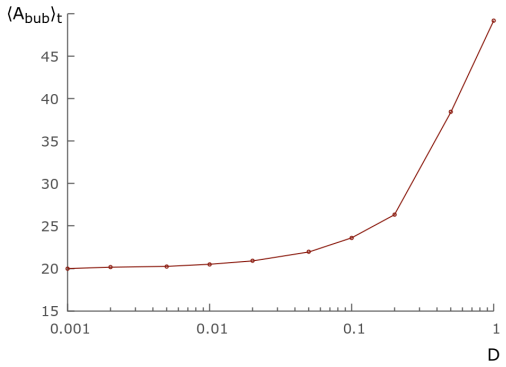

Figure 4.5: Average bubble size in bubbly liquid steady-state when varying the diffusivity D. System size $L = 300$, gas fraction $v_g = 0.4$.

4.2.2 Bubbly phase separation

As we saw in the previous section, in the bubbly liquid, for a fixed diffusivity constant D, by increasing the vapor fraction v_g, the bubble size variability increases: the average bubbles size is larger and the exponential cut-off in $P(A)$ shifts to larger sizes. By further increasing the vapor fraction in the system (Fig. 4.6), we find the bubbly phase separated state. This state is a macro-phase separated state between a

vapor reservoir (i.e. the largest bubble in the systems, whose volume scales linearly with the total volume V) and bubbly liquid with a vapor fraction $v_{g,BL}$. As is customary in bulk phase separations, we then have (asymptotically) the bubbly phase separation for volume fractions $v_{g,BL} < v_g < 1$.

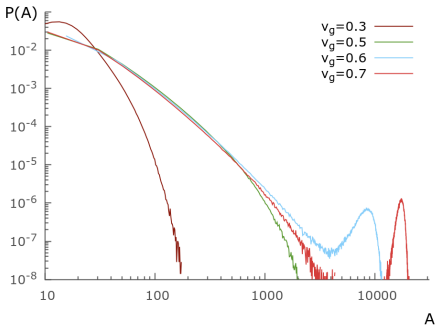

(a) $L = 200$

Figure 4.6: Bubble size distribution $P(A)$ passing through the transition between bubbly liquid and bubbly phase separation by increasing the gas fraction v_g. Diffusivity level $D = 0.1$.

In other words, $v_{g,BL}$ corresponds to the vapor fraction v_g beyond which the transition from bubbly liquid towards bubbly phase separation happens. As we will see in more details later, we estimate $v_{g,BL} \simeq 0.5$: micro-phase separation is found when the liquid is the majority phase, while bubbly phase separation is found when the liquid is the minority phase.

We confirm this with two facts. First, we perform simulations at $v_g = 0.4$ and $v_g = 0.6$; we observe that the system attains micro-phase separation in the former case, and bubbly phase separation in the latter. Within the bubbly phase separated regime, the distribution of bubble sizes does depend neither on system-size nor on the overall value of v_g, see Fig. 4.7. Analogous results were obtained at various noise levels $D/\beta \leq 1$.

We then measure $v_{g,BL}$ as the quantity of vapor in the bubbly liquid (i.e., excluding the macroscopic bubble). Precisely:

$$v_{g,BL} = \frac{V - V_g}{V - V_{vr}} \,. \tag{4.9}$$

where V_{vr} is the volume occupied by the macroscopic vapor bubble. This second procedure gives $v_{g,BL} \sim 0.49 - 0.5$ for small values of D/β, see Fig. 4.8.

We finally study the convergence time τ_{ss} to the bubbly phase separated state in Fig. 4.9. In particular, we exploit the time-series of $v_{g,BL}(t)$ as defined above. Interestingly, as it was the case in AMB+, and at variance to the case where the system is heading towards the micro-phase separated state, the convergence time increases with system-size. We thus confirm the robustness of this surprising result.

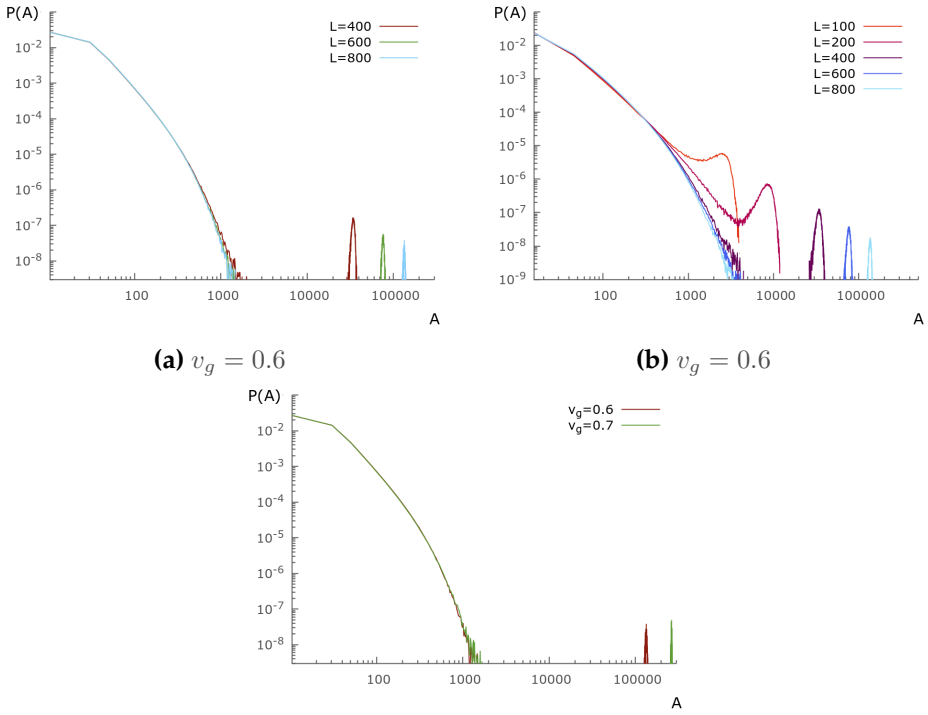

(a) $v_g = 0.6$ **(b)** $v_g = 0.6$

(c) $L = 800$

Figure 4.7: Bubble size distribution $P(A)$ in the bubbly phase separation at $D = 0.01$ (a) and $D = 0.1$ (b). We can see how it does not depend on system size or vapor fraction v_g when converged in system size. In (c) we show that the distribution of bubbles in the microphase separated state does not depend on the overall volume fraction v_g either ($D = 0.01$).

By doing so we obtained Fig. 4.8, from which we can see that $v_{g,BL} \approx 0.49$. Finally, in Fig. 4.8(b) we see that the same value is attained for simulations with different v_g.

Concluding, for systems at low diffusivity D we are able to study the system asymptotically both in time and system-size at any overall density (here represented by the amount of vapor in the system v_g). This confirms the presence of microphase separation when $0 < v_g < v_{g,BL}$ (liquid is the majority phase) and bubbly phase separation when it is the minority phase $v_{g,BL} < v_g < 1$. All the properties of the bubbly phase separated state that we found in AMB+ state are retrieved, among which the surprising increase of the typical time needed to converge to such state. We now investigate the regime of high diffusivity.

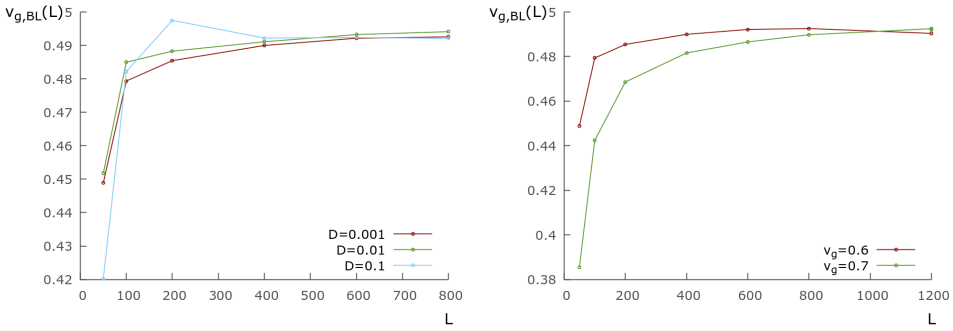

(a) $v_g = 0.6$ **(b)** $D = 0.001$

Figure 4.8: Steady-state vapor fraction in the bubbly liquid as a function of the linear system size L.
(a) Various (low) diffusivity levels D are shown.
(b) The same asymptotic level is reached for different vapor fractions v_g.

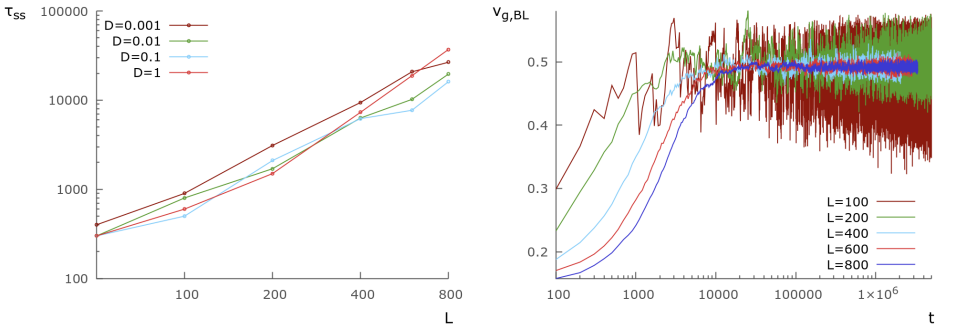

(a) **(b)**

Figure 4.9: (a) In the bubbly phase separation, the convergence time τ_{ss} increases exponentially with system-size. Various diffusivity level D are shown. $v_g = 0.6$.
(b) Vapor fraction in the bubbly liquid for $D = 0.1$, $v_g = 0.6$ and different system sizes L. From these time series we extracted τ_{ss} of Fig.(a).

4.3 Intermediate and high bubbles diffusivity

Increasing D/β increases finite-size effects; obtaining convergence in time and system-size becomes harder. In this section, we study the effect of increasing D on the system properties and on the convergence in system-size. This study is still ongoing, and we present here preliminary results.

First, we build in Fig.4.12 (a,b) the phase diagram at finite system-size for $L = 200$ and $L = 400$ by performing simulations at various diffusivity levels D

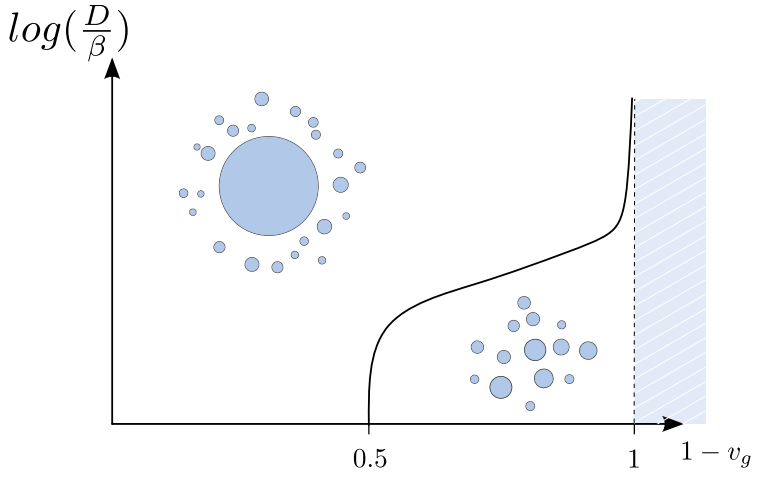

Figure 4.10: Tentative phase diagram D/β vs $1 - v_g$ in the asymptotic regime of the effective bubble model.

and vapor fraction v_g. The phase diagram at finite system-size is necessarily ambiguous, as both micro-phase separation and bubbly phase separation are precisely defined only asymptotically. Neverthless, analysing the bubble size distribution $P(A)$, we distinguish the following cases: (blue dots) the distribution of bubble sizes is continuous and monotonous decreasing with A; (yellow dots) is when $P(A)$ shows a peak at large values of A. Observe that this can correspond either to a peak well-separated from the size distribution of other bubbles, when there is a bubble much larger than all the others, or not; we do not distinguish these two cases for the moment, as there is not a simple way to do so without comparing results at different sizes.

The first clear conclusion is that, increasing D/β at fixed system-size, favors bubbly phase separation. Indeed, for $D/\beta > 1$, this is observed even for $v_g < 0.5$. This is natural, given that a large bubble will increase by coalescence and shrink by reversed Ostwald ripening.

We now turn to study finite-size effects focusing on $v_g = 0.4$ and $v_g = 0.6$, see Fig. 4.12 (c,d). As already shown in Section 4.2.1, at low D/β we easily attain convergence in time and system-size both to the micro- and bubbly phase separated one. In fact, we have also attained convergence in system-size at high values of D/β, where the system converges to bubbly phase separation at both values of v_g, see Fig. 4.11 and 4.12 (c,d). This proves that the transition line between micro-phase separation, asymptotically, shifts to lower values of v_g upon increasing D. Indeed, consistently, the measure for $v_{g,BL} \simeq 0.065$ at $D = 20$ based both on simulations performed at $v_g = 0.4$ and $v_g = 0.6$.

The case of intermediate values of D/β is the most difficult to study as the finite-size effects are larger so that convergence will be attained at larger systems and

longer times. However, we have no sign of qualitative differences at play. As such our current conclusion is that the phase diagram of the model is qualitatively given by Fig. 4.10. In the near future, we will check such statement in details optimising the code we employed; this is possible as the bottleneck for large systems is given by a single step, nucleation, which can be made more efficient.

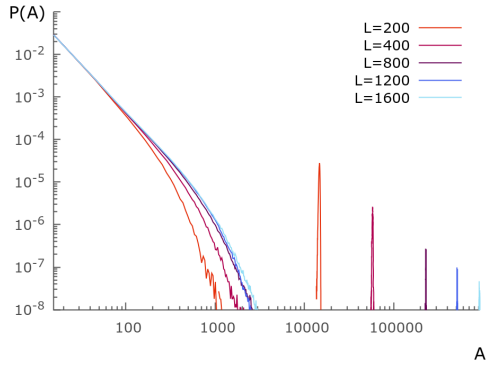

(a)

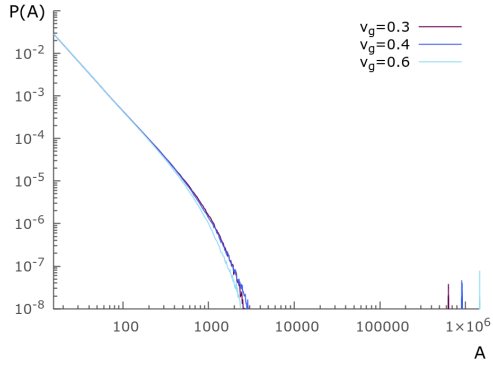

(b)

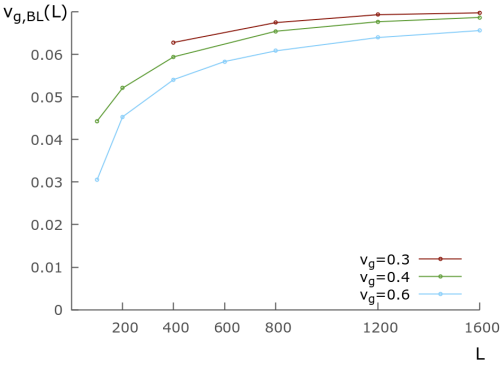

(c)

Figure 4.11: Asymptotic convergence in system size of the bubbly phase separation at high diffusivity ($D = 20$).
(a) Bubble size distribution $P(A)$ convergence for $v_g = 0.4$ at various system sizes L
(b) Bubble size distribution $P(A)$ varying vapor fraction when convergence in size is attained (at least for $v_g = 0.4$ and 0.3).
(c) Fraction of gas in the bubbly liquid $v_{g,BL}$ convergence with size. Different curves represent different vapor fractions.

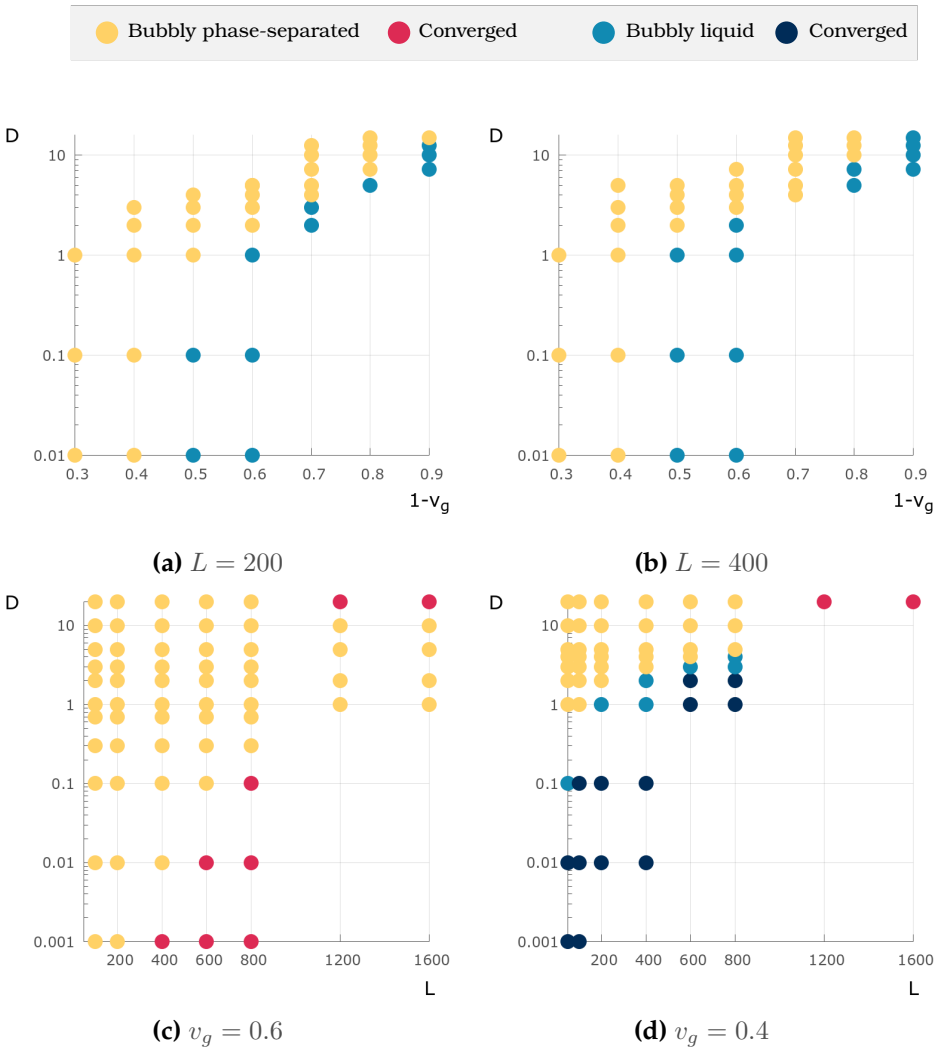

Figure 4.12: (a,b) Finite size $D \times 1 - v_g$ phase diagram for two different sizes, $L = 200$ and $L = 400$. Blue and yellow dots represent, respectively, where we observe the microphase separated state (homogeneous bubbly liquid) or bubbly phase separation. See the main text for a precise definition of the two cases at finite system-size. Red and black dots represents where we see these two phases and the statistics of the bubble-size distribution is converged both in time and system-size. Clearly, increasing diffusivity at fixed system-size is favoring bubbly phase separation, which is observed even when the liquid is the majority phase ($v_g < 0.5$).
(c,d) System size behavior of the phase diagram in (a,b) for fixed vapor fraction $v_g = 0.4$ and $v_g = 0.6$ and various diffusivity levels D.

4.4 Conclusions

In this chapter we studied a minimal model of vapor bubbles nucleating, diffusing, coalescing and interacting with the first neighbors through Ostwald Ripening. This confirms all statistical properties that we have found in Chapter 2 when studying AMB+. The advantage of this model is that it allows to tune independently the rate of Ostwald ripening β and the diffusion constant of bubbles D, which determines their coalescence rate.

Importantly we discovered that finite-size effects and the timescale for convergence to the steady state crucially depend on the non-dimensional parameter D/β. For low and high values of D/β, we obtained results converged in both time and system size.

When $D/\beta \ll 1$, the transition between bubbly phase separation and the microphase separated state happens at $v_g = 0.5$: the system is in the homogeneous bubbly phase when the liquid is the majority phase and it is bubbly phase separated when the liquid is the minority phase. Increasing D/β, such transition line moves to lower values of v_g (larger global densities). Bubbly phase separation is found even when the liquid is the majority phase.

Models of active particles undergoing MIPS, are often observed in the bubbly phase separated regime even at global densities where the liquid is the majority phase [1, 2, 59]; this suggests that these models are in the regime of intermediate or large D/β. The minimal model studied in this Chapter teaches us that finding a way to tune D/β in these particle models is a very interesting avenue, crucial to control finite-size effects, and is left for the future.

At intermediate values of the diffusivity ($D/\beta \sim 1$), we were unable so far to obtain results that are converged in system-size. Yet, our preliminary results indicates that no novel physics is at play, except for the fact that finite-size effects are stronger in this regime. This point will be clarified in the near future by means of a more efficient code. We will also look for a first principle derivation of the diffusion law (4.1) that we have assumed for vapor bubbles and/or consider the case where $D \propto R^\alpha$, $\alpha > 0$, which might be similar to the limit of large D values in the model studied here.

Chapter 5

Conclusions

Active phase separation is one among the most fundamental collective phenomena that we can observe in active matter systems. In particular, due to its intrinsic non-equilibrium nature, it displays features that cannot be observed at equilibrium. Strikingly, active systems, unlike equilibrium ones, can phase separate even in the absence of attraction among particles [47, 48]. This is driven by the positive feedback between the slow-down of particles in high density areas and vice-versa, their accumulation in slow moving areas. This phenomenon is known as motility-induced phase-separation (MIPS) and has been widely studied in the literature. MIPS was first understood via an approximate mapping to equilibrium liquid-vapor phase separation; it is nowadays clear that in active systems more complex types of phase separation can arise, as we contributed to show with this Thesis.

Specifically, in Chapter 2 and 3, we adopted the coarse grained point of view of Active Model B+ (AMB+) [60], a minimal field theory built on symmetry arguments and conservation laws that describes phase separation in the absence of time-reversal symmetry. Then, in Chapter 4 we define and study a minimal model of diffusing bubbles to link our AMB+ results, with those that have been recently observed in models of repulsive active particles [1, 2].

We now review our main results.

Field theoretical analysis of active phase-separation predicts the emergence of purely non equilibrium types of phase separation in active systems. This feature stem form the possibility of active system to have a negative interfacial tension linked to the Ostwald process, that can therefore go into reverse [60]. When this happens, the system self-organizes in either a micro phase-separated state, in which vapor bubbles diffuse in a dense liquid phase (bubbly liquid), or in a bulk phase-separated state in which bubbly liquid coexists with an outer homogeneous vapor (bubbly phase separation). In Chapter 2, we performed an in-depth numerical study of the statistical properties of these two phases, by using an efficient pseudo spectral code that we developed. Thanks to this numerical effort we were able

to simulate large system, and for longer times with respect to previous attempts [60]; we were able to attain convergence in both time and system size, in both phases. This allowed us to obtain one of the major results of the chapter, by proving that the bubbly phase separation is indeed a bona-fide phase separation between the bubbly liquid and the uniform vapor phase (both with a well-defined density). Surprisingly, we discovered that the convergence, both in time and system size, is significantly longer when is towards bubbly phase separation (rather than the microphase separated state); moreover, the typical convergence time increases with system-size.

Despite our results, we were unable to fully understand some points, that calls for future studies (especially analytical ones). In particular, the behavior of the convergence time towards the bubbly phase separated state, the infinite time and space limit of the transition from the microphase separated state to the homogeneous liquid, and finally the coarsening law of growing domains.

In Chapter 3, we entered the long-lasting debate about a proper definition of interfacial tension in active system. In passive systems, the interfacial tension is a well-defined quantity, and is responsible for several phenomena, like the Ostwald ripening process, the Laplace pressure jump, and the elastic properties of the interface; on the contrary, we have shown that in active systems it is not possible to adopt one single definition for it.

We have described, both analytically and numerically, the capillary wave interfacial tension responsible for the fluctuation properties of the interface and the spectrum of the capillary waves. In particular, we did so by deriving from first principles the capillary wave theory for active system and see how it differs from the one responsible for Ostwald ripening. With that, we were able to perfectly predict the decay rate of interfacial fluctuations and the spectrum of capillary waves fully from first principles.

Surprisingly, moreover, we discovered that the capillary interfacial tension can get negative because of activity, while still maintaining a phase separated state. In such situation, analogously at what happen when the Ostwald tension is negative, novels phases of matter arise: a new type of micro-phase separation where coalescence is highly inhibited and an 'active foam state'. These were previously unknown, and we studied their properties.

The techniques we introduced in Chapter 3 could be used in the future to elucidate the capillary tension in particle-based active models, by applying them to various field-theoretical descriptions obtained by explicit coarse-graining [60, 52, 88], or to describe confluent biological tissues, where the measured interfacial tension was recently shown to be dependent on the measuring protocol [89].

The results contained in Chapter 3 were recently published in *Physical Review Letters* [3].

We concluded with Chapter 4, by presenting preliminary results on a minimal model of diffusing bubbles interacting by reversed Ostwald ripening and coales-

cing upon contact. One of the main reasons to study this model was to shed light on the properties of bubbly and micro- phase separation in particle-based models of active systems, where bubbles were found to have a very strong variability in size [1, 2], a fact that made it very complicated to study the statistical properties of these two phases. Indeed, in particle models, attaining system-size convergence within the bubbly phase-separated regime has proven practically impossible so far, while convergence in the bubbly liquid can be attained just very close to the liquid binodal [1].

The advantage of the effective bubble model we introduced and studied, is that it allows to tune independently the rate of Ostwald ripening β and the diffusion constant of bubbles D, which determines the coalescence rate of bubbles. Our main result was to show that D/β sets the strength of finite-size effects and changes the density of the bubbly liquid when the system is bubbly phase-separated. For small and large values of the non-dimensional ratio D/β we attained convergence in system-size both in the micro-phase separated regime and in the regime of bubbly phase separation. At intermediate values of the diffusivity ($D/\beta \sim 1$), we were unable so far to obtain results that are converged in system-size, but our preliminary results indicate that no novel physics is at play (except for the fact that finite-size effects are stronger in this regime). We plan to clarify this point in the near future.

Interestingly, models of active particles undergoing MIPS are often observed in the bubbly phase separated regime even at global densities where the liquid is the majority phase [1, 2, 59]; this suggests that these models are in the regime of intermediate or large D/β. The minimal model studied in this Chapter teaches us that finding a way to tune D/β in these particle models is a very interesting avenue, crucial to control finite-size effects, and is left for the future.

Chapter 6

Synthèse en français

La séparation de phase active est l'un des phénomènes collectifs les plus fondamentaux que nous pouvons observer dans les systèmes de matière active. En particulier, en raison de sa nature intrinsèque de non-équilibre, elle présente des caractéristiques qui ne peuvent être observées à l'équilibre. Etonamment, les systèmes actifs, contrairement aux systèmes à l'équilibre, peuvent se séparer en phase même en l'absence d'attraction entre les particules [47, 48]. Ce phénomène est dû à la rétroaction positive entre le ralentissement des particules dans les zones à forte densité et vice-versa, leur accumulation dans les zones à mouvement lent. Ce phénomène est connu sous le nom de séparation de phase induite par la motilité (MIPS) et a été largement étudié dans la littérature. La MIPS a d'abord été comprise via une cartographie approximative de la séparation de phase liquide-vapeur à l'équilibre ; il est aujourd'hui clair que dans les systèmes actifs, des types plus complexes de séparation de phase peuvent apparaître, comme nous avons contribué à le montrer dans cette thèse.

Plus précisément, dans les Chapitres 2 et 3, nous avons adopté le point de vue à grand échelle du modèle actif B+ (AMB+) [60], une théorie de champ minimal construite sur des arguments de symétrie et des lois de conservation qui décrit la séparation de phases en l'absence de symétrie temporelle inverse. Ensuite, dans le chapitre 4, nous définissons et étudions un modèle minimal de bulles diffusantes pour relier nos résultats AMB+, avec ceux qui ont été récemment observés dans des modèles de particules actives répulsives [1, 2].

Nous passons maintenant en revue nos principaux résultats.

La théorie des champs applique à la séparation de phase active prédite l'émergence de types de séparation de phase purement non équilibrés dans les systèmes actifs. Cette caractéristique provient de la possibilité pour un système actif d'avoir une tension interfaciale négative liée au processus d'Ostwald, qui peut donc s'inverser [60]. Cela signifie, par exemple, qu'en présence d'une séparation de phases, les petites bulles de vapeur se développent au détriment des grandes.

Lorsque cela se produit, le système s'auto-organise soit dans un état de micro-séparation de phase, dans lequel les bulles de vapeur diffusent dans une phase liquide dense (liquide bouillonnant), soit dans un état de séparation de phase en vrac dans lequel le liquide bouillonnant coexiste avec une vapeur homogène externe (séparation de phase bouillonnante, voir Fig. 6.1).

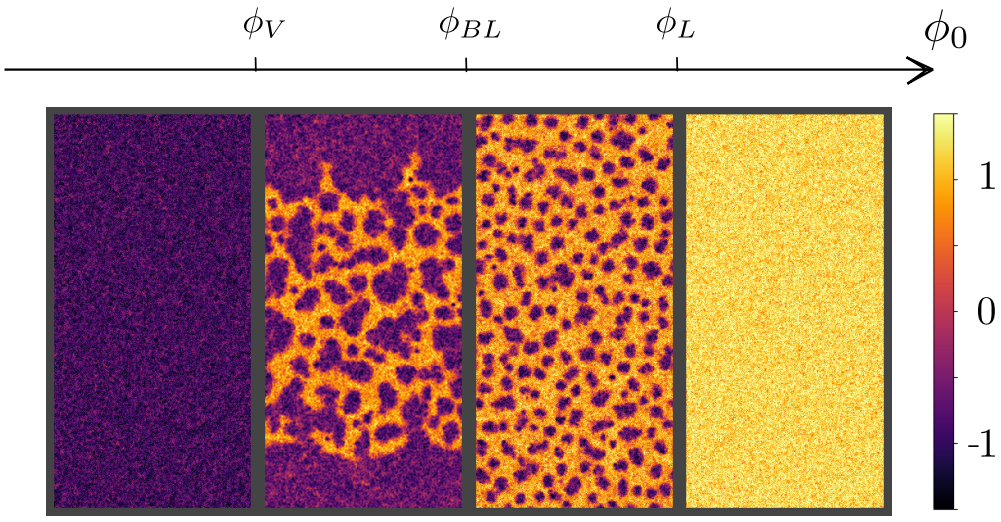

Figure 6.1: De gauche à droite, des instantanés des différentes phases de l'AMB+ rencontrées lors de l'augmentation de la densité globale ϕ_0 : phase vapeur homogène, séparation de phase bouillonnante, phase liquide bouillonnante et liquide homogène.

Dans le Chapitre 2, nous avons effectué une étude numérique approfondie des propriétés statistiques de ces deux phases, en utilisant un code pseudo spectral efficace que nous avons développé. Grâce à cet effort numérique, nous avons pu simuler de grands systèmes, et pour des temps plus longs par rapport aux tentatives précédentes [60] ; nous avons pu atteindre la convergence à la fois en temps et en taille de système, dans les deux phases. Cela nous a permis d'obtenir l'un des résultats majeurs du chapitre, en prouvant que la séparation de phase de bulles est bien une séparation de phase authentique entre le liquide de bulles et la phase vapeur uniforme (tous deux avec une densité bien définie). Pour ce faire, nous avons étudié les propriétés statistiques du liquide de bulle à travers sa distribution de taille de bulle et son profil de densité (voir Fig.6.2 et 6.3). De manière surprenante, nous avons découvert que la convergence, à la fois en temps et en taille de système, est significativement plus longue lorsqu'on se dirige vers la séparation de phase bouillonnante (plutôt que vers le liquide bouillonnante) ; de plus, le temps de convergence typique augmente avec la taille du système.

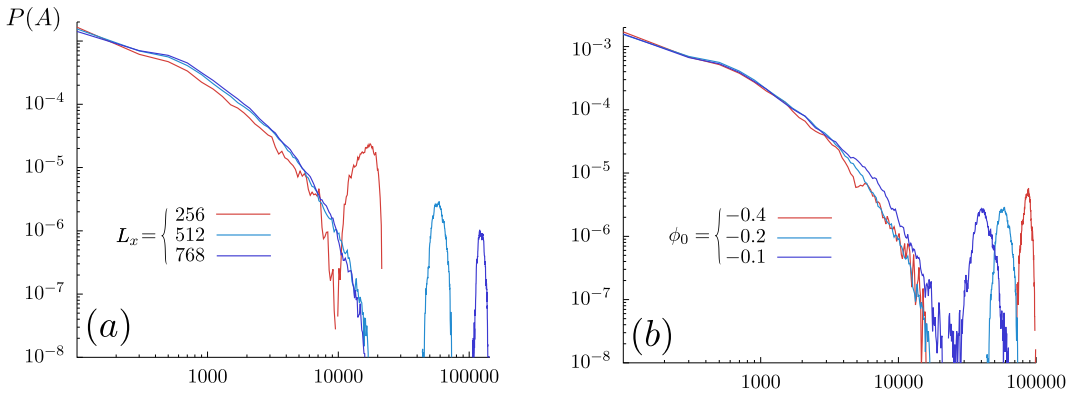

Figure 6.2: Convergence de la distribution de la taille des bulles $P(A)$
(a) $P(A)$ convergeant en taille de système.
(b) $P(A)$ convergent pour différentes densités globales ϕ_0.

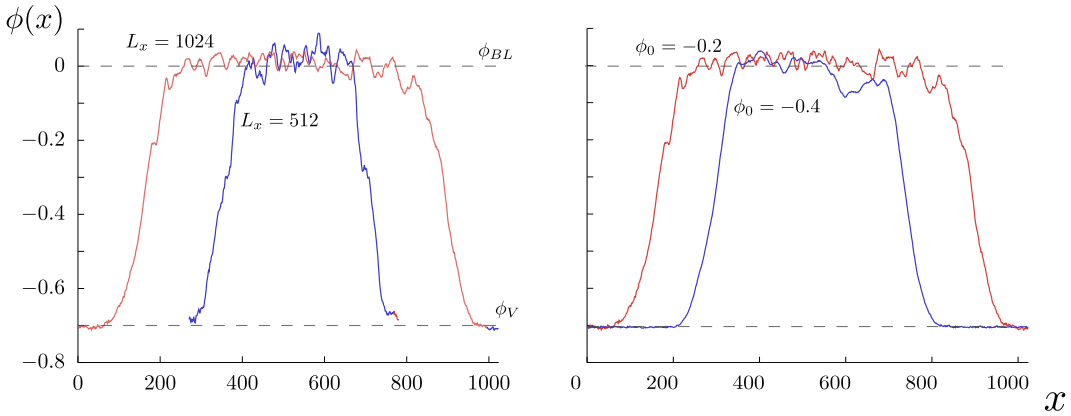

Figure 6.3: Profil de densité moyenne dans la séparation de phases à bulles (avec une géométrie de bande). Nous pouvons clairement distinguer les deux niveaux de densité du liquide de bulle ϕ_{BL} et de la vapeur ϕ_V. Ceux-ci ne dépendent pas de la densité globale ϕ_0, ni de la taille du système (lorsqu'elle est choisie suffisamment grande).

Malgré nos résultats, nous n'avons pas été en mesure de comprendre pleinement certains points, qui appellent à des études futures (en particulier analytiques). En particulier, le comportement du temps de convergence vers l'état de séparation de phases bouillonnantes, la limite de temps et d'espace infinie de la transition du liquide bouillonnant vers le liquide homogène, et enfin la loi de croissance des domaines en formation.

Dans le Chapitre 3, nous avons entamé un débat de longue haleine sur la définition correcte de la tension interfaciale dans les systèmes actifs. Dans les systèmes passifs, la tension interfaciale est une quantité bien définie, et elle est responsable

de plusieurs phénomènes, comme le processus de maturation d'Ostwald, le saut de pression de Laplace, et les propriétés élastiques de l'interface ; au contraire, nous avons montré que dans les systèmes actifs, il n'est pas possible d'adopter une définition unique pour elle.

Nous avons décrit, tant analytiquement que numériquement, la tension interfaciale des ondes capillaires responsable des propriétés de fluctuation de l'interface et du spectre des ondes capillaires. En particulier, nous l'avons fait en dérivant à partir des premiers principes, la théorie des ondes capillaires pour le système actif et en voyant comment elle diffère de celle responsable de la maturation d'Ostwald. Grâce à cela, nous avons pu prédire parfaitement le taux de décroissance des fluctuations interfaciales et le spectre des ondes capillaires à partir des premiers principes.

De manière surprenante, nous avons en outre découvert que la tension interfaciale capillaire peut devenir négative en raison de l'activité, tout en maintenant un état de séparation de phases. Dans une telle situation, de manière analogue à ce qui se passe lorsque la tension d'Ostwald est négative, de nouvelles phases de matière apparaissent : un nouveau type de séparation de microphases où la coalescence est fortement inhibée et un "état de mousse active". Ces phases (voir Fig.6.4) étaient auparavant inconnues, et nous avons étudié leurs propriétés.

Les techniques que nous avons présentées dans le Chapitre 3 pourraient être utilisées à l'avenir pour élucider la tension capillaire dans les modèles actifs à base de particules, en les appliquant à diverses descriptions théoriques de champ obtenues par un raisonnement grossier explicite [60, 52, 88], ou pour décrire des tissus biologiques confluents, où il a été récemment démontré que la tension interfaciale mesurée dépendait du protocole de mesure [89].

Les résultats contenus dans le Chapitre 3 ont été récemment publiés dans *Physical Review Letters* [3].

Nous avons conclu avec le chapitre 4, en présentant des résultats préliminaires sur un modèle minimal de bulles diffusantes interagissant par maturation d'Ostwald inversée et coalesçant au contact (voir fig. 6.5).

L'une des principales raisons d'étudier ce modèle était de faire la lumière sur les propriétés du liquide bouillonnant et de la séparation des phases bouillonnant dans les modèles de particules de systèmes actifs, où l'on a constaté que les bulles avaient une très forte variabilité de taille [1, 2], un fait qui rendait très compliquée l'étude des propriétés statistiques de ces deux phases. En effet, dans les modèles de particules, il s'est avéré pratiquement impossible jusqu'à présent d'atteindre la convergence de la taille du système dans le régime de séparation des phases bouillonnant , alors que la convergence dans le liquide bouillonnant peut être atteinte juste très près de la binodale du liquide [1].

L'avantage du modèle de bulles effectif que nous avons introduit et étudié, est qu'il permet de régler indépendamment le taux de maturation d'Ostwald β et la constante de diffusion des bulles D, qui détermine le taux de coalescence des bulles. Notre principal résultat a été de montrer que D/β définit la force des effets de taille

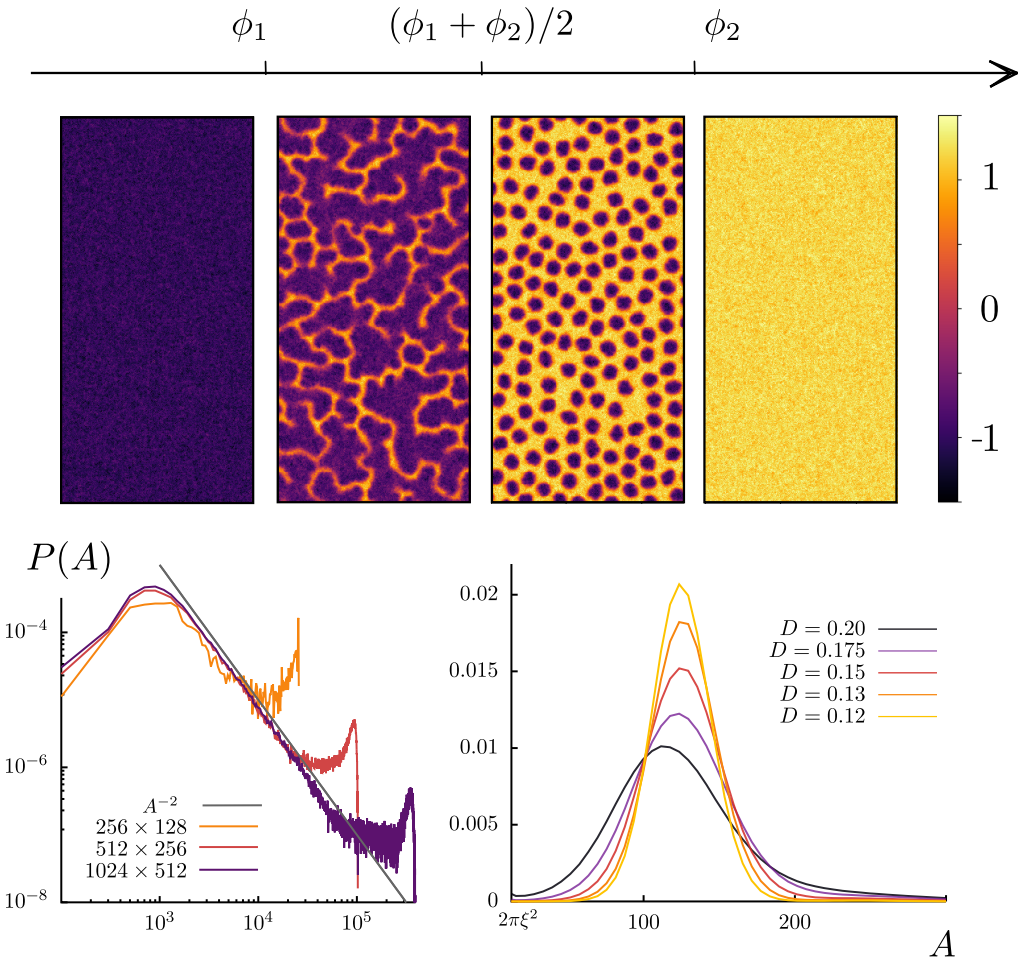

Figure 6.4: (En haut) diagramme de phase lorsque la tension interfaciale responsable de la propriété élastique de l'interface est négative ($\sigma_{\rm cw} < 0$) en fonction de la densité globale A haute et basse densité globale ϕ_0, le système est homogène (états liquide ou vapeur). Pour des valeurs intermédiaires lorsque le liquide est la phase majoritaire, le système présente des bulles de vapeur (microseparation de phase) dont la coalescence est fortement inhibée. À des valeurs inférieures de ϕ_0, le système forme un état de mousse active en évolution continue. (En bas) : distribution de la surface des régions de vapeur pour l'état de mousse active (gauche) et dans l'état de microphase séparée (droite).

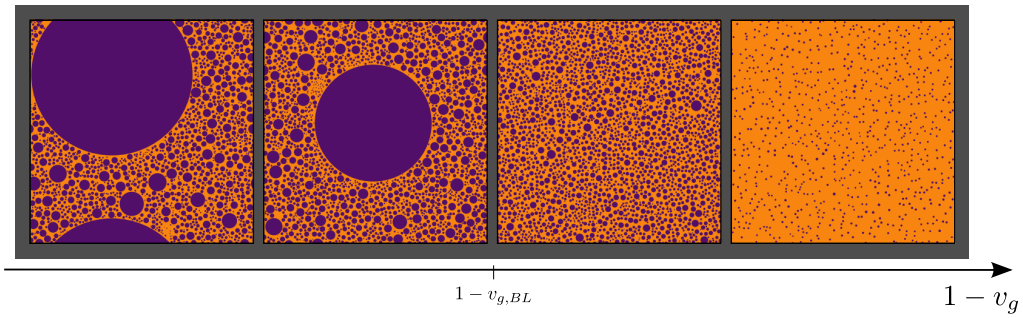

Figure 6.5: Diagramme de phase de taille finie à faible diffusivité. Nous pouvons observer l'émergence d'un état de micro-séparation de phase que nous identifions avec le liquide bouillonnant, et un état de macro-séparation de phase entre une grande bulle et une mer de bulles plus petites autour (séparation de phase bouillonnante). De gauche à droite, les fractions de vapeur diminuent (donc la densité globale ϕ_0 augmente).

finie et modifie la densité du liquide de bulle lorsque le système est en phase de séparation de bulles. Pour des valeurs petites et grandes du rapport non dimensionnel D/β, nous avons atteint une convergence dans la taille du système à la fois dans liquide bouillonnant et dans le régime de séparation en phase bouillonnante. Pour des valeurs intermédiaires de la diffusivité ($D/\beta \sim 1$), nous n'avons pas été en mesure jusqu'à présent d'obtenir des résultats qui convergent en taille de système, mais nos résultats préliminaires indiquent qu'aucune nouvelle physique n'est en jeu (excepté le fait que les effets de taille finie sont plus forts dans ce régime). Nous prévoyons de clarifier ce point dans un avenir proche.

Il est intéressant de noter que les modèles de particules actives subissant MIPS sont souvent observés dans le régime de séparation de phases bouillonnantes, même à des densités globales où le liquide est la phase majoritaire [1, 2, 59] ; ceci suggère que ces modèles se trouvent dans le régime de D/β intermédiaire ou grand. Le modèle minimal étudié dans ce chapitre nous apprend que trouver un moyen d'accorder D/β dans ces modèles de particules est une avenue très intéressante, cruciale pour contrôler les effets de taille finie, et est laissée pour le futur.

Appendix A

Simulations and data analysis

This appendix is devoted to the explanation of the code we developed and used to simulate AMB+ equations (1.30) in Chapter 2 and 3, as well as the algorithms that we developed to analyze the resulting outcomes. In Sec. A.1, we describe the algorithm used to integrate in time the equations, its stability and performance. Then, in Sec. A.2, we present two fundamental algorithms we employed to perform the data analysis on the density field $\phi(x, y)$. In particular, we describe the algorithms to locate vapor bubbles and liquid-vapor interfaces (in a bulk phase separated system).

A.1 Integrating AMB+ equations

In this section, we present the code used to integrate Eq. (1.30) to obtain the results described in Chapter 2 and 3.

Eq. (1.30) is a nonlinear partial differential equation describing the time evolution of the conserved density field $\phi(\boldsymbol{x}, t)$ at spatial coordinate $\boldsymbol{x}$. The objective is to integrate such equations in two dimensions for systems of volume $V = L_x \times L_y$ using periodic boundary conditions. This setup is particularly convenient computationally, as it allows implementing, using simple Fourier transforms, pseudo-spectral codes. The density field $\phi(x, y, t)$ is defined on a $N_x \times N_y$ square lattice. The distance between neighboring lattice points is equal to dx.

Throughout our study, we employed three types of initial conditions:

- uniform: the local density is uniformly set to a constant value:

$$\phi(x, y, t = 0) = \phi_0 \tag{A.1}$$

  That is a stationary solution of Eq. 1.30 when $D = 0$.

- random uniform: obtained from the uniform initial condition by adding uncorrelated noise to each lattice point:

$$\phi(x, y, t = 0) = \phi_0 + \psi \tag{A.2}$$

  where ψ is a uniform random variable and takes values in the interval $[-a, a]$. We used this initial condition when simulating systems with $D = 0$.

- band: phase-separated state between uniform liquid and vapor phases in contact through a flat interface. This corresponds to a band of liquid in a vapor background (or vice-versa):

$$\phi(x, y, t = 0) = \begin{cases} \phi_1 & 0 \leq x \leq x1, \forall y \\ \phi_2 & x_1 \leq x \leq x_2, \forall y \\ \phi_1 & x_2 \leq x \leq L_x, \forall y \end{cases} \tag{A.3}$$

  where ϕ_1 and ϕ_2 are usually chosen to be the mean field binodals value (± 1 for $\zeta = 2\lambda = 2$), while $x_1 - x_2$ depends on the chosen global density:

$$\phi_0 = 1/V \int_0^{L_x} \int_0^{L_y} dx dy \, \phi(x, y) \tag{A.4}$$

Time evolution between time t and $t + dt$ is computed using a direct Euler scheme. So, writing (1.30) in the form:

$$\frac{d\phi(t)}{dt} = G[\phi] \tag{A.5}$$

Where G is a functional of ϕ, we have:

$$\phi(t + dt) = \phi(t) + dtG[\phi(t)] \tag{A.6}$$

The code used to compute G in the original paper introducing AMB+ [60], is based on a finite difference algorithm. Instead, we opted for a pseudo-spectral implementation, as it is expected to be much more accurate. We explore the differences between these two approaches in the next two sections.

A.1.1 Finite difference algorithm

In the finite difference algorithm a derivative is simply treated like a difference, using a Taylor expansion. At first order, for example:

$$f(x + dx) = f'(x)dx + ... \tag{A.7}$$

gives:

$$\frac{df(x)}{dx} \approx \frac{f(x + dx) - f(x)}{dx} \tag{A.8}$$

higher order approximation that consider more lattice neighbors (in 1 or two directions) can be adopted to increase the precision of this method (that being algebraic for construction, goes like $\mathcal{O}(1/(dx)^n)$ for approximation of order n).

The development of a stable finite-difference code in [60] required the use of an approximation of high order ($n = 8$), and rotationally symmetric approximations of the equations of motion. The reason behind this are two. First, AMB+ equations contains high order derivatives are. Second, we know that nucleation events of spherical objects (vapor bubbles and liquid droplets) play a major role.

To gain accuracy and overcome these problems we developed a pseudo-spectral code, that relies on Fourier transforms to compute derivatives; being therefore exponentially precise in dx. Moreover, pseudo-spectral algorithms are generally easy to parallelize thanks to the existing libraries for Fast Fourier Transform (FFT). In the next section, we will see in details how it works.

A.1.2 Pseudo-spectral algorithm

The pseudo-spectral method is one of the main techniques used to solve nonlinear (and possibly noisy) partial differential equations. It exploits Fourier transforms to compute the linear terms of the equations, and in particular the derivatives, as they become simple multiplications in Fourier space. The non-linearities of the equation, instead, are expensive in the inverse space. Indeed, for a function f defined on N lattice points, even a simple quadratic term becomes a convolution whose computational cost is $\mathcal{O}(N^2)$:

$$\mathcal{F}[f(x,t)f(x,t)] = \mathcal{F}[f(x,t)] * \mathcal{F}[f(x,t)] \tag{A.9}$$

Where $\mathcal{F}$ is the Fourier transform operator, defined along with its inverse as follows:

$$\mathcal{F}[\cdot] = \int d\mathbf{x}\, e^{-i\mathbf{q}\cdot\mathbf{x}} \,. \tag{A.10}$$

$$\mathcal{F}^{-1}[\cdot] = \frac{1}{2\pi}\int d\mathbf{x}\, e^{i\mathbf{q}\cdot\mathbf{x}} \,. \tag{A.11}$$

For higher order nonlinearities the computational cost is even larger. For this reason, in a pseudo-spectral code, they are computed in the direct space. The price to pay for exploiting the best that the two worlds (direct and inverse space) have to offer, is the computation of several Fourier transforms and their inverse at each time step. This operation is done using the fast Fourier transform algorithm that scales as $\mathcal{O}(N \log N)$. Notice that for complex terms mixing derivatives and nonlinearities, we need to go back and forth the Fourier space several times. For example, the Fourier transform of $\boldsymbol{\nabla}\left(\nabla^2\phi(\boldsymbol{x})\boldsymbol{\nabla}\phi(\boldsymbol{x})\right)$ would be computed as follow:

$$-q^2\mathcal{F}\left\{\, \mathcal{F}^{-1}[-i\boldsymbol{q}\mathcal{F}[\phi(\boldsymbol{x})]]\, \mathcal{F}^{-1}[-q^2\mathcal{F}[\phi(\boldsymbol{x})]] \,\right\} \tag{A.12}$$

As is it customary when dealing with nonlinear differential equations, we use anti-aliasing to set to zero high frequency terms of the Fourier transform. The aliasing error comes from the fact that we are representing the field $\phi(x, y)$ on a discrete lattice: this means that high frequency signals that cannot be resolved are interpreted as lower frequency one. This introduces the so-called aliasing error that leads to errors in the numerical solutions and/or destabilize the code. One way to deal with is the two-third rule proposed by Orszag. Since the field $\phi(\boldsymbol{x})$ is defined on a lattice of $N_x \times N_y$ points (with N_x and N_y even), its Fourier transform $\phi(\boldsymbol{q})$ is defined on an inverse lattice of $N_x \times N_y$ points. Wave-numbers take values $(n_x, n_y)\epsilon[-\frac{N_x}{2}+1, \frac{N_x}{2}] \times [-\frac{N_y}{2}+1, \frac{N_y}{2}]$. The two-third rule consist in setting at each time-step:

$$\phi(\boldsymbol{q}) \to \begin{cases} 0 & q_\alpha < -\frac{N_\alpha}{2} + 1 + \frac{N_\alpha}{12} \quad \text{or} \quad q_\alpha > \frac{N_\alpha}{2} - \frac{N_\alpha}{12} \quad \alpha = x, y \\ \\ \phi(\boldsymbol{q}) & \text{otherwise} \end{cases} \tag{A.13}$$

This is especially needed after the computation of a nonlinearity that creates higher-frequency terms. For example, if we multiply two sinus of frequency ω we get an higher frequency term:

$$\sin(\omega x)\sin(\omega x) = -\frac{1}{2}\cos(2\omega x) \tag{A.14}$$

Moreover, in our case, there is another advantage of setting to zero higher frequency terms. Indeed, we are dealing with stochastic differential equations and adding uncorrelated noise to each lattice point in the system. Big fluctuations of

noise (even if they are rare events) might results in code instability if not resolved well enough in time and space. With the anti-aliasing method we are effectively adding correlation in the noise terms at high frequencies, limiting the effect of such rare events.

AMB+ equations are characterized by the presence of mixed terms (containing both nonlinearities and derivatives), and uncorrelated noise. This makes this code particularly susceptible to instabilities when space or time resolution are not sufficiently high. This is particularly true for nucleation events. As the nucleated objects in this model are spherical, the stability of the code for the same resolution is greater if the equations are explicitly isotropic. Therefore, instead of intergrating directly AMB+ equations 1.30, we manipulated their expression to explicit the isotropy of the deterministic part:

$$\dot{\phi} = \nabla^2 \left(a\phi + b\phi^3 - \left(\frac{\zeta}{2} + \lambda \right) \phi \nabla^2 \phi \right) + \frac{\lambda}{2} \nabla^4 (\phi^2) + \left(\frac{\zeta}{2} - \kappa \right) \nabla^4 \phi - \frac{\zeta}{2} (\nabla^2 \phi)^2 + \boldsymbol{\nabla \eta} \tag{A.15}$$

Finally, a few words about the implementation of the noise. In our code we perform the dynamical time-step to evolve the field $\phi(\boldsymbol{x}, t)$ in the Fourier space. The noise is therefore added through its Fourier components. In particular, for a wave-vector $\boldsymbol{q}$ the corresponding noise term is:

$$n(\boldsymbol{q}) = \mathcal{F}[\boldsymbol{\nabla} \eta] = (\xi_1 + i\xi_2)|\boldsymbol{q}| \tag{A.16}$$

where i is the imaginary unit, and $\xi_{1,2}$ are two independent random number distributed as a unitary Gaussian with zero mean. Of course, since we want to add real noise in direct space, we have to impose $n(\boldsymbol{q}) = [n(-\boldsymbol{q})]^*$, where the symbol $*$ denotes the complex conjugate.

A.1.3 Parallel code and performances

To obtain the results discussed in the Chapter 2 and 3 we had to integrate Eq. 1.30 for long times and large scales. To obtain a fast and efficient code we parallelised it. This allows for a significant speed gain, since we multiple processors work at the same time (in parallel) to integrate the equations. In our case, the system is divided in vertical slices, that are integrated by a different processor. To compute Fourier transforms or global observables the processors exchange information. Parallelising the code allowed us to speed up our simulations up to a factor 10 for the largest systems used ($L_x = 1024, L_y = 512$).

Importantly, we have to determine, for each system size, the optimal number of processors working in parallel. Indeed, if the number of processor is too large, code performances starts to worsen; this happens when the communication time between processors becomes comparable to the one spent to actually solve the equations. In

other words, the reason behind this is that the slices surface becomes comparable with their volume. The optimal number of processor also depends on the speed of the communication, and must therefore be determined for the particular cluster of processors used. The speed gain of parallelization is large, but we can further improve it by working on the Fourier transforms. The latter represent the actual bottle-neck of the code being the only operation of order $\mathcal{O}(N \log N)$. There are at least two ways to improve the code speed. First, $FFTW$ libraries are more efficient when system dimensions are a power of 2. Therefore, by using $L_x = 2^n$ with n an integer number, we obtain a code that is about 10% more efficient with respect to a system with same volume but $L_x \neq 2^n$. Then, we can reduce to the minimum the number of Fourier transform computed in a pseudo-spectral step. Notice however that this gain is marginal with respect to the parallelization.

A.1.4 Data storage

We saved snapshots of the system (*i.e.* the array of the values of $\phi(x, y)$ for each x, y of the simulation lattice) at regular intervals to produce images of the systems at a given time or, in some cases, to be able to post-process the data (compute observables after the simulation was ended). The files were saved in a binary format to keep their size as low as possible. Moreover, most of the time, we computed the observable on the fly (during the simulation), saving the time spent post-processing raw data and space on the disk. This was especially useful in cases for which we needed more statistics. Saving binary files, on the other hand, allows computing new observable of interest on simulations already completed, avoiding sending them again (especially useful for long ones). The files containing observables (like the number of bubbles, the average gas density and so on) were instead saved as simple text files so that the information were readily available to be seen or plotted.

A.1.5 Code stability

The pseudo-spectral method is a very powerful tool allowing us to simulate AMB+ equations with good resolution and efficiency. Anyway, as we saw, AMB+ equations are characterized by the addition of uncorrelated noise on neighbors sites and complicated mixed terms (comprising both nonlinearities and derivatives). For these reasons obtaining stable and reliable simulations may be challenging, especially due to the sudden nucleation events. We already discussed how we can mitigate such problems, here we see the limits of our code. If the non equilibrium term λ and ζ are sufficiently small we are able to get stable and reliable simulations with a fairly good resolution. In particular we can choose time and space resolution $dt = 0.02$ an $dx = 1$. In Fig.A.1.5 we delimit the region of parameters around Model B (*i.e.* $\zeta = \lambda = 0$), in which (for high noise level $D = 0.3$) we can exploit such resolution. By decreasing the noise we can extend this region a little more.

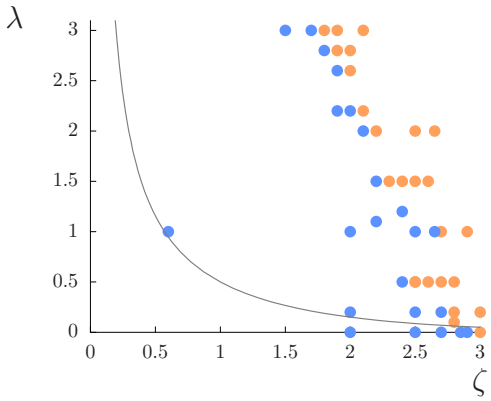

Figure A.1: Region of the $\zeta \times \lambda$ phase space in which the code is stable with accuracy $dt = 2 \times 10^{-2}$ and $dx = 1$ (blue dots). Test are done for system dimensions $L = 256 \times 128$, at high noise ($D = 0.3$). The solid line represent is the transition between reverse and direct Ostwald ripening process.

Crucially, when leaving this region, the non equilibrium terms become bigger, and the space-time resolution required to have a stable code increases very quickly (even in the deterministic case, starting from a random initial condition), making practically impossible to do perform simulations. To give the reader an idea of this phenomenon we report in table A.1 the minimum resolution needed to have stable simulations in the deterministic case ($D = 0$) along the line $\zeta = 2\lambda$. What makes things more complicated is that (A.1.2) contains space derivatives of order four: this means that increasing the space resolution by a factor α needs a corresponding increase in time resolution of α^4.

$\boldsymbol{\zeta = 2\lambda}$	$\boldsymbol{dt}$	$\boldsymbol{dx}$
2.7	$2.5\ 10^{-2}$	1
3	10^{-3}	1
3.2	10^{-4}	0.25
3.5	$<10^{-6}$	<0.25

Table A.1: Scaling of the minimal resolution needed to have a stable code in our simulations along the line $\zeta = 2\lambda$ for $D = 0$. Notice, for example, that increasing ζ from 3.2 to 3.5 we need a resolution that makes the code at least 400 times slower!

As a last remark, we want to point out that the finite-difference code used in [60], is less affected by the increase of the non-linear terms and allowed to perform simulations for $\lambda = 1$ and $\zeta = 4$, that we cannot reach with the pseudo-spectral code.

A.2 Data analysis

In this section, we present the most important algorithms that we used to analyze the density field $\phi(x, y)$. Namely, the algorithms used to locate vapor bubbles and identify the interface between liquid and vapor phase.

A.2.1 Algorithm to locate bubbles

In order to study the properties of the bubbly liquid and the bubbly phase separation, we need to locate bubbles and compute their area. To this end we consider the disconnected graph composed by the 2-dimensional grid of lattice points on which we are solving the AMB+ equation. In this graph two neighbors node are connected if they are both in the vapor state. A bubble of size n is then just a cluster of n (connected) nodes. To find all the clusters we run a deep-first search algorithm on a binary version of the density field ϕ_b (that assumes values 0 in the vapor phase and 1 in the liquid one).

We report the full algorithm in more details:

- Smoothing: The field $\phi(x, y)$ is smoothed to reduce the noise. The smoothing is performed by evolving the density field for 8 steps thought the deterministic dynamics of AMB+. From $\phi(x, t)$ we obain $\phi_s(x, y)$.

- Vapor-liquid discrimination: $\phi_s(x, y)$ is binarized in the following way:

$$\phi_b(x, y) = \begin{cases} 0 & \phi_s(x, y) \leq \bar{\phi} \\ 1 & \text{otherwise} \end{cases} \tag{A.17}$$

  where $\bar{\phi}$ is an intermediate density level between the vapor and the liquid one. In particular, we choose $\bar{\phi} = 0$, the intermediate point between the mean-field binodals on the $\zeta = 2\lambda$ line. The points (x, y) where $\phi_b = 0$ are considered as vapor, the others as liquid.

- Breath first search: the algorithm is performed by scanning linearly the binarized field ϕ_b. Each time we find a point for which $\phi_b = 0$ and that does not belong to the list of visited nodes (initially empty), we find a cluster. We then run the breath first algorithm to identify the other points of the cluster. When the the breath first algorithm ends, we continue the scanning procedure until the last node.

  The breath first search algorithm is implemented on the cluster k as follows:

  1. We insert the point in the list of visited ones.
  2. If $\phi_b = 0$ we label it with k, increase the cluster size by one and insert its 4 neighbors in the queue.

3. If the queue is not empty we repeat (a,b) for the next point in the list.

One important point to notice is that we create an algorithm that is not recursive. In this way we avoid to hit the maximum recursion depth limit (that depends on the programming language and on the machine used to run the code). Indeed this is very likely when trying to locate the vapor reservoir of the bubbly phase (the algorithm sees it as a very large bubble).

In Fig. A.2 we can see the results of running the algorithm on two different cases.

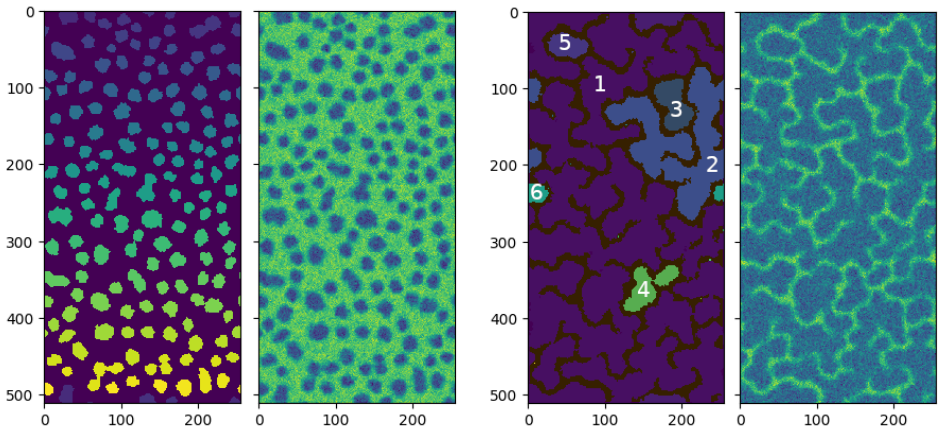

Figure A.2: Two examples of how the algorithm to locate bubbles works. On the right of each couple of images we have the density field $\phi(x, y)$, on the left the bubbles found by the algorithm (description in the text). Here, different bubbles have different colors.

A.2.2 Bubble size distribution

In order to study the statistical properties of the bubbly liquid and bubbly phase separation, we study the PDF of the bubble size. This quantity, that we will call bubble size distribution $P(A)$, corresponds to the probability that the size of a bubble drawn at random in the steady-state is equal to A. Since we compute $P(A)$ on the fly (*i.e.* during the simulation), we need to save a certain number of $P_t(A)$ each computed on a different time interval $t, t + \Delta t$. In this way we can average over distributions $P_t(A)$ in the steady-state (disregarding the initial transient). To build $P_t(A)$ we run (every N_{pdf} time-steps) the algorithm to locate the bubbles described in the previous section, and compute their area. Every time we count the number $N(A, t)$ of bubbles having area A at time-step t. Finally, $P_t(A)$ corresponds to:

$$P_t(A) = \frac{\sum_{i=0}^{\Delta t/N_{pdf}} N(A, t + iN_{pdf})}{\sum_{A=0}^{\infty} \sum_{i=0}^{\Delta t/N_{pdf}} N(A, t + iN_{pdf})} \tag{A.18}$$

This ensure that $P(A)$ is an actual PDF. Indeed we have:

$$\sum_{A=0}^{\infty} P_t(A) = 1 \tag{A.19}$$

A.2.3 Identification of the interface

In this section, we describe the algorithm we used to locate the interface between vapor and liquid in a systems that is fully phase separated, without bubbles and with an interface passing through the full system (see Fig.A.3). If the interface is along the x-axis the algorithm is as follow: For every coordinate x, we scan the pixel starting in the vapor phase until we find the first pixel in the liquid phase. To do that we find the first $\bar{y}$ such that $\phi(x, \bar{y}) > \phi_{th}$, choosing $\phi_{th} = (\phi_1 + \phi_2)/2$ in between the mean-field binodals $\phi_{1,2}$. For that x the interface position along in the y direction is set to:

$$h(x) = \bar{y} + \frac{\phi(x, \bar{y}) - \phi_{th}}{\phi(x, \bar{y}) - \phi(x, \bar{y} + \Delta x)} \,. \tag{A.20}$$

Different values of ϕ_{th} do not change the results as far as ϕ_{th} is sufficiently far from the binodals. Notice that if we had overhangs, we would need a more sophisticated algorithm to find the interface. In Fig. A.3, we can see the algorithm in action.

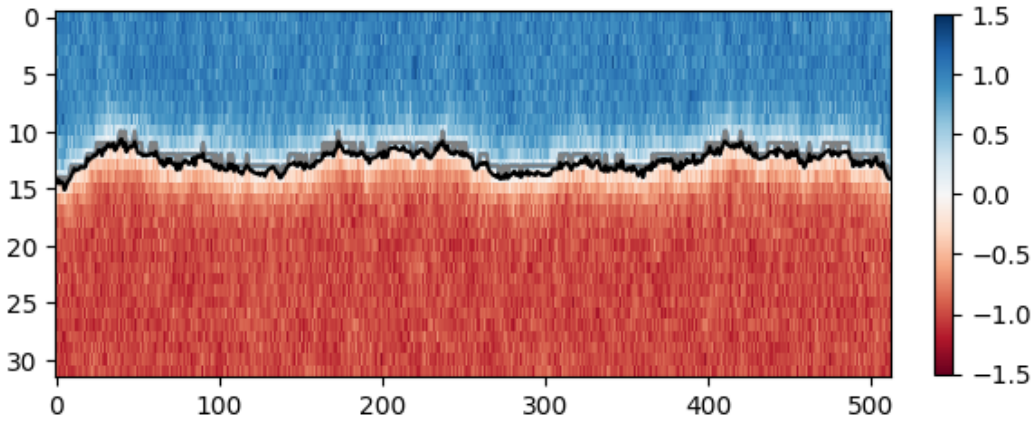

Figure A.3: Interface localization using the algorithm described in the text. Grey line: curve of the points $(x, \bar{y})$, where $\bar{y}$ is the first liquid pixel starting from the top. Black line: $h(x)$ computed with Eq. (A.2.3). For visualization purposes we show just the top part of a system of size 512×64. Moreover, we squeeze the image along x (this results in rectangular pixels).

A.3 Conclusion

In this chapter, we presented the main algorithms used to integrate AMB+ equations and analyze the density field. In particular, we described the parallel pseudo-spectral algorithm used to integrate the spatial part of the equations and justified its choice. Then, we briefly presented the algorithms used to analyze the density field $\phi(\boldsymbol{x}, t)$, to locate the vapor bubbles and interfaces in phase-separated states. The two following chapters, 2 and 3, are instead devoted to the study of AMB+ physics using the algorithm described here.

Appendix B

AMB+

B.1 Liquid density shift stability with time resolution

In Sec. 2.4.4, we saw the difficulties emerging while estimating the asymptotic behavior of ϕ_L. One of them is that we cannot extrapolate this value from the second peak of the PDF of the local field $P(\phi)$, unlike in equilibrium, since it shifts with global density ϕ_0. Here, we check the stability of this density shift – and incidentally of all our results in the bubbly liquid phase – when increasing time resolution. The first observation is that, for high global density values ϕ_0, we need a higher time resolution than $dt = 0.02$ to stabilize our the code. Even at lower ϕ_0, decreasing dt slightly changes the PDF of the local density field $P(\phi)$. The effect of increasing dt is similar to the one obtained by increasing D: the peaks of $P(\phi)$ are broader and get closer to each other. A part than that, the global picture remains the same. Indeed, the shift of the second peak of $P(\phi)$, although slightly smaller for higher time resolutions, remains evident when convergence in time resolution is attained (see Fig. B.1).

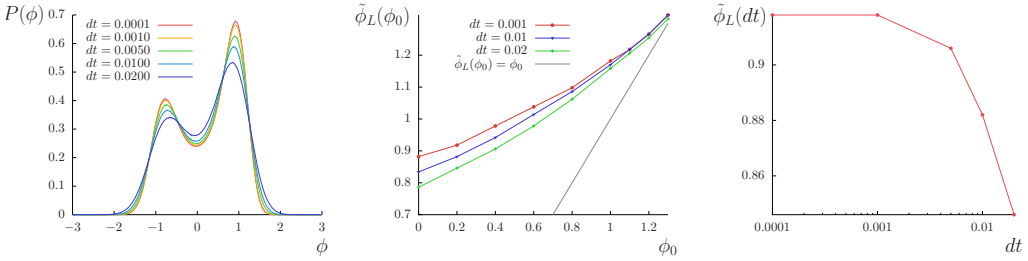

(a) $D = 0.3, \phi_0 = 0.2$ **(b)** $D = 0.3$ **(c)** $D = 0.3, \phi_0 = 0.2$

Figure B.1: (a) PDF of the local density $P(\phi)$ varying dt. In the bubbly liquid, the choice of a higher time resolution changes the shape of $P(\phi)$. In particular, the higher the time resolution, the more peaked is the distribution. At the same time we have a slight shift of the peaks positions. Parameters: $D = 0.3, \phi_0 = -0.2$.
(b) Position of the liquid peak of $P(\phi)$ as a function of the global density ϕ_0 for noise $D = 0.3$. The different curves have a different time resolution. In this Fig. the convergence is reached at high ϕ_0, while in Fig. (c) we reach it for $\phi_0 = 0.2$. This proves that the shift is still present even when we reach convergence in dt.
(c) Convergence in time-resolution of the position of the liquid peak of $P(\phi)$ for $D = 0.3, \phi_0 = 0.2$

B.2 Algorithm to extract ϕ_{BL} from the density profile

In Sec.2.4.1, we saw how it is possible to estimate the convergence time towards the bubbly phase separated state, by studying the time series of the average density inside the bubbly liquid ϕ_{BL}. Here we present the algorithm used to extrapolate ϕ_{BL} from the density profile $\phi(x,t)$ (as defined in equation (2.2) and shown in Fig.2.11).

The algorithm is as follows (see also Fig. B.2):

- Compute the distance between the maximum and minimum of $\phi(x,t)$:

$$\Delta\phi_{max} = \phi_{max} - \phi_{min} \tag{B.1}$$

- Consider the threshold given by the following density value:

$$\phi_{th} = \phi_{min} + \alpha\Delta\phi_{max} \tag{B.2}$$

- Determine the vapor region as the one containing the maximum number of consecutive point with $\phi(x,t) < \phi_{th}$ (considering the periodic boundary conditions).

- Determine the band interfaces as the values x_1' and x_2' delimiting the vapor region. The width of the band is equal to: $w' = x_1' - x_2'$

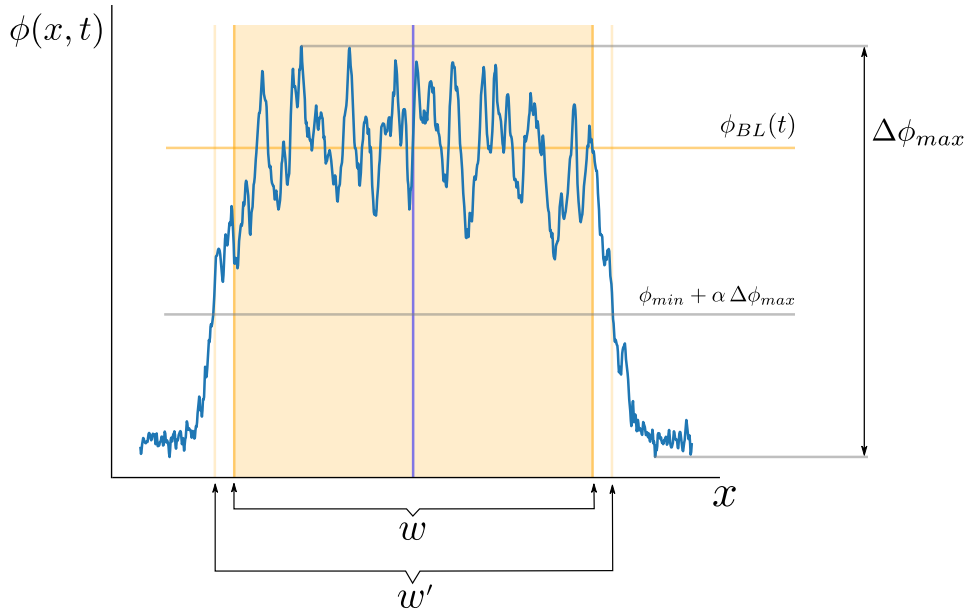

Figure B.2: Example of a density profile $\phi(x,t)$, from which we extract the average density in the bubbly liquid $\phi_{BL}(t)$ (by averaging $\phi(x,t)$ in the orange area). See the main text for the complete algorithm and the definition of the various symbols.

- Discard the interfacial part by considering just a fraction of the band width $f = w/w'$. This delimits the region $(x_1, x_2 = x_1 + w)$ on which to compute the bubbly liquid density.
- Compute the bubbly liquid density as:

$$\phi_{BL}(t) = \frac{1}{w}\int_{x_1}^{x_1+w} \phi(x,t) \tag{B.3}$$

The parameter of the algorithm are the threshold level (controlled through α) and the fraction of band considered f. In order to detect the interface and the bulk of the bubbly liquid reliably, we need to optimize these two parameters. In particular, we choose $\alpha = 0.4$, getting a threshold closer to ϕ_V (the density level with smaller fluctuations), and $f = 0.6$. The exact values of f and α do not really matter as far as they are reasonable. This method, once the parameters are chosen correctly, is not affected by systematic errors like the naive one. For large systems such as the one shown in Fig. 2.11, is reliable and provides a good estimate of $\phi_{BL}(t)$.

Appendix C

Minimal model

C.1 Code implementation

In this section, we describe the main algorithms used to simulate our model, and present some considerations about efficiency. The main algorithms used in the model are the research of the nearest neighbors (for the Ostwald ripening step), the determination of the bubbles that are in contact (for the coalescence step), and the nucleation.

C.1.1 Efficiency

Our model deals with $N(t)$ spatially extended object whose radius is variable and goes from $R_0 = 0.5$ (for the newly nucleated bubbles) up to $L/2$ (due to their circular shape) for bubbly phase separated configurations. Interactions between bubbles are both local (by contact) and with their nearest neighbor. In particular, having extended objects of variable size, we cannot blindly apply the usual boxing algorithms used in particles models to increase efficiency. The latter rely on partitioning the space in a grid of boxes. Each particle belongs to a particular box. Therefore, interactions can be computed locally in the box (and in the surrounding ones, if needed). This allows one to reduce the computational cost of pairwise operation from $\mathcal{O}(N^2)$ to $\mathcal{O}(N)$. Of course, this kind of technique, can be used just in absence of long range interactions. We will see, however, a modification of the boxing algorithm can be applied for both the coalescence process and the research of the closest bubble. Finding alternative solutions to the brute force algorithm used to find the nearest neighbors and the bubbles that are in contact, is vital to simulate large system sizes. Indeed, the easiest solution is to compute all the $N(N-1)/2 \sim N^2$ distances between bubbles in the system. This solution is of computational complexity of order $\mathcal{O}(N^2)$. Notice that even the nucleation process suffer from this problem: at each time step, we nucleate a certain number of bubbles that is, roughly speaking, a fraction of the

total number of bubbles. For each of them, we need to extract a random position and check whether they collide with other bubbles. Checking the collision with all the other particle lead to a computational complexity of order $\mathcal{O}(N^2)$.

C.1.2 Nearest neighbor algorithm

To simulate the Ostwald ripening dynamics, we need to find for each bubble its nearest neighbor. In order to avoid computing all the distances between bubbles, we rely on a kind of boxing algorithm by dividing the system in a grid of squares. Then, for each bubble, we look for the nearest neighbors in a certain finite radius around it. We now describe the algorithm in more details.

First, we create an occupancy array $O(i, j)$: each element of the array correspond to a box in the system, and has value equal to the label of the bubble occupying it (partially or completely) or -1 if it is not occupied. To create $O(i, j)$, we perform a loop over all the bubbles. For each bubble n, we set $O(i, j) = n$ for all the boxes (i, j) occupied by the bubble. The creation of the occupancy array $O(i, j)$ needs an algorithm whose computational cost does not scale with system volume. Once again, cycling through all the boxes and checking if their distance from the bubble center is smaller or equal than the bubble radius is an expensive choice that scales with system volume $V = L \times L > N^2$. To avoid this, we use the equation of a circle to determine, for each coordinate i, which boxes (i, j) are occupied.

Once we have the occupation array, we perform another loop over the bubbles. For each bubble n, we compute the distances $d(n, i)$ from every other bubble i occupying at least one box in a radius $r+R_n$ from $\boldsymbol{x}_n$. The smallest distance determines the nearest neighbor. In order to avoid loops on too many boxes, we optimized the research radius r value to 1.5 times the average bubble distance ξ, approximated to:

$$\xi = \sqrt{\frac{V(1 - v_g)}{\pi N(t)}} \tag{C.1}$$

where we divide the available volume outside vapor bubbles $V(1 - v_g)$ by their number $N(t)$. This algorithm has computational complexity that scales linearly with the number of bubbles.

C.1.3 Coalescence

In this section, we present the algorithm we used to find bubbles in contact and coalesce them. The easiest solution would be to compute the distances $d(i, j)$ between all the couples of bubbles (i, j) and check which of them has distance $d(i, j) < R_i + R_j$. This method, although easy to implement, has a computational cost of $\mathcal{O}(N^2)$. In order to use a more efficient algorithm, we rely on the occupancy matrix $O(i, j)$. Initially $O(i, j) = -1 \; \forall (i, j)$ to indicate that no box has been visited. Then, we perform a loop over all the bubbles. For each bubble n (with center in

x_n, y_n and radius R_n), we scan all the boxes (i, j) for which $x_n - R < i < x_n + R$ and $y_n - R < j < y_n + R$. For each scanned box (i, j), we check if the box was previously visited (*i.e.* if $O(i, j) \neq -1$). If not, we set $O(i, j) = n$. If yes, then $O(i, j)$ is equal to some number k as a result of a previous scan of that box. We check if bubble n overlaps with bubble k (this is the case if $d(n, k) < R_n + R_k$). If the bubbles overlap, we assign both bubbles to the same cluster. Finally, if $R_n < R_k$ we set $O(i, j) = n$. Once all clusters are determined, I can apply the coalescence formula (3) on each of them.

C.1.4 Nucleation

After the coalescence step, we nucleate a certain number of bubbles aN to compensate the vapor volume loss caused by α_C. For each nucleation event, we extract random positions until the newly nucleated bubble does not overlap with any other bubble. The probability that a point chosen at random is inside a bubble is v_g. The probability that a bubble of radius R_0 positioned at random is in contact with another one is larger than this. Indeed, in this case the excluded volume is composed by the volume occupied by vapor bubble plus a shell of width R_0 outside each of them. Therefore, the average number of trials before a good position is found is larger than $\frac{1}{1-v_g}$. For this reason, the nucleation can become a bottleneck when dealing with large vapor fractions. Finally, the number of operations required by this algorithm is higher than $\frac{a}{1-v_g}N^2$. The probability that a randomly chosen position is inside a certain bubble n, is proportional to its volume. Therefore, ordering bubbles by their size we improve the code efficiency. Indeed, this reduces the number of distances we have to compute when choosing a trial position that would bring the bubble to overlap. In particular, the ordering step can be performed every N_s time-step though a quick-sort algorithm whose computational cost is $\mathcal{O}(N \log N)$. Despite the efficiency gain, the algorithm is still of computational cost $\mathcal{O}(N^2)$. However, it was not the bottleneck for most simulations. For this reason, we did not improve it further. Anyway, to access larger system we will need a linear algorithm. We plan to improve its performances to be able to reach larger system sizes at high diffusivity D.

We now list some possible improvements. An efficient way to proceed would be to recompute the occupancy matrix and then extract randomly one of the boxes that are not occupied by other bubbles. This may create problems at high vapor fractions v_g, as there may be no available empty boxes. Otherwise, one could choose at random a box (empty or not) and check overlapping just with the bubbles occupying it. In these solutions nucleation would scale linearly with the number of bubbles N.

C.2 Stability with decreasing time-discretization

In this section we will justify our choice of time-resolution for the bubble diffusion and confirm its stability. First, we must notice that the choice of Δt is done based on physical reasons. Specifically, Δt has to be chosen in such a way that the typical discrete displacement in a time-step is much smaller than the size of a single bubble. In others words:

$$\sqrt{\frac{D}{R_0^2}}\Delta t \ll R_0 \tag{C.2}$$

that implies:

$$\Delta t \ll \frac{R_0^3}{D} \tag{C.3}$$

If this condition is not met, the chosen time-resolution is not sufficient to resolve bubbles trajectories. In particular, at each time-step bubbles have a non-negligible probability to move across other bubbles, without touching them and therefore coalescing. So, even though the choice of Δt does not pose any stability problem, by using a large Δt we are underestimating the coalescence process. In our simulations, unless otherwise stated, we fix $\Delta t = 0.1$. Strictly speaking, this choice is appropriate only for small diffusivity values, while already at $D = 1$ we have: $\frac{R_0^3}{D} = 0.125$ that is just slightly larger than $\Delta t = 0.1$. We will anyway use $\Delta t = 0.1$ for higher diffusivity values. Despite leading to (small)) systematic overestimation (or underestimation) of some observables, we will see that it does not change the physics of the features we primarily investigate.

In order to asset the effect on the choice of temporal resolution Δt, we simulated a bubbly phase separated system at high diffusivity $D = 5$ for system size $L = 200$. In Fig. C.1 we can observe how, by increasing Δt, we underestimate more and more the effect of coalescence. This reflects on various observables: the average number of bubbles in the steady state is higher, while their size is smaller; at the same time the vapor fraction in the bubbly liquid is larger (although is less affected than the average number and size of bubbles). Finally, we can see how the bubble size distribution conserves the same shape. This suggests that while our estimates of some observables is slightly different (of about $\pm 10 - 20\%$ between $\Delta t = 0.1$ and lower values), the basic physics does not change. Our choice of $\Delta t = 0.1$ is therefore practically justified even for higher diffusivity values.

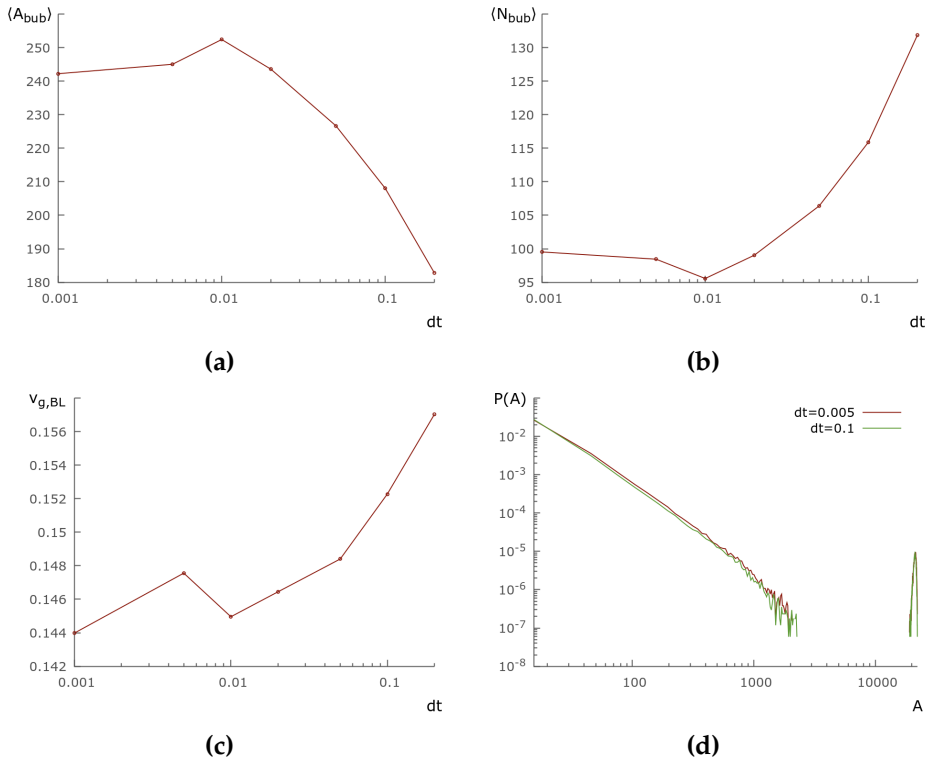

Figure C.1: Behavior of some key observables when changing temporal resolution through Δt in the bubbly phase separated state ($D = 5, L = 200, v_g = 0.6$). As we can see, for high Δt values, the coalescence process is underestimated. This results in steady-state with more bubbles that are smaller on average. This does ot change the global physics of the state that is bubbly phase separated for all the time resolution considered. Moreover, while the bubble size distribution $P(A)$ is slightly different when changing Δt, its shape is just slightly affected. Notice the behavior with Δt of the observables considered is not monotonic. This is actually due to the fact the for $\Delta t < 0.01$, along with Δt (related bubble diffusion) we also had to decrease the temporal resolution of the Ostwald process Δt_{Ost} (that we otherwise set to 0.01, as discussed in 4.1.2).
(a) Average bubble size (including the vapor reservoir)
(b) Average number of bubbles
(c) Average vapor fraction in the bubbly liquid
(d) Bubble size distribution $P(A)$ for two different Δt

Bibliography

[1] X.-q. Shi, G. Fausti, H. Chaté, C. Nardini, and A. Solon, Physical Review Letters **125**, 168001 (2020).

[2] C. B. Caporusso, P. Digregorio, D. Levis, L. F. Cugliandolo, and G. Gonnella, Physical Review Letters **125**, 178004 (2020).

[3] G. Fausti, E. Tjhung, M. E. Cates, and C. Nardini, Physical Review Letters **127**, 068001 (2021).

[4] N. Goldenfeld, *Lectures on phase transitions and the renormalization group* (CRC Press, 2018).

[5] P. M. Chaikin, T. C. Lubensky, and T. A. Witten, *Principles of condensed matter physics*, Vol. 10 (Cambridge university press Cambridge, 1995).

[6] A. Bray, Advances in Physics **43**, 357 (1994).

[7] M. C. Marchetti, J.-F. Joanny, S. Ramaswamy, T. B. Liverpool, J. Prost, M. Rao, and R. A. Simha, Reviews of Modern Physics **85**, 1143 (2013).

[8] G. Gompper, R. G. Winkler, T. Speck, A. Solon, C. Nardini, F. Peruani, H. Löwen, R. Golestanian, U. B. Kaupp, L. Alvarez, *et al.*, Journal of Physics: Condensed Matter **32**, 193001 (2020).

[9] T. Vicsek and A. Zafeiris, Physics Reports **517**, 71 (2012).

[10] S. Ramaswamy, Journal of Statistical Mechanics: Theory and Experiment **2017**, 054002 (2017).

[11] D. Helbing, Reviews of Modern Physics **73**, 1067 (2001).

[12] C. Becco, N. Vandewalle, J. Delcourt, and P. Poncin, Physica A: Statistical Mechanics and its Applications **367**, 487 (2006).

[13] M. Ballerini, N. Cabibbo, R. Candelier, A. Cavagna, E. Cisbani, I. Giardina, V. Lecomte, A. Orlandi, G. Parisi, A. Procaccini, M. Viale, and V. Zdravkovic, Proceedings of the National Academy of Sciences **105**, 1232 (2008).

[14] S. Camazine, J.-L. Deneubourg, N. R. Franks, J. Sneyd, G. Theraula, and E. Bonabeau, *Self-organization in biological systems* (Princeton university press, 2020).

[15] J. Joanny and J. Prost, HFSP journal **3**, 94 (2009).

[16] Y. Sumino, K. H. Nagai, Y. Shitaka, D. Tanaka, K. Yoshikawa, H. Chaté, and K. Oiwa, Nature **483**, 448 (2012).

[17] J. R. Howse, R. A. L. Jones, A. J. Ryan, T. Gough, R. Vafabakhsh, and R. Golestanian, Physical Review Letters **99**, 048102 (2007).

[18] B. Yigit, Y. Alapan, and M. Sitti, Soft Matter **16**, 1996 (2020).

[19] J. Deseigne, S. Léonard, O. Dauchot, and H. Chaté, Soft Matter **8**, 5629 (2012).

[20] A. Bricard, J.-B. Caussin, N. Desreumaux, O. Dauchot, and D. Bartolo, Nature **503**, 95 (2013).

[21] R. Matas-Navarro, R. Golestanian, T. B. Liverpool, and S. M. Fielding, Physical Review E **90**, 032304 (2014).

[22] J. Toner and Y. Tu, Physical Review Letters **75**, 4326 (1995).

[23] A. Cavagna, A. Cimarelli, I. Giardina, G. Parisi, R. Santagati, F. Stefanini, and M. Viale, Proceedings of the National Academy of Sciences **107**, 11865 (2010).

[24] W. Bialek, A. Cavagna, I. Giardina, T. Mora, E. Silvestri, M. Viale, and A. M. Walczak, Proceedings of the National Academy of Sciences **109**, 4786 (2012).

[25] R. F. Storms, C. Carere, F. Zoratto, and C. K. Hemelrijk, Behavioral Ecology and Sociobiology **73**, 10 (2019).

[26] Y. Katz, K. Tunstrøm, C. C. Ioannou, C. Huepe, and I. D. Couzin, Proceedings of the National Academy of Sciences **108**, 18720 (2011).

[27] J. E. Herbert-Read, A. Perna, R. P. Mann, T. M. Schaerf, D. J. T. Sumpter, and A. J. W. Ward, Proceedings of the National Academy of Sciences **108**, 18726 (2011).

[28] D. Nishiguchi, K. H. Nagai, H. Chaté, and M. Sano, Physical Review E **95**, 020601 (2017).

[29] H. P. Zhang, A. Be'er, E.-L. Florin, and H. L. Swinney, Proceedings of the National Academy of Sciences **107**, 13626 (2010).

[30] S. J. DeCamp, G. S. Redner, A. Baskaran, M. F. Hagan, and Z. Dogic, Nature Materials **14**, 1110 (2015).

[31] S. Ramaswamy, Annual Review of Condensed Matter Physics **1**, 323 (2010).

[32] H. H. Wensink, J. Dunkel, S. Heidenreich, K. Drescher, R. E. Goldstein, H. Löwen, and J. M. Yeomans, Proceedings of the National Academy of Sciences **109**, 14308 (2012).

[33] I. Buttinoni, J. Bialké, F. Kümmel, H. Löwen, C. Bechinger, and T. Speck, Physical Review Letters **110**, 238301 (2013).

[34] G. Liu, A. Patch, F. Bahar, D. Yllanes, R. D. Welch, M. C. Marchetti, S. Thutupalli, and J. W. Shaevitz, Physical Review Letters **122**, 248102 (2019).

[35] J. Roostalu, J. Rickman, C. Thomas, F. Nédélec, and T. Surrey, Cell **175**, 796 (2018).

[36] J. M. Belmonte, M. Leptin, and F. Nédélec, Molecular Systems Biology **13**, 941 (2021).

[37] C. Chen, S. Liu, X.-q. Shi, H. Chaté, and Y. Wu, Nature **542**, 210 (2017).

[38] A. Attanasi, A. Cavagna, L. D. Castello, I. Giardina, S. Melillo, L. Parisi, O. Pohl, B. Rossaro, E. Shen, E. Silvestri, and M. Viale, PLOS Computational Biology **10**, e1003697 (2014).

[39] C. Bechinger, R. Di Leonardo, H. Löwen, C. Reichhardt, G. Volpe, and G. Volpe, Reviews of Modern Physics **88**, 045006 (2016).

[40] L. K. Abdelmohsen, F. Peng, Y. Tu, and D. A. Wilson, Journal of Materials Chemistry B **2**, 2395 (2014).

[41] C. Lozano, B. ten Hagen, H. Löwen, and C. Bechinger, Nature Communications **7**, 12828 (2016).

[42] T. Bäuerle, A. Fischer, T. Speck, and C. Bechinger, Nature Communications **9**, 3232 (2018).

[43] D. E. Woodward, R. Tyson, M. R. Myerscough, J. D. Murray, E. O. Budrene, and H. C. Berg, Biophysical Journal **68**, 2181 (1995).

[44] T. Surrey, F. Nédélec, S. Leibler, and E. Karsenti, Science **292**, 1167 (2001).

[45] T. Vicsek, A. Czirók, E. Ben-Jacob, I. Cohen, and O. Shochet, Physical Review Letters **75**, 1226 (1995).

[46] H. Chaté and B. Mahault, (2019), arXiv:1906.05542 .

[47] J. Tailleur and M. E. Cates, Physical Review Letters **100**, 218103 (2008).

[48] M. E. Cates and J. Tailleur, Annual Review of Condensed Matter Physics **6**, 219 (2015).

[49] Y. Fily and M. C. Marchetti, Physical Review Letters **108**, 235702 (2012).

[50] M. E. Cates and J. Tailleur, Europhysics Letters **101**, 20010 (2013).

[51] R. Wittkowski, A. Tiribocchi, J. Stenhammar, R. J. Allen, D. Marenduzzo, and M. E. Cates, Nature Communications **5**, 4351 (2014).

[52] A. P. Solon, J. Stenhammar, M. E. Cates, Y. Kafri, and J. Tailleur, Physical Review E **97**, 020602 (2018).

[53] A. P. Solon, J. Stenhammar, R. Wittkowski, M. Kardar, Y. Kafri, M. E. Cates, and J. Tailleur, Physical Review Letters **114**, 198301 (2015).

[54] I. Theurkauff, C. Cottin-Bizonne, J. Palacci, C. Ybert, and L. Bocquet, Physical Review Letters **108**, 268303 (2012).

[55] M. N. Van Der Linden, L. C. Alexander, D. G. Aarts, and O. Dauchot, Physical Review Letters **123**, 098001 (2019).

[56] A. Scagliarini and I. Pagonabarraga, Soft Matter **16**, 8893 (2020).

[57] B. Liebchen, D. Marenduzzo, and M. E. Cates, Physical Review Letters **118**, 268001 (2017).

[58] A. Tiribocchi, R. Wittkowski, D. Marenduzzo, and M. E. Cates, Physical Review Letters **115**, 188302 (2015).

[59] J. Stenhammar, D. Marenduzzo, R. J. Allen, and M. E. Cates, Soft Matter **10**, 1489 (2014).

[60] E. Tjhung, C. Nardini, and M. E. Cates, Physical Review X **8**, 031080 (2018).

[61] E. Demir, Y. I. Yaman, M. Basaran, and A. Kocabas, eLife **9**, e52781 (2020).

[62] P. Digregorio, D. Levis, A. Suma, L. F. Cugliandolo, G. Gonnella, and I. Pagonabarraga, Physical Review Letters **121**, 098003 (2018).

[63] J. U. Klamser, S. C. Kapfer, and W. Krauth, Nature communications **9**, 1 (2018).

[64] P. C. Hohenberg and B. I. Halperin, Reviews of Modern Physics **49**, 435 (1977).

[65] F. Caballero, C. Nardini, and M. E. Cates, Journal of Statistical Mechanics: Theory and Experiment **2018**, 123208 (2018).

[66] R. Singh and M. E. Cates, Physical Review Letters **123**, 148005 (2019).

[67] E. Tjhung, D. Marenduzzo, and M. E. Cates, Proceedings of the National Academy of Sciences **109**, 12381 (2012).

[68] J. Bialké, J. T. Siebert, H. Löwen, and T. Speck, Physical Review Letters **115**, 098301 (2015).

[69] S. Pattanayak, S. Mishra, and S. Puri, Soft Materials **19**, 286 (2021).

[70] I. Lifshitz and V. Slyozov, Journal of Physics and Chemistry of Solids **19**, 35 (1961).

[71] E. D. Siggia, Physical Review A **20**, 595 (1979).

[72] D. A. Huse, Physical Review B **34**, 7845 (1986).

[73] V. M. Kendon, M. E. Cates, I. Pagonabarraga, J.-C. Desplat, and P. Bladon, Journal of Fluid Mechanics **440**, 147 (2001).

[74] J. S. Rowlinson and B. Widom, *Molecular theory of capillarity* (Courier Corporation, 2013).

[75] A. P. Solon, J. Stenhammar, M. E. Cates, Y. Kafri, and J. Tailleur, New Journal of Physics **20**, 075001 (2018).

[76] R. Zakine, Y. Zhao, M. Knežević, A. Daerr, Y. Kafri, J. Tailleur, and F. van Wijland, Physical Review Letters **124**, 248003 (2020).

[77] C. F. Lee, Soft matter **13**, 376 (2017).

[78] A. Patch, D. M. Sussman, D. Yllanes, and M. C. Marchetti, Soft matter **14**, 7435 (2018).

[79] A. K. Omar, Z.-G. Wang, and J. F. Brady, Physical Review E **101**, 012604 (2020).

[80] S. Hermann, D. de las Heras, and M. Schmidt, Physical Review Letters **123**, 268002 (2019).

[81] A. J. Bray, A. Cavagna, and R. Travasso, Physical Review E **65**, 016104 (2001).

[82] J. S. Langer, Reviews of Modern Physics **52**, 1 (1980).

[83] M. E. Cates and E. Tjhung, J Fluid Mech. **836**, P1 (2018).

[84] J. Meunier, Journal of Physics: Condensed Matter **48**, 1819 (1987).

[85] E. M. Blokhuis and D. Bedeaux, Molecular Physics **80**, 705 (1993).

[86] A. Shinozaki and Y. Oono, Physical Review E **47**, 804 (1993).

[87] J. Bricmont, A. Kupiainen, and J. Taskinen, Communications on Pure and Applied Mathematics **52**, 839 (1999).

[88] J. Bickmann and R. Wittkowski, Physical Review Research **2**, 033241 (2020).

[89] D. M. Sussman, J. M. Schwarz, M. C. Marchetti, and M. L. Manning, Physical Review Letters **120**, 058001 (2018).

université PARIS-SACLAY
ÉCOLE DOCTORALE
Physique en l'Île-de-France (PIF)

Titre: Séparation de phase dans la matière active

Mots clés: Démixtion , Transitions de phases , Systèmes à sec, Matière active, Physique statistique hors équilibre, Auto-organisation

Résumé: La matière active désigne une classe des systèmes hors-équilibre dans laquelle l'énergie est dissipée localement par ses constituants pour se transformer en mouvement. Grâce à l'interaction entre les particules, il y a une grande variété de phénomènes collectifs. Ainsi, dans certains systèmes, il peut y avoir une séparation de phase entre des zones de haute et basse densité, même en l'absence de force d'attraction. À la base de la séparation de phase appelée motility-induced phase-separation (MIPS), il y a une rétroaction positive entre l'accumulation des particules et la diminution de la vitesse. Les particules bougent plus lentement dans les zones à forte densité et donc s'accumulent.

La séparation de phase MIPS est le sujet de cette thèse et on va l'étudier avec différents points de vue. Dans un premier temps, on adopte l'approche du modèle active B+, qui est une théorie des champs capable de prédire l'existence de nouvelles séparations de phase telles que : une séparation microphase où des bulles de vapeur diffusent dans un milieu dense, et une séparation macrophase où il y a une phase dense en équilibre avec une phase diluée à l'extérieur. En particulier, on confirme l'existence de ces phases asymptotiquement et on étudie leurs propriétés statistiques. On trouve que le temps de relaxation vers l'état stationnaire dépend de la taille du système pour la séparation macrophase.

Ensuite, on étudie le concept de tension superficielle et on montre qu'en matière active on ne peut pas avoir qu'une définition, mais on doit définir plusieurs tensions superficielles.

Pour conclure, on fait le lien entre le modèles de particules et la théorie des champs en étudiant un modèle minimal de bulles développé pour identifier les ingrédients minimaux dans la séparation de phase MIPS, c'est-à-dire la compétition entre la diffusion des boules et l'Ostwald ripening (le mécanisme qui permet aux petites bulles de grandir au détriment des plus grandes).

Title: Phase Separation in Active Systems: Non-Equilibrium Fingerprints

Keywords: Phase separation, Phase Transition, Dry systems, Acive matter, Non-equilbrium statistical mechanics, Self-organisation

Abstract: Active matter is intrinsically out of equilibrium because energy is converted into systematic motion by its constituents, and exhibit fascinating collective phenomena. One of them is phase separation between dense and dilute regions which, unlike in equilibrium, can happen even in absence of attraction among particles.
In this Thesis, we study phase separation in active systems. First, we adopt the coarse-grained point of view of Active Model B+, a field theory based on symmetry arguments and conservation laws. This predicts the emergence of novel types of phase separation, impossible in equilibrium: a microphase separated state and bubbly phase separation (the coexistence between this microphase separated state and the homogeneous phase). In the first part of the Thesis, we study the statistical properties of micro and bubbly phase separation, confirm their asymptotic existence and show how the time convergence to the steady state is system size dependent in the bulk phase separation.
Secondly we study the concept of interfacial tension in active systems, and derive from first principles (and for the first time) the capillary wave tension, which determines the elasticity of active liquid-vapor interfaces. By doing so, we show that no unique definition of surface tension can exist in active systems, thus ending a long-dated debate. Discovering that the capillary interfacial tension can become negative because of activity, we also find new types of phase separation, among which a previously unknown 'active foam' state.
Finally, we introduce and study a minimal model for the dynamics of vapor bubbles in micro and bubbly phase separation. Thanks to this, we shed light on the statistical properties of these phases and on how they might be controlled in the future in particle-based models.

Université Paris-Saclay
Espace Technologique / Immeuble Discovery
Route de l'Orme aux Merisiers RD 128 / 91190 Saint-Aubin, France